

## INFORMATION TO USERS

This manuscript has been reproduced from the microfilm master. UMI films the text directly from the original or copy submitted. Thus, some thesis and dissertation copies are in typewriter face, while others may be from any type of computer printer.

The quality of this reproduction is dependent upon the quality of the copy submitted. Broken or indistinct print, colored or poor quality illustrations and photographs, print bleedthrough, substandard margins, and improper alignment can adversely affect reproduction.

In the unlikely event that the author did not send UMI a complete manuscript and there are missing pages, these will be noted. Also, if unauthorized copyright material had to be removed, a note will indicate the deletion.

Oversize materials (e.g., maps, drawings, charts) are reproduced by sectioning the original, beginning at the upper left-hand corner and continuing from left to right in equal sections with small overlaps.

ProQuest Information and Learning  
300 North Zeeb Road, Ann Arbor, MI 48106-1346 USA  
800-521-0600


UMI<sup>®</sup>



University of Alberta

# Pairing Fluctuations and the Pseudogap

by

Simona Verga 

A thesis submitted to the Faculty of Graduate Studies and Research  
in partial fulfillment of the requirements for the degree of  
Doctor of Philosophy

Department of Physics

Edmonton, Alberta

Fall 2005



Library and  
Archives Canada

Bibliothèque et  
Archives Canada

Published Heritage  
Branch

Direction du  
Patrimoine de l'édition

0-494-08747-1

395 Wellington Street  
Ottawa ON K1A 0N4  
Canada

395, rue Wellington  
Ottawa ON K1A 0N4  
Canada

*Your file* *Votre référence*

*ISBN:*

*Our file* *Notre référence*

*ISBN:*

**NOTICE:**

The author has granted a non-exclusive license allowing Library and Archives Canada to reproduce, publish, archive, preserve, conserve, communicate to the public by telecommunication or on the Internet, loan, distribute and sell theses worldwide, for commercial or non-commercial purposes, in microform, paper, electronic and/or any other formats.

The author retains copyright ownership and moral rights in this thesis. Neither the thesis nor substantial extracts from it may be printed or otherwise reproduced without the author's permission.

**AVIS:**

L'auteur a accordé une licence non exclusive permettant à la Bibliothèque et Archives Canada de reproduire, publier, archiver, sauvegarder, conserver, transmettre au public par télécommunication ou par l'Internet, prêter, distribuer et vendre des thèses partout dans le monde, à des fins commerciales ou autres, sur support microforme, papier, électronique et/ou autres formats.

L'auteur conserve la propriété du droit d'auteur et des droits moraux qui protègent cette thèse. Ni la thèse ni des extraits substantiels de celle-ci ne doivent être imprimés ou autrement reproduits sans son autorisation.

---

In compliance with the Canadian Privacy Act some supporting forms may have been removed from this thesis.

Conformément à la loi canadienne sur la protection de la vie privée, quelques formulaires secondaires ont été enlevés de cette thèse.

While these forms may be included in the document page count, their removal does not represent any loss of content from the thesis.

Bien que ces formulaires aient inclus dans la pagination, il n'y aura aucun contenu manquant.

  
**Canada**

## Abstract

We have investigated the effect of pairing fluctuations on the normal state of the attractive Hubbard model. This model describes a system of mutually attracting fermions on a lattice. Our work has been motivated by the pseudogap phase found in underdoped cuprates, which we see as a precursor superconductivity effect.

The pairing problem is treated within the Green function formalism. An approximation scheme valid in the low density limit, the T-matrix approximation, is presented, then critically tested in the atomic (0-dimensional) limit of the attractive Hubbard model. In this limit, we discuss the importance of feedback effects, an issue we re-examine later in higher dimensions. A pseudogap is found in the electronic density of states, for values of the interaction parameter ranging from weak to strong coupling, close to the critical temperature in three dimensions and over an extended temperature interval in two dimensions. The energy of the weak coupling pseudogap agrees remarkably well with the zero temperature BCS gap energy. The energy of the strong coupling pseudogap is much larger, especially in three dimensions.

# Acknowledgments

First of all, I would like to thank my supervisor, Dr. Frank Marsiglio, for initiating this work, and for providing greatly appreciated guidance throughout the completion of this degree. For all his support, I am very grateful.

I would also like to thank my parents, Ruxanda and Gheorghe, for their unconditional love and support, and for always encouraging me to follow my dreams. Thanks to my sister, Mihaela, as well, for her 'bubbly' disposition that has always put a smile on my face when I needed cheering up.

Foremost, I want to thank my dear husband, Claudiu, for everything; for his calmness and cool, for keeping me focused, and for helping me not to lose my head. Our beautiful daughter, Mara, has added immeasurability to my life, and has made everything worthwhile.

# Contents

<b>1</b>	<b>Introduction</b>	<b>1</b>
1.1	The Pseudogap state in HTSC . . . . .	2
1.1.1	Experimental evidence . . . . .	2
1.1.2	Pseudogap scenarios . . . . .	6
1.1.3	Precursor pairing . . . . .	8
1.2	The electronic nature of cuprate physics . . . . .	10
1.2.1	The important role of correlations . . . . .	11
1.2.2	The attractive Hubbard model . . . . .	13
1.3	Outline of the thesis . . . . .	15
<b>2</b>	<b>Diagrammatic Approach And The T-matrix Approximation</b>	<b>16</b>
2.1	Preamble to the Green function formalism . . . . .	16
2.2	Normal state formalism - Approaching $T_c$ from above . . . . .	21
2.3	Derivation of the self-energy in the T-matrix approximation . . . . .	23
2.3.1	Definitions and notations . . . . .	23
2.3.2	The equation of motion (EOM) method . . . . .	24
2.3.3	The T-matrix approximation . . . . .	28
2.3.4	Fourier representation . . . . .	31
2.4	Self-consistency, BCS limit and conservation laws in the T-matrix approximation . . . . .	34
2.5	Non-Self-Consistent T-matrix approximation: is it enough? . . . . .	36
<b>3</b>	<b>Atomic Limit</b>	<b>39</b>
3.1	Exact Results . . . . .	39
3.2	T-Matrix Approximation . . . . .	41
3.2.1	NSC T-matrix . . . . .	41
3.2.2	Enforcing self-consistency . . . . .	44
3.3	TPSC Approach . . . . .	45

3.4	Comparison of results . . . . .	47
3.4.1	Chemical potential . . . . .	47
3.4.2	Two-particle correlations . . . . .	48
3.4.3	Spectral properties . . . . .	52
3.4.4	Discussion . . . . .	55
<b>4</b>	<b>Higher Dimensions</b>	<b>58</b>
4.1	The quest for the Pseudogap . . . . .	58
4.2	Imaginary axis calculations - finite size effects . . . . .	60
4.2.1	NSC T-matrix . . . . .	60
4.2.2	Low $\bar{q}$ analytical integration . . . . .	61
4.2.3	High frequency correction . . . . .	70
4.3	Real axis calculations . . . . .	72
4.3.1	Continued fraction approach . . . . .	72
4.3.2	Kramers-Kronig technique . . . . .	73
4.3.3	Numerical treatment - finite size and broadening effects	75
4.3.4	3D density of states - results . . . . .	76
4.4	2D case - self-consistent treatment . . . . .	82
4.4.1	The approximation . . . . .	82
4.4.2	2D density of states . . . . .	83
4.5	Summary . . . . .	89
<b>5</b>	<b>Conclusion</b>	<b>90</b>
5.1	Summary of the T-matrix Approximation . . . . .	90
5.2	Relevance to High $T_c$ Superconductors . . . . .	92
<b>A</b>	<b>Results in the noninteracting limit</b>	<b>101</b>
A.1	The noninteracting Hamiltonian . . . . .	101
A.2	The noninteracting one-particle Green function . . . . .	102
A.3	Pairing susceptibility in the noninteracting approximation . .	105
A.4	The Cooper instability . . . . .	110
<b>B</b>	<b>Analytic continuation and Padé approximants</b>	<b>113</b>
B.1	Analytic continuation . . . . .	113
B.2	Padé approximants - Thiele's reciprocal difference algorithm .	115



# List of Figures

1.1	Schematic phase diagram for hole-doped cuprates . . . . .	3
2.1	Proper self-energy in the Hartree-Fock approximation . . . . .	18
2.2	Proper self-energy in the ladder approximation . . . . .	19
2.3	Generalized interaction and proper self-energy derived with the EOM method . . . . .	29
2.4	T-matrix approximation for the generalized interaction . . . . .	30
3.1	Chemical potential vs. temperature in the atomic limit . . . . .	43
3.2	A comparison of different approximations at $n = 0.3$ in the atomic limit . . . . .	49
3.3	A comparison of different approximations at $n = 0.1$ in the atomic limit . . . . .	50
3.4	Level 1 vs. level 2 of the TPSC approximation at $n = 0.3$ . . . . .	51
3.5	Spectral function in the atomic limit . . . . .	54
3.6	'Effective interaction' in the atomic limit . . . . .	56
4.1	First Brillouin zone for a $8 \times 8$ square lattice . . . . .	63
4.2	Real part of the noninteracting susceptibility vs. $q$ in 1D . . . . .	64
4.3	Real part of the noninteracting susceptibility vs. $q$ in 3D . . . . .	65
4.4	Electronic density vs. temperature in 1D from a non-self-con- sistent calculation . . . . .	67
4.5	Electronic density vs. temperature in 2D from a non-self-con- sistent calculation . . . . .	69
4.6	Electronic density vs. temperature in 3D from a non-self-con- sistent calculation . . . . .	71
4.7	Density of states in 3D for different temperatures . . . . .	78
4.8	Density of states in 3D for two lattice sizes . . . . .	79

4.9	Density of states in 3D for different coupling strengths; comparison of the DOS pseudogap with the BCS superconducting gap at $T = 0$ . . . . .	80
4.10	Density of states in 3D for different values of the broadening parameter . . . . .	81
4.11	Electronic density vs. temperature in 2D from a self-consistent calculation . . . . .	84
4.12	Lower coupling density of states in 2D for different temperatures	86
4.13	Strong coupling density of states in 2D for different temperatures	87
4.14	Density of states in 2D for different coupling strengths; comparison of the DOS pseudogap with the BCS superconducting gap at $T = 0$ . . . . .	88
A.1	Noninteracting pairing susceptibility vs. frequency in 1D for a finite lattice . . . . .	107
A.2	Noninteracting pairing susceptibility vs. frequency in 1D in the thermodynamic limit . . . . .	109
A.3	Upper and lower integration contours in the complex plane . .	111

# List of Abbreviations

$T_c$	critical temperature
$T^*$	pseudogap temperature
SC	superconducting
BCS	Bardeen-Cooper-Schrieffer
BE	Bose-Einstein
HTSC	high temperature superconductors
AF	anti-ferromagnetic
NMR	nuclear magnetic resonance
ARPES	angle-resolved photoemission spectroscopy
STM	scanning tunnelling microscope
FS	Fermi surface
FL	Fermi liquid
RVB	resonance valence bond
1(2,3)D	one (two, three) dimension(s)
DDW	$d$ -density wave
AHM	attractive Hubbard model
QMC	Quantum Monte Carlo
EOM	equation of motion
SVR	Schmitt-Rink, Varma and Ruckenstein
FLEX	fluctuation exchange
TPSC	two-particle self-consistent
NSC	non-self-consistent
FBZ	first Brillouin zone
DOS	density of states

# Chapter 1

## Introduction

The discovery, in 1986, of high- $T_c$  superconductivity in copper oxide compounds by J. G. Bednorz and K. A. Müller [1] re-opened the discussion about the microscopic mechanism responsible for the transition from a normal metal to superconductivity. This problem had been settled very convincingly by Bardeen, Cooper and Schrieffer within their ‘BCS’ theory [2], very successful in describing the physics of conventional metallic superconductors, which undergo such a transition at much lower temperatures. In the case of High Temperature Superconductors (HTSC), the puzzle starts with some peculiar properties in their normal phase.

The undoped cuprates — ‘parent compounds’ — are Anti-Ferromagnetic (AF) insulators. Upon hole doping they become superconductors, some compounds achieving critical temperatures above the boiling point of liquid nitrogen at optimal doping [3] (holding the promise of endless technological applications at the time of their discovery [4]). On the overdoped side relative to the optimal carrier density (the one producing the highest  $T_c$ ), the normal state is reasonably well described by conventional Fermi liquid theory, the superconducting (SC) transition is fairly sharp and the magnitude of the SC gap (the maximum gap, since the gap has momentum dependence) scales with  $T_c$  [5], similarly to conventional materials. Decreasing the number of charge carriers beyond the optimal value has rather drastic effects: a ‘pseudogap’ appears in the normal state at a temperature  $T^*$  greater than the SC transition temperature, and the maximum gap *increases* with decreasing hole concentration, while  $T_c$  is suppressed [6]. The pseudogap signature on both static and dynamic properties has been documented experimentally to a great extent, and its presence in most cuprates is well established [7]. The

origin of such unusual normal state behavior is still the subject of heated debate, as is the mechanism underlying high- $T_c$  superconductivity and the possible connection between them.

## 1.1 The Pseudogap state in HTSC

### 1.1.1 Experimental evidence

Experimental indication of a pseudogap emerged within the early search for a superconducting gap in the hole-doped cuprate materials. Early experiments failed to find the expected signatures of an energy gap, namely the absence of quasiparticle excitations below an energy  $2\Delta$  appearing abruptly at the superconducting transition temperature  $T_c$ . Instead, the depression of excitations was incomplete and often started well above  $T_c$  in the normal state. It is well known now that this is the consequence of two basic properties of high-temperature superconductors: the  $d$ -wave character of the SC gap and the presence of a partial gap in the normal state. Both these properties have been solidly confirmed by the extensive experimental investigation of the cuprates that followed the initial experiments (see Ref. [7] for a review).

Many experiments performed on cuprates have found evidence for a pseudogap; both the loss in electronic entropy, reflected in thermodynamic quantities such as the electronic spin susceptibility (probed by Nuclear Magnetic Resonance (NMR) [8]) and specific heat [9], and the reduction in scattering rate suggested by transport properties such as dc electrical resistivity [10], thermal conductivity [11], magnetoresistance and Hall effect [12], are consistent with a depletion of electronic states near the Fermi energy. Further confirmation comes from spectroscopic measurements such as optical conductivity [13], vacuum tunneling spectroscopy [14] and Angle-Resolved Photo-Emission Spectroscopy (ARPES) [15, 16].

ARPES is probably the most ‘revealing’ of all experimental probes, because it can provide information about the angular dependence of both the superconducting gap and the normal state pseudogap. The underlying principle is simple: light is shone on the surface of the sample, an electron in an occupied state absorbs a photon and is emitted out of the sample *at an angle*, depending on its initial energy. The existence of the surface breaks the translational invariance in the  $z$ -direction (perpendicular to the sample surface), so the  $k_z$  component of the momentum is not conserved. However,

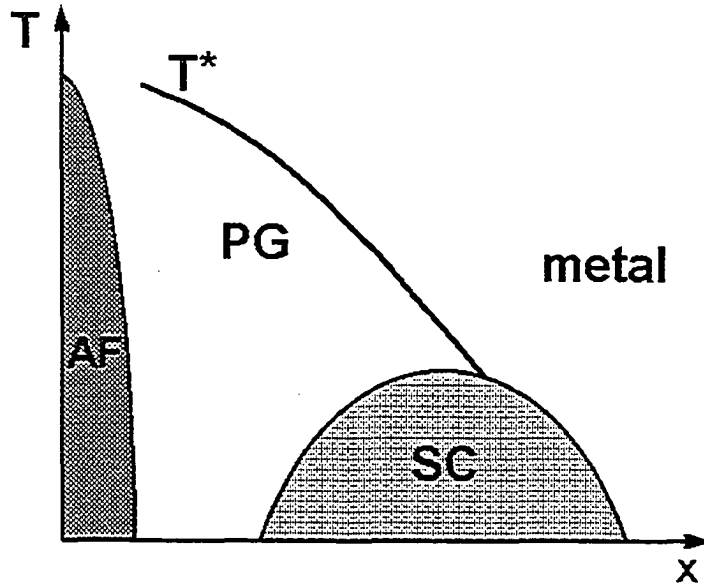


Figure 1.1: Schematic phase diagram for hole-doped cuprates ( $x$  indicates the concentration of doped carriers), indicating the anti-ferromagnetic (AF), superconducting (SC) and pseudogap (PG) regions.

two-dimensional translational invariance in the directions parallel to the surface is still preserved, and thus  $k_{\parallel}$  is conserved in the emission process. This allows one to obtain the in-plane momentum of the initial state by identifying it with the parallel momentum of the emitted electron. Because of their quasi 2D nature, in many cases with no observable  $k_z$  dispersion, the cuprates are very well suited to this technique, which is able to provide a direct image of the occupied electronic states as a function of momentum. This made ARPES the tool of choice for investigating the high  $T_c$  cuprates, leading to a more and more detailed picture of the electronic structure in these materials, as the energy and angular resolution have continued to improve providing greater and greater accuracy (for a survey of the extensive ARPES literature over the last decade see Ref. [17, 18]).

A conventional Fermi surface is seen above the superconducting transition temperature  $T_c$  on the overdoped side of the phase diagram - schematically shown in Fig. 1.1 - and above  $T^*$ ; however, for  $T_c < T < T^*$  the number of states at the Fermi energy is slowly suppressed along all directions

in momentum space except along the Brillouin zone diagonals. Below  $T_c$ , this suppression in spectral weight evolves smoothly into a  $d$ -wave superconducting gap, as suggested by both its magnitude and momentum space structure [19]. Interestingly, the maximum gap does not appear to change significantly when the temperature is raised. This behavior is consistent with other spectroscopic probes such as vacuum tunneling spectroscopy [14] and  $c$ -axis optical conductivity [20], which have found the gap energy to be temperature independent, the gap filling in as the temperature increases (in contrast to the evolution of the gap around the Fermi surface in momentum space, where the gap energy does change, going to zero - ‘closing’ - as the zone diagonal is approached).

The ARPES lineshape is complex, and indicates a variety of effects, reflecting the many competing degrees of freedom that are a characteristic of the cuprate materials. As a consequence, often it has been difficult to unequivocally interpret some of the features present in the data, from those related to crystal structure details to those explained in terms of quasiparticles coupling to collective modes. This has led to oftentimes conflicting theoretical views, especially in the very underdoped regime, where there is still no clear picture of how exactly a doped Mott insulator becomes a metal and, upon cooling, a superconductor. There have been, however, many topics on which ARPES results have obtained a general consensus, with a profound impact on our understanding of the physics of HTSC; we list below some of the most relevant:

- electronic correlations are very important in the cuprates;
- the doping evolution of the electronic structure is qualitatively the same in all hole-doped cuprates;
- there is a well defined Fermi surface (FS) above the superconducting transition in the overdoped regime;
- a normal state pseudogap opens at  $T^* > T_c$  in the underdoped regime;
- the pseudogap evolves smoothly through the SC transition into the superconducting gap; however, in contrast to the incoherent spectrum in the normal state, a sharp quasiparticle peak appears below  $T_c$ ;
- both the pseudogap and the superconducting gap seem ‘tied’ to the FS (that is, the FS seen in the metallic phase coincides with the minimum

gap locus in the ‘gapped’ phases);

- the pseudogap magnitude and momentum structure are very similar to those of the superconducting gap;
- the overall  $d$ -wave symmetry of the superconducting gap supports the universality of the pairing nature in the HTSC;

While recognizing its important contribution, it would be misleading to leave the impression that the ARPES investigation does not have its share of limitations. On top of the obvious one coming from the high purity requirements for the surface (easier to satisfy for some materials, such as the Bi-based compounds Bi2212 and Bi2201, but not a simple matter for others, which do not have the advantage of a natural cleavage plane), other complications come from the strong inelastic background, and from the sometimes strong lineshape dependence on the photon energy. Also, ARPES can only access the occupied states, and some sort of symmetrization is necessary in order to extract the entire electronic spectrum. All these issues can make the interpretation of the data difficult and corroboration with other experiments is vital.

An experimental probe that has known a revival lately is tunneling spectroscopy. This technique has played a crucial role in the investigation of conventional superconductors, and has confirmed the presence of a pseudogap in the cuprates early on [14]. Although ARPES has been preferred for its being both a momentum and a frequency resolved probe, tunneling has the advantage of a much better energy resolution, and that of being able to see unoccupied states as well as occupied ones. More recently, Davis’s group at Berkeley have perfected the technique and, through Fourier analysis of the extensive and detailed spatial information collected in many STM scans, have been able to uncover details about the momentum space structure [21].



### 1.1.2 Pseudogap scenarios

Given its ubiquitous presence in the cuprates, understanding the origin of the pseudogap phase is critical in order to achieve an adequate description of high  $T_c$  superconductivity. Consequently, a variety of models have been proposed attempting to elucidate the nature of this state. A review of the theoretical work, accompanied by relevant experimental evidence, can be found in Ref. [22], where the pseudogap is discussed in the more general context of the rich physics of the cuprate materials.

The pseudogap scenarios can be broadly divided into two classes: those which see the partial gap opening in the normal state as a precursor effect to superconductivity, and those which see it as the effect of a competing instability.

Within each class, the origin of the pseudogap can be seen quite differently. For example, among the precursor superconductivity scenarios, there is one category which places the superconductivity in the cuprates at the crossover between the BCS (large pair) and Bose-Einstein (small pair) descriptions. This view can be traced back to the work of Leggett [23], and is inspired by the small coherence length  $\xi$ , naturally associated with modest size Cooper pairs. Models in this category relate the pseudogap to pairing correlations above  $T_c$ . This is the view we will adopt in this thesis. We base our choice to a great extent on the abundance of experimental evidence suggesting that the superconducting gap and the normal state pseudogap are intimately related, particularly ARPES evidence.

A second category within the ‘precursor’ class places the emphasis on phase fluctuations, and is based on the low plasma frequency  $\omega_p$  (related to the low carrier density in the cuprates). According to this line of thought, the amplitude of the order parameter is established at  $T^*$ , while phase coherence occurs at the much lower temperature  $T_c$ . We mention here the picture of mesoscopically established regions of superconductivity, first proposed by Emery and Kivelson [24].

One model with subtle differences from the ‘pairing correlation’ hypothesis is the Resonance Valence Bond (RVB) scenario, introduced by Anderson [25]. In this 2D model incoherent pairing applies to opposite spins, localized on neighboring sites for energetic reasons, effectively leading to a spin gap. This magnetic order is frustrated by doped holes, which are current carriers and contribute to the superfluid density. Thus, this picture leads to a realization of spin-charge separation, with a complete decoupling of the

excitation gap (decreasing linearly with doping) from the order parameter (increasing linearly with doping). A finite temperature extrapolation will associate the ‘pairing’ temperature scale with the spin gap, and the phase coherence temperature will be proportional to doping. This model has certainly been controversial, and the physical reality of ‘holons’ and ‘spinons’ yet to be confirmed. We mention it here for its effort to address not only the pseudogap phase but the entire phase diagram from the Mott insulator to the overdoped regime. Some experimental backup for this picture has been offered by the relatively strong gap seen in NMR experiments (probing the spin channel), compared to the weaker gap-like depression observed in the in-plane infrared conductivity (the in-plane drop in resistivity is seen as due to less states available for the doped holes to scatter off of, as the spins pair up and become gapped). In contrast, the large effect seen in the c-axis transport measurements is explained by the necessary recombination of spins and charges into real electrons in order to tunnel between planes (spin-charge separation, being a 2D effect, only occurs within a plane).

Not unrelated to the RVB scenario is the stripe picture, where doped holes form 1D ‘rivers of charge’, balancing the frustration of the magnetic order with the Coulomb repulsion of the holes clumping together. While it is not yet established if Fermi liquids are inherently unstable in 2D, they definitely are in 1D [26]. Thus, such models would naturally lead to non-Fermi liquid behavior, and that’s why the 1D physics of the stripes is so attractive. In this scenario the pseudogap is due to the spin gap present in the magnetic insulating domains between stripes. Below some temperature the stripes phase coherently lock via Josephson coupling, and the system crosses over from a 1D non-Fermi liquid normal state to a 3D coherent superconducting state. Experimental evidence for the presence of stripes has been provided by inelastic neutron scattering experiments for LSCO [27], but it has proved hard to confirm their presence in other cuprates. The stripe scenario has common ground with the Emery and Kivelson model mentioned earlier.

One of the leading alternates to the preformed pairs picture is the magnetic precursor scenario. This approach advocates spin fluctuation mediated superconductivity in the cuprates, and sees the pseudogap as the result of spin correlations anticipating the AF regime [28]. The precursor to the AF state is also discussed in Ref. [29], while a detailed agreement with experiments can be found in Ref. [30]. For spin fluctuations, the associated ordering grows with underdoping, leaving less and less states at the Fermi surface available for pairing. This leads to an increasing suppression of the

SC transition temperature on the underdoped side. In fact, the presence of two effects found in ARPES studies, a ‘higher energy pseudogap’ and a ‘leading edge pseudogap’ (evident from the earliest studies, but not differentiated until later [18]), may reconcile the precursor pair hypothesis with the competing magnetic order scenario, in that the leading edge pseudogap seems to be a precursor to the superconducting gap, whereas the high energy pseudogap is a precursor to the magnetic insulating gap. The two energies scale together with doping, demonstrating the close relation of magnetic and pairing correlations in the cuprates. Based on the spectroscopic data, though, it is hard to find support for a number of theories advocating a competing phase with true long range order, often involving a quantum critical point [31, 32]. In these scenarios, the  $T^*$  line crosses the  $T_c$  line and into the SC ‘dome’, vanishing on the  $T = 0$  axis near optimal doping. In support to these theories, Tallon and Loram [33] revisit the experimental evidence on the pseudogap and claim to have found support for the existence of a critical doping point just beyond optimal doping. Notably, more recent circularly polarized ARPES experiments [34] find evidence for broken time reversal symmetry, predicted by a competing scenario based on orbital currents, as proposed by Varma [35]. Orbital spin currents are also associated with the  $d$ -Density Wave (DDW) model promoted by Laughlin and collaborators [36], although the polarized ARPES experiment seems to favor the Varma picture. While more experimental investigation might be desirable in order to confirm this interpretation of the data, two things are quite clear: the physics of the cuprates is very complex, and the last word on the origin of the pseudogap has not been spoken yet.

### 1.1.3 Precursor pairing

Superconductivity in the BCS theory arises through the formation of an order parameter, characterized by both an amplitude and a phase [2]. The amplitude of the order parameter is associated with pairing of electrons, leading to a gap in the single-particle excitation spectrum (the superconducting gap); phase coherence refers to the macroscopic occupation of the zero center of mass momentum pair state, leading to superflow properties. It is a very special feature of this theory, and of the conventional metallic superconductors so well described by it, that the two aspects occur at the same temperature. Fluctuations can impact both the amplitude and the phase, and have been suggested to be relevant to the anomalous normal state properties of the high

temperature copper oxide superconductors.

The HTSC are different from the more conventional materials in many ways, particularly in the underdoped regime, as we hope to have made clear; however, superconductivity in these compounds exhibits the same two basic (and defining) properties: zero resistance and Meissner effect. The superconducting objects have a  $2e$  charge, indicating that pairs are formed. These pairs, though, have much less spatial extent, *i.e.*, the coherence length is much shorter than those in the conventional superconductors. This has led to the idea of preformed bosonic pairs above  $T_c$ .

In fact, speculation about the possibility of Bose condensation, with pairs existing above the superconducting transition temperature, predates the discovery of the cuprates, and it was first brought forth in an article by Eagles [37]. After the presence of the normal state pseudogap became a well-established fact, a number of models [38, 39] trying to explain it have proposed a Hamiltonian containing a mixture of free fermions and bosons, with terms allowing for pairing of fermions into bosons and the decay of pairs into individual fermions. Such models are attractive because they are intuitively simple and lend themselves to analytical treatment. Their applicability is limited though, because they consider the pairs to be structureless point bosons, strictly valid only in the low density, strong coupling limit.

A more convenient starting point is a conventional, fermionic Hamiltonian that provides a standard pairing interaction. This approach has the advantage that the coupling strength may be varied, providing access not only to the extreme strong coupling limit, where two electrons already form a well defined boson at the critical temperature (where the bosons acquire phase coherence), but to the weak coupling regime as well, in an attempt to recover the BCS theory. Moreover, the ARPES studies attest the presence of a large FS even in the underdoped regime, consistent with a degenerate Fermi system, albeit one with non-Fermi liquid behavior. This would place the cuprates in the intermediate regime, rather than the Bose condensation (local pair) limit (in this limit, the chemical potential would lie beneath the bottom of the energy band).

It is this last approach which is assumed in this thesis. We will reserve extensive space to expand on the history of pairing fluctuations ideas in a subsequent chapter, where we will also present how a many-body framework may be formulated in an effort to understand this physics.

## 1.2 The electronic nature of cuprate physics

The normal state of a conventional metallic superconductor is a Fermi liquid, *i.e.*, most properties of the system can be described by a collection of independent quasiparticles (electrons shielded by strong Coulomb interactions), by virtue of adiabatic continuity; this implies the presence of a well-defined Fermi surface, the important excitations being those of quasiparticles near this energy level.

The BCS theory relies on the existence of a filled Fermi sea: the Cooper pairing idea considered two quasiparticles sitting in empty states above it. Cooper showed that even an infinitesimal attraction would lead to formation of bound electron pairs [40]. That the attraction could be provided by phonons had already been suggested by Frölich in 1950 [41]. The lattice-mediated attraction is local in space and retarded in time, although the dynamics did not make it into the original BCS picture, where the phonon contribution is simplified to a density of states cut-off at some characteristic Debye energy  $\omega_D$ . The effect of electrons coupling to dynamical phonons was addressed later, starting with Migdal [42] and Eliashberg [43].

In the overdoped regime, the normal state of the copper oxide materials fits well the FL description. The superconducting state is reasonably well described by the BCS picture, with two important caveats: the interaction has momentum dependence, as suggested by the d-wave symmetry of the SC gap, and the characteristic frequency refers to a different bosonic excitation, most likely electronic in origin [25]. We note here, though, that the possible contribution of phonons was speculated by Lanzara and collaborators in relation to a universal ‘kink’ found in the quasiparticle dispersion along the zone diagonal [44]. This effect was also investigated by our group [45]. We devised an inversion procedure in order to extract the underlying bosonic spectrum from the dispersion data. We were able to obtain the real part of the electron self-energy directly from the dispersion curves; the imaginary part was then calculated by performing a Kramers-Kronig integral. With the standard approximations [46, 47], one can relate the imaginary part of the self-energy to the underlying electron-‘boson’ spectrum. The result of the inversion indicated a frequency domain consistent with the phonon picture [44]. However, we found a ‘tail’ of high frequency spectral weight, a peculiar feature for a phonon spectrum. It is true that spin fluctuations are expected to have significant spectral weight at higher frequencies; in fact, significant spectral weight persists at frequencies much higher than the data indicates. Thus we

were unable to definitely rule in favor of either alternative.

Clearly though, in the underdoped regime the anomalous normal state attests for a departure from Fermi liquid behavior. A logical extension is that one must go beyond BCS theory in order to interpolate between this anomalous normal state and the superconducting state in the cuprates. Far from clear is exactly how this is to be done. But no matter what the most successful theory might turn out to be, one thing is certain: strong electronic correlations in these materials must be properly accounted for. To make our point more poignant, we will discuss next their basic electronic structure.

### 1.2.1 The important role of correlations

The HTSC are highly anisotropic, layered structures. The unit cell consists of a sequence of layers, of which one at least is a  $\text{CuO}_2$  plane. The planes are separated by the so-called *charge reservoir* layers, because by changing their chemical composition, either by element substitution or by varying the oxygen content, carriers are effectively doped into the  $\text{CuO}_2$  planes. The resulting electronic structure is quasi two dimensional, with weak dispersion along the  $z$ -axis.

Band structure calculations based on a square lattice with three orbitals (Cu  $3d_{x^2-y^2}$  and O  $2p_x$  and  $2p_y$ ) at half-filling (*i.e.*, one electron per Cu  $3d_{x^2-y^2}$  orbital, corresponding to zero doping) predict metallic behavior and a Fermi sea with a volume equal to half of the Brillouin zone. (In real 3D materials the inter-plane layers can cause distortions, resulting in in-plane anisotropy that can be significant in some compounds, such as YBCO123.) In reality, all undoped cuprates are AF insulators. This contradiction reflects the importance of correlations and the failure of the Fermi liquid theory based on the independent quasiparticle picture. The reason for this failure lies in the on-site electron-electron repulsion  $U$ , much greater than the bandwidth  $W$ , causing the conduction band to split into the upper and the lower Hubbard bands, separated by an optical gap of a few eV. For most of the transition metal oxides the charge transfer gap  $\Delta$  is smaller than  $U$ , and these compounds are more appropriately described as *charge-transfer insulators*, rather than Hubbard-Mott insulators. Therefore it has been suggested that a proper description should explicitly consider Cu  $3d_{x^2-y^2}$  as well as O  $2p_x$  and  $2p_y$  orbitals, as in the three-band extended Hubbard model [48, 49]. In the case of cuprates, however, there is a fair amount of hybridization, the relevant energy being the bonding-antibonding splitting involving the quantum mechanical

mixture of Cu and O orbitals. As speculated earlier by Anderson [25], it is the Cu-O antibonding band which ‘Mott-Hubbardizes’. The one-band Hubbard model captures the essential physics of the cuprates, since the lowest electron removal states, corresponding to the O-derived Zhang-Rice singlet band [50], can be looked upon as an effective lower Hubbard band, and an in-plane Cu-derived band as the upper Hubbard band. When the on-site Coulombic repulsion is much larger than the characteristic hopping  $t$ , the upper Hubbard band is projected out and the effect of  $U$  becomes virtual [51]. In this case the Hubbard model reduces to the  $t - J$  model, where  $J \propto t^2/U$  is a superexchange interaction between the Cu spins. Thus, at half filling, the electrons gain kinetic energy by undergoing virtual hopping to neighboring sites, and because the Pauli principle forbids hopping for parallel spins, the ground state is AF, leading to an energy savings of the order  $t^2/U$  from second order perturbation theory. The  $t - J$  model is considered the minimal model for the cuprates, as it furnishes an AF undoped ground state and it has been shown to produce a  $d$ -wave SC state away from half filling [52]. However, it is not generally agreed upon. For instance, Varma [35] derives the orbital current state that he associates with the pseudogap by considering the full three-band Hubbard model, where non-trivial phase factors between the three bands become possible upon projection onto the low energy sector.

Our objection to the  $t - J$  model is more a practical one, since this model is not directly amenable to many-body calculations, and not all parameter space is easily accessible. We choose instead to focus on the physics leading up to superconductivity and not be concerned with the details related to magnetic correlations. We will adopt the general consensus that the SC state is isomorphic to a BCS ground state of  $d$ -wave pairs, although we will not consider the momentum space structure for now. We assume that pairing is the result of an attraction between electrons, without worrying about its possible origin. The question we want to ask first is much simpler: in a system of many electrons provided with an attractive interaction, does pairing play a role in shaping the normal state?

### 1.2.2 The attractive Hubbard model

The simplest lattice model that allows one to study the pairing problem is the Attractive Hubbard Model (AHM). The Hamiltonian is given by:

$$\hat{H} = -t \sum_{\langle ij \rangle, \sigma} (\hat{c}_{i\sigma}^\dagger \hat{c}_{j\sigma} + h.c.) - |U| \sum_i \hat{n}_{i\uparrow} \hat{n}_{i\downarrow} \quad (1.1)$$

Here  $\hat{c}_{i\sigma}$  ( $\hat{c}_{i\sigma}^\dagger$ ) is the creation (annihilation) operator for a particle (electron or hole) on site  $i$  with spin  $\sigma$ ,  $\hat{n}_{i\sigma} = \hat{c}_{i\sigma}^\dagger \hat{c}_{i\sigma}$  is the number operator, and  $\langle ij \rangle$  restricts the sum to nearest-neighbors only. The first term, the kinetic energy term, is proportional to the nearest-neighbor hopping amplitude  $t$ , and the second term, the negative- $U$  Hubbard term (different from the on-site Coulomb repulsion  $U$  in the regular Hubbard Hamiltonian), provides the on-site attraction between two electrons. This attraction is a useful simplification that bypasses the controversy about the pairing mechanism in cuprates. But despite its simplicity, the AHM Hamiltonian remains non-trivial to solve. We have to mention here the remarkable work of Lieb and Wu, who provided, in one dimension, an exact solution for all parameter values and all sizes, including the thermodynamic limit (relevant for describing real solids) [26]. Their solution demonstrated, for the first time, the possibility of ‘breaking’ the electron into separate spinless charge and neutral spin excitations. Another important result was that despite the decay of the electronic excitations into a number of ‘pieces’, the system still had a Fermi surface (in fact, two Fermi points in 1D), at the same location in momentum space, in agreement with Luttinger’s theorem [53]. Lieb and Wu studied the repulsive Hubbard model; nonetheless, this can be mapped into the AHM, as outlined by the authors in Ref. [26].

In higher dimensions, however, there are few exact results available, apart from two limiting cases: the zero- $U$  and zero- $t$  limit. The  $U = 0$  limit simply describes free electrons on a lattice, and is presented in Appendix A; the  $t = 0$  limit represents the extreme strong coupling limit, when the hopping becomes insignificant, and the system consists of a collection of uncorrelated sites (0-dimensional limit). We will discuss this limit in Chapter 3.

A functional integral approach, developed for a closely related continuum model [54, 55], was discussed in the context of the AHM by Randeria [56]. This approach led to an interpolation scheme for  $T_c$  that reproduced correctly both the weak coupling and the strong coupling limits. The weak coupling  $|U|/t \ll 1$  limit is well described by the BCS theory, with large-size pairs that



dissociate and lose coherence at the same temperature  $T_c \sim t \exp(-t/|U|)$ . Above  $T_c$  one has a ‘well-behaved’ Fermi liquid. In the opposite, strong coupling  $|U|/t \gg 1$  limit, Bose-Einstein condensation is the appropriate theory, *i.e.*, the ground state is a condensate of hard core bosons that lose coherence at  $T_c \sim t^2/|U|$  but remain well-defined as tightly bound pairs upon heating up to a much higher temperature  $T^* \sim |U|$ . However, the interpolation scheme is least reliable in the intermediate coupling regime, which is, of course, the most interesting. At  $T = 0$  it was found [55] that a mean field approximation is able to capture the physics of the SC ground state, and excitations, all the way from the BCS to the composite boson limit. However, such an approximation fails to describe, even qualitatively, the normal state physics beyond the weak coupling BCS limit.

For 2D systems, a number of Quantum Monte Carlo (QMC) studies have been done on the AHM [57]. Such studies have also been done in 3D [58]. They have been very useful in elucidating the nature of the normal state, and they have indicated, in the coupling regime of interest, a departure from the FL behavior consistent with experimental observations. While their contribution cannot be contested, one wishes to find analytically tractable approaches that may be applicable to more realistic models. After all, the ultimate goal is to extend the treatment to models with a momentum dependent electron-electron interaction, in order to properly reproduce the *d*-wave nature of the SC gap. There is no known simple model with a *d*-wave SC ground state amenable to QMC calculations; the main reason is the well-known fermion sign problem [59]. Thus, it is desirable to find a generic prescription to make approximations, ideally a scheme that can be derived rigorously and improved systematically. Developing a formalism that meets such requirements makes the subject of Chapter 2.

## 1.3 Outline of the thesis

In this thesis we will adopt the precursor superconductivity line of thought and investigate the effect of pairing correlations on the normal state of a system of lattice fermions provided with an attractive interaction. The remainder of the thesis is structured as follows:

### Chapter 2

- Within the Green function formalism, we look for approximate schemes that include two-particle correlations. We employ the Equation of Motion (EOM) method to select an infinite subset of diagrams in the diagrammatic expansion of the one- and two-particle propagators; in the dilute limit, the EOM yields the so-called T-matrix theory, in which only the particle-particle channel is retained (to infinite order). The limitations of the EOM prescription, together with constraints on any generalization, are subsequently discussed; in this context, we will emphasize the importance of feedback effects on the T-matrix.

### Chapter 3

- We will test different approximations in the zero- $t$  (atomic) limit of the AHM, where an exact solution exists. In this limit, one particular T-matrix formulation that keeps the feedback effects to a minimum is the most successful when compared with the exact results.

### Chapter 4

- We will use the T-matrix approximation to calculate spectral properties of the fermionic system in two and three dimensions. While a self-consistent treatment is not deemed necessary for the 3D case, we will include minimal feedback on the T-matrix for the 2D calculations. A pseudogap is found in the density of states, *even for weak coupling*, close to  $T_c$  in 3D and over a broader temperature range in 2D.

### Chapter 5

- We will present conclusions of our work, ending with a discussion about its relevance to the high  $T_c$  materials.

## Chapter 2

# Diagrammatic Approach And The T-matrix Approximation

In the **Introduction**, we have alluded to the fact that, while real physical systems are generally very complex, one's efforts to understand such systems in all the details are both futile and impractical. In order to make progress, it is important to recognize the most relevant features one is trying to capture in a theory and find simple models to describe them. Thus we have argued that the AHM with its simplified on-site attraction has the merit of providing the electrons with the 'means' to form pairs, which we know is essential to superconductivity. And yet, despite its simplicity, a full description of this model is not available for all strengths of the interaction and in all dimensions. In this chapter, we will discuss how different diagrammatic schemes can be employed to treat the coupling regime of interest for this model.

### 2.1 Preamble to the Green function formalism

The *Green function* formalism is useful in treating models that cannot be solved by conventional theoretical techniques aimed at finding the full wave function. The Green functions (or *propagators*) contain the most important physical information about interacting many-body systems, such as the ground state energy and other thermodynamic functions, the energy and lifetime of excited states and the linear response to external perturbations. Unfortunately, finding the exact Green functions is no easier than the original

problem of finding the full wave function.

The usual approach is to separate the problem into a part that can be solved exactly, described by a known Hamiltonian  $H_0$ , and a ‘perturbing’ potential  $V$ . Then, one proceeds with the perturbation theory, best formulated in the concise and systematic language of Feynman rules and diagrams. While there are a few cases in physics where the first few terms in the perturbation series will suffice, in the vast majority of problems the adequate description of an interacting system requires evaluating the Green function to all orders in the interaction potential. Dyson’s equation provides a formal way to do that and, more importantly, is independent of the original perturbation series. This allows for the possibility of non-perturbative approaches, with important implications, given the lesson learned from superconductivity, that the properties of many-particle systems may be nonanalytic in the coupling constant. The difference between the full Green function  $G$  and the noninteracting one  $G^0$  (associated with the noninteracting part of the Hamiltonian) is encapsulated in a function  $\Sigma$ , called the proper self-energy. Iterating Dyson’s equation yields the perturbation expansion to any arbitrary order in the perturbation parameter.

In principle, Feynman-Dyson perturbation theory produces the exact Green function to all orders in the interaction potential, but it is very often impossible to pursue such a calculation in practice. Most of the times we must resort to non-exact techniques, and one wishes to find controlled, systematic ways to make approximations.

One approach is to retain the first few diagrams in the perturbation theory and to *reinterpret* the particle lines to represent the *full* Green function, instead of the noninteracting one. This way it includes infinite orders in the perturbation potential. Within these schemes the Green function is expressed in terms of itself, and therefore requires a *self-consistent* determination. An example of such an approximation is the Hartree-Fock approximation, illustrated diagrammatically in Fig. 2.1, following Ref. [60]. Expressing the Green function in terms of a complete set of (unknown) single-particle wave functions and energies will lead to the well-known Hartree-Fock equations - a system of coupled equations that allows the self-consistent determination of these wave functions and energies.

A different approach is to select an infinite subset of diagrams, expressed in terms of the noninteracting Green function  $G^0$  and perform the summation to all orders. We will give here the example of the *ladder* approximation, appropriate for a dilute Fermi gas, where  $k_F \rightarrow 0$  ( $k_F$  being the radius of the

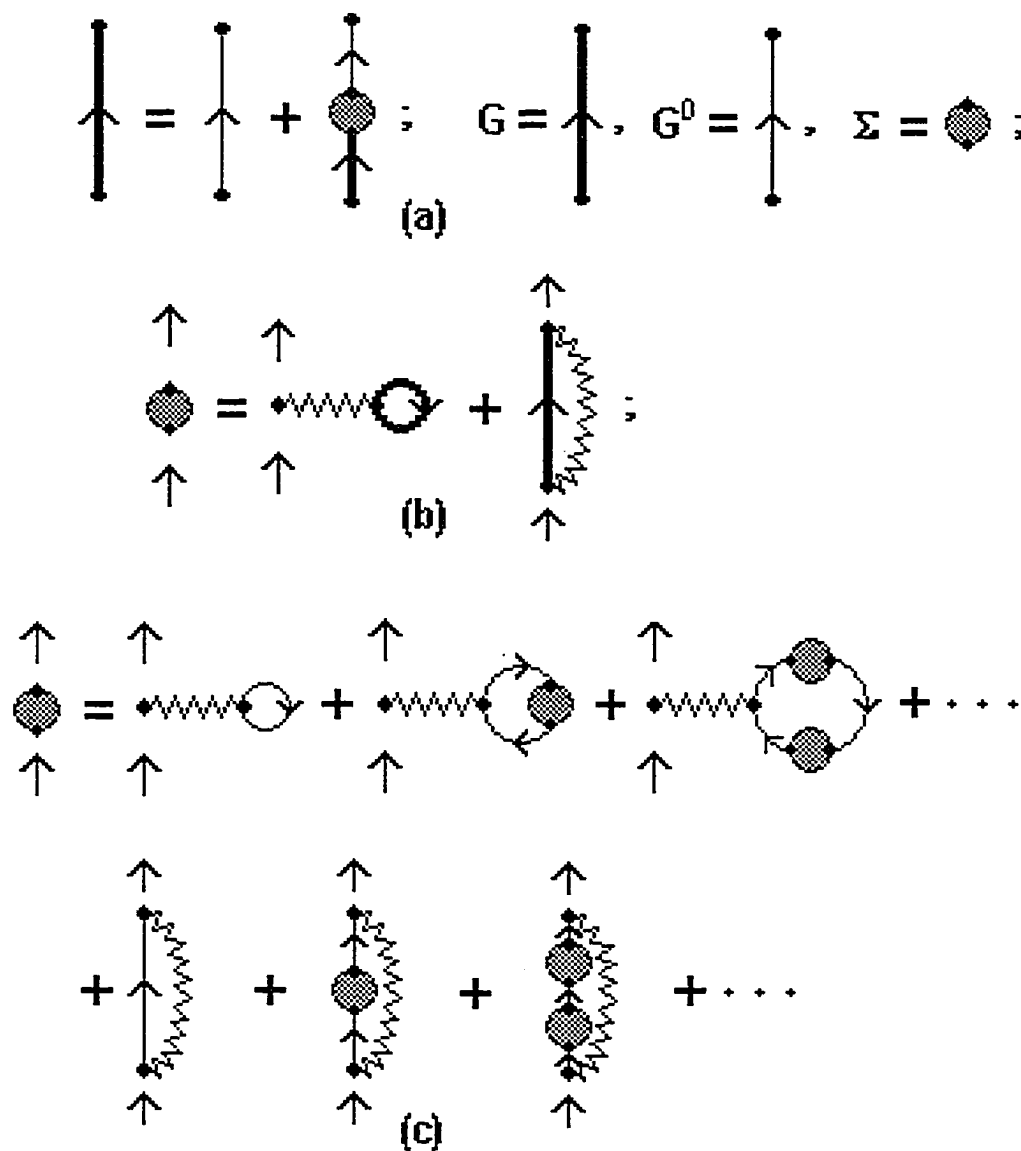


Figure 2.1: (a) Dyson's equation; (b) Self-consistent proper self-energy in the Hartree-Fock approximation; (c) Series for the proper self-energy in the Hartree-Fock approximation (adapted from Ref. [60]). Note that for the AHM, since the on-site potential only allows particles of opposite spin to interact, the exchange part is absent (second term in (b), second line in (c)) and one has only the Hartree bubble diagrams (first term in (b), first line in (c)).

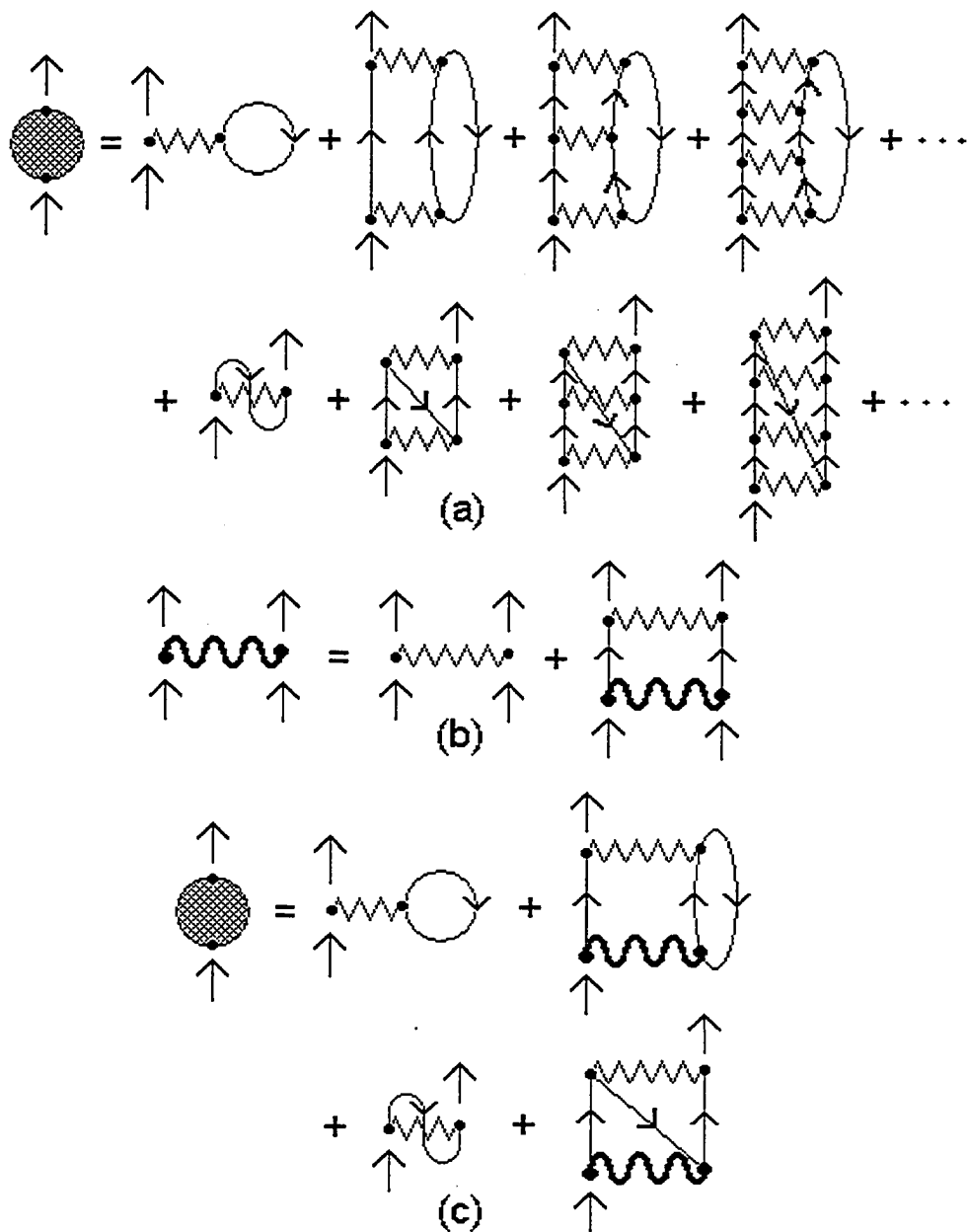


Figure 2.2: (a) Series for the proper self-energy in the ladder approximation; (b) Generalized interaction; (c) Proper self-energy in the ladder approximation, in terms of the generalized interaction. Again, for the AHM the exchange part is absent (second line in (a) and (c)).

Fermi sea in momentum space). In this case, even if the interaction parameter is too strong to lead to a convergent perturbation series, the product  $k_F a$ , where  $a$  is the scattering length (related to the interaction strength), can be treated as an additional small parameter. For such a system, the average distance between fermions is much greater than the range of interaction and thus the two-particle collisions are the leading event. Analogously to the Hartree-Fock case where the average effect of the interaction with all the other particles was included to improve the single-particle picture, the ladder approximation considers the effect that the many-particle background has on an interacting pair of particles. This background limits the intermediate states available to the two particles involved in the scattering event. They may suffer any number of collisions *outside* the Fermi sea, before they are de-excited back into it. This effect translates into corrections of the order  $(k_F a)^2$  to the ground state energy (the Hartree-Fock correction is of the order  $k_F a$ ). Any scattering involving an intermediate particle-hole pair adds an extra power of  $k_F a$  and may be neglected. Such a process really represents the transfer of an additional particle inside the Fermi sea, filling the original hole and leaving a new one in its place. Thus it leads to corrections of the order  $(k_F a)^3$ , negligible in the dilute limit.

For completeness, we note that there are instances of dilute Fermi systems where the treatment of  $k_F a$  as a small parameter may no longer be adequate. We refer, for example, to the work of Pieri and Strinati on a general Fermi gas model with a point contact attractive interaction [61]; the same physics has been discussed in the context of superfluid pairing, near a Feshbach resonance, in ultra-cold Fermi gases trapped in electromagnetic fields [62]. The main idea is that, when going from weak to strong coupling, the scattering length changes from being negative to positive, and it does so by going through a *divergence* when the coupling is sufficiently strong for a bound state to appear. Beyond that point, Pieri and Strinati [61] argue, it is the residual interaction between composite bosons that determines the ‘diluteness’ condition, and not the original attraction between fermions. In that case, the ladder approximation is not expected to remain valid.

The ladder approximation is also known as the T-matrix approximation, by analogy with the well-known T-matrix for the scattering of two independent particles. The proper self-energy in the ladder approximation is shown in Fig. 2.2.

The ladder sum in the particle-particle (Cooper) channel was used by Thouless [63] to elucidate the nature of the superconducting instability, and

allowed the possibility to study the superconducting transition away from the weak coupling limit for which BCS was initially designed. This demonstrates that, even in the case of superconductivity, where the order parameter is non-analytic in the interaction strength and no perturbative treatment with respect to the normal state of a system of many fermions could converge to the superconducting state, perturbation theory may still find its uses.

The two approaches outlined above can be combined, in the sense that one may select an infinite set of diagrams *and* reinterpret some of the particle lines to represent the full Green function, thus requiring a self-consistent determination. We will further expand on the issue of how to choose *which* of the particle lines are to be changed when we discuss the T-matrix approximation for the AHM.

## 2.2 Normal state formalism - Approaching $T_c$ from above

Before we proceed with presenting the formalism, we want to set the framework, based on what we hope to accomplish.

One could say that ‘modern’ interest in the influence of pair fluctuations on the superconducting transition was stimulated by Leggett [23]. He used a variational approach to show that for a dilute gas of fermions with an attractive interaction there was a smooth crossover from the BCS ground state with overlapping Cooper pairs space to a BE condensate of tightly bound pairs. Some years later, this work was extended to lattice models and, more importantly, finite temperatures by Nozières and Schmitt-Rink [64]. Using a diagrammatic formulation, they showed that, within their approximation, the transition temperature  $T_c$  evolves smoothly as a function of coupling strength from the BCS to the BE limit. The problem of the BCS-BE crossover was reviewed in detail by Randeria [56], using a variety of theoretical techniques. The main conclusion of his work followed along the same lines, that there is only one phase transition to a state with long range order, the superconducting transition, which in the strong coupling limit was properly described by the Bose condensation of electron pairs.

But the nature of the transition in the two limiting cases is rather different. In the BCS or weak coupling case, Cooper pairs form and condense at the same temperature, which is  $T_c$ . In the BE or strong coupling regime,



there is another energy scale (but no phase transition), represented by the temperature  $T^*$  at which real-space bound pairs appear (they are thermally dissociated above  $T^*$ ), well separated from  $T_c$ , at which the Bose condensation takes effect.

Concerning the normal state just above  $T_c$ , the question remains: how does the system evolve, as a function of coupling strength, from a Fermi liquid with well-defined quasiparticle excitations in the weak coupling limit, to a Bose liquid of tightly bound pairs at the strong coupling end? Thus the nature of the normal state in the intermediate coupling regime is a long standing puzzle that remains to be solved. It is natural to assume that the pairing tendency of the system, while not strong enough to lead to well-defined pairs, has significant influences on the normal state properties.

Since the motivation for our work is understanding the unusual normal state of the HTSC, particularly the pseudogap state, we find it natural to start our study above  $T_c$ . We adopt the point of view that the pseudogap is a precursor effect to superconductivity, and that the pairing correlations may be responsible for this anomalous behavior in the normal state. Thus we will look at schemes that allow for the inclusion of pairing fluctuations above the phase transition and study the effect they have on the spectral properties of the system. When the system is cooled down, we expect the superconducting transition to be signaled by the divergence of the pair propagator, as correlations grow stronger and the interacting particles become unstable to pair formation.

With this in mind, we wish to find ways to systematically include correlation effects in the proper self-energy, in particular two-particle correlations. Following Ref. [65], we will show how the Equation Of Motion (EOM) method can be used to accomplish that. Within this framework we will derive a Dyson's equation for the scattering T-matrix and discuss the limitations of the Kadanoff-Martin prescription. We will not limit ourselves to the particular scheme derived in Ref. [65], but will discuss the restrictions on any generalization based, on the one hand, on whether or not the resulting scheme obeys certain conservation laws, as shown by Baym and Kadanoff in [66], and on the other hand, on whether or not it results in expected physics.

We must emphasize that a description of high- $T_c$  superconductivity in its full complexity goes beyond the scope of this work. For a complete description one must have a microscopic theory that, among other things, gives the correct symmetry of the order parameter and takes into account magnetic correlations, bound to be important given that the cuprate superconductors

are doped AF insulators. Nevertheless, we believe that the features that we do capture within the formalism we are about to describe are relevant to the high- $T_c$  systems independently of microscopic details.

## 2.3 Derivation of the self-energy in the T-matrix approximation

### 2.3.1 Definitions and notations

Throughout this work we will use a shorthand notation where a single numerical index ( $m$ ) denotes the pair of space-imaginary time coordinates  $(j_m, \tau_m)$ . In the Heisenberg picture, the creation and annihilation operators are:

$$\begin{aligned} c_\alpha(m) &= e^{-\hat{K}\tau_m} c_{j_m\alpha} e^{\hat{K}\tau_m} \quad (\text{annihilation operator}) \\ c_\alpha^\dagger(m) &= e^{-\hat{K}\tau_m} c_{j_m\alpha}^\dagger e^{\hat{K}\tau_m} \quad (\text{creation operator}) \end{aligned} \quad (2.1)$$

Here,  $\hat{K} = \hat{H} - \mu\hat{N}$  is the grand canonical Hamiltonian, where  $\hat{H}$  is the AHM Hamiltonian given by Eq. (1.1),  $\mu$  is the chemical potential and  $\hat{N}$  is the number operator. While real physical systems have a fixed number of particles and it would appear that the canonical ensemble should be used, for systems with very large numbers of particles the deviation, of the order  $(\sqrt{N})^{-1}$ , is not significant. Moreover, in the thermodynamic limit  $N \rightarrow \infty$  the results are necessarily independent of system size. Although in the grand canonical ensemble  $N$  is allowed to fluctuate, for all practical purposes  $\mu$  is chosen to maintain a fixed density  $n(T, \mu)$ .

The one-, two- and three-particle Green functions (and the Green function of any arbitrary number of particles) are defined as ensemble averages of time ordered products of Heisenberg annihilation and creation operators.

$$G_\alpha(1; 1') = -\langle T_\tau [c_\alpha(1) c_\alpha^\dagger(1')] \rangle, \quad (2.2)$$

$$G_{2,\alpha\beta}(12; 1'2') = (-1)^2 \langle T_\tau [c_\alpha(1) c_\beta(2) c_\beta^\dagger(2') c_\alpha^\dagger(1')] \rangle, \quad (2.3)$$

$$G_{3,\alpha\beta\gamma}(123; 1'2'3') = (-1)^3 \langle T_\tau [c_\alpha(1) c_\beta(2) c_\gamma(3) c_\gamma^\dagger(3') c_\beta^\dagger(2') c_\alpha^\dagger(1')] \rangle. \quad (2.4)$$

Note that, since the AHM does not contain any spin flipping mechanism, the Green function we have defined are diagonal in the spin indices.

The utility of these functions comes from the fact that any response function can be constructed from a Green function, evaluated in the appropriate limit. For example, the electron density is given by the following single-particle Green function:

$$n = G_{\uparrow}(1; 1^+) + G_{\downarrow}(1; 1^+) \equiv 2G(1; 1^+). \quad (2.5)$$

Also, one particularly important instance of the two-particle Green function is the *pair* propagator,  $G_{2,\uparrow\downarrow}(11; 1'1')$ . It is a divergence in this quantity that signals the superconducting instability. The double-occupancy is obtained from the pair propagator evaluated in the following limit:

$$\langle n_{\uparrow}n_{\downarrow} \rangle = G_{2,\uparrow\downarrow}(11; 1^+1^+). \quad (2.6)$$

In the above, by  $(m^+)$  we understand  $(j_m, \tau_m + 0^+)$ , simply saying that the time ordering operator  $T_{\tau}$  acting on a product of two operators  $c(m)$  and  $c(m^+)$  will place  $c(m^+)$  to the left of  $c(m)$  (producing a minus sign any time a permutation of two such operators is necessary).

### 2.3.2 The equation of motion (EOM) method

This method starts with the equation of motion for the Heisenberg operators:

$$-\frac{\partial}{\partial \tau_m} c_{\alpha}(m) = [c_{\alpha}(m), \hat{K}]. \quad (2.7)$$

Eq. (2.7), together with (2.2), (2.3) and the anti-commutation relations  $\{c_{j_m\alpha}, c_{j_n\beta}^{\dagger}\} = \delta_{\alpha\beta}\delta_{j_mj_n}$ , leads to the following equation of motion for the one-particle Green function:

$$\begin{aligned} \left(-\frac{\partial}{\partial \tau_1} + \mu\right) G_{\uparrow}(j_1\tau_1; j_1'\tau_1') + t \sum_{j''}^{\prime} G_{\uparrow}(j''\tau_1; j_1'\tau_1') \\ = \delta_{j_1j_1'}\delta(\tau_1 - \tau_1') - |U|G_{2,\uparrow\downarrow}(j_1\tau_1, j_1\tau_1; j_1'\tau_1', j_1\tau_1^+). \end{aligned} \quad (2.8)$$

In the above equation the prime symbol indicates that the sum is restricted to nearest neighbors of  $j_1$  only. Following Ref. [65], we define an operator  $G_{\alpha}^0(1; 1')$  such that

$$\sum_{j''}^{\prime} \left[ t + \left(-\frac{\partial}{\partial \tau_1} + \mu\right) \delta_{j_1j''} \right] G_{\alpha}^0(j''\tau_1; j_1'\tau_1') \equiv [G^0(1)]^{-1} G_{\alpha}^0(1, 1') = \delta(1, 1'). \quad (2.9)$$

As the nomenclature suggests,  $G_\alpha^0(1; 1')$  is the noninteracting ( $|U| = 0$ ) one-particle Green function. With this definition, Eq. (2.8) becomes

$$[G^0(1)]^{-1}G_\uparrow(1, 1') = \delta(1, 1') - |U|G_{2,\uparrow\downarrow}(11; 1'1^+). \quad (2.10)$$

We have used the condensed form  $\delta(1, 1') = \delta_{j_1 j_1'} \delta(\tau_1 - \tau_1')$  in the above expressions (and may use it elsewhere on occasion).

The right-hand side of Eq. (2.10) contains a two-particle Green function. Application of an imaginary time derivative to the two-particle Green function requires the three-particle Green function, and so on. Only in some very fortunate circumstances does the hierarchy of equations close, and we will see an example in the atomic limit ( $t \rightarrow 0$ ) of the AHM in the next chapter. In most cases, however, we must force a truncation of this hierarchy at some point, and this constitutes an approximation.

Truncation by decoupling the two-particle Green function in Eq. (2.10) merely results in the Hartree approximation (the direct term of the Hartree-Fock approximation, which we briefly touched upon in §2.1, opening this chapter; there is no exchange term for the AHM). This is a mean-field approximation, designed to renormalize single-particle properties. Nonetheless, we do anticipate that a decoupling is necessary, so we define the two-particle correlation function:

$$C_{2,\uparrow\downarrow}(12; 1'2') \equiv G_{2,\uparrow\downarrow}(12; 1'2') - G_\uparrow(1; 1')G_\downarrow(2; 2'). \quad (2.11)$$

With this definition, Eq. (2.10) becomes

$$\left([G^0(1)]^{-1} + |U|G_\downarrow(1; 1^+)\right)G_\uparrow(1, 1') = \delta(1, 1') - |U|C_{2,\uparrow\downarrow}(11; 1'1^+). \quad (2.12)$$

We introduce the operator

$$[\tilde{G}_\uparrow^0(1)]^{-1} \equiv [G^0(1)]^{-1} + |U|G_\downarrow(1; 1^+) = [G^0(1)]^{-1} + |U|n/2, \quad (2.13)$$

where Eq. (2.5) and the spin symmetry of the AHM was used to obtain the last equality. The noninteracting inverse operator includes now a Hartree term, expressed diagrammatically by the first term in Fig. 2.1(b). This already points to the necessity of self-consistent solutions. Analogously to Eq. (2.9), we can define the function  $\tilde{G}_\alpha^0(1; 1')$  such that

$$[\tilde{G}_\alpha^0(1)]^{-1}\tilde{G}_\alpha^0(1, 1') = \delta(1, 1'). \quad (2.14)$$

Rewriting Eq. (2.12) gives

$$[\tilde{G}_\uparrow^0(1)]^{-1} [G_\uparrow(1, 1') - \tilde{G}_\uparrow^0(1, 1')] = -|U|C_{2,\uparrow\downarrow}(11; 1'1^+). \quad (2.15)$$

The solutions to this equation can be written in integral form:

$$G_\uparrow(1, 1') = \tilde{G}_\uparrow^0(1, 1') - |U|\tilde{G}_\uparrow^0(1, \mathbf{m})C_{2,\uparrow\downarrow}(\mathbf{m}\mathbf{m}; 1'\mathbf{m}^+), \quad (2.16)$$

where the contracted variable means integrating over the internal space-imaginary time coordinates:

$$(\mathbf{m}) \equiv \sum_{j_m} \int_0^\beta d\tau_m.$$

For further reference, we cast Eq. (2.16) into a Dyson's equation form, diagrammatically shown in Fig. 2.1(a):

$$G_\uparrow(1, 1') = \tilde{G}_\uparrow^0(1, 1') + \tilde{G}_\uparrow^0(1, \mathbf{m})\tilde{\Sigma}_\uparrow(\mathbf{m}; \mathbf{n})G_\uparrow(\mathbf{n}, 1') \quad (2.17)$$

The comparison suggests a relation between the self-energy and the two-particle correlation function. We make the remark that the self-energy to be defined below contains only those proper self-energy corrections beyond first order in  $|U|$ , which have already been included in the 'noninteracting' function  $\tilde{G}^0$ :

$$\tilde{\Sigma}_\uparrow(1; \mathbf{n})G_\uparrow(\mathbf{n}, 1') = -|U|C_{2,\uparrow\downarrow}(11; 1'1^+) \quad (2.18)$$

We go back to the two-particle correlation function defined in Eq. (2.11). Applying an imaginary time derivative to this function generates a three-particle Green function:

$$[G^0(1)]^{-1}C_{2,\uparrow\downarrow}(12; 1'2') = -|U| [G_{3,\uparrow\downarrow}(121; 1'2'1^+) - C_{2,\uparrow\downarrow}(11; 1'1^+)G_\downarrow(2; 2') - G_\uparrow(1; 1')G_\downarrow(1; 1^+)G_\downarrow(2; 2')] \quad (2.19)$$

Similarly to Eq. (2.11), we can define a three-particle correlation function:

$$\begin{aligned}
C_{3,\uparrow\downarrow}(121; 1'2'1^+) &= G_{3,\uparrow\downarrow}(121; 1'2'1^+) - G_{\uparrow}(1; 1')G_{\downarrow}(2; 2')G_{\downarrow}(1; 1^+) \\
&\quad + G_{\uparrow}(1; 1')G_{\downarrow}(2; 1^+)G_{\downarrow}(1; 2') - G_{\uparrow}(1; 1')C_{2,\downarrow}(21; 2'1^+) \\
&\quad - G_{\downarrow}(2; 2')C_{2,\uparrow}(11; 1'1^+) + G_{\downarrow}(1; 2')C_{2,\uparrow}(12; 1'1^+) \\
&\quad + G_{\downarrow}(2; 1^+)C_{2,\uparrow}(11; 1'2') - G_{\downarrow}(1; 1^+)C_{2,\uparrow}(12; 1'2') \quad (2.20)
\end{aligned}$$

At this point we remember our goal to terminate the chain of equations generated by the EOM and we choose to neglect correlations between three (or more) particles. Accordingly, we set the left-hand side of Eq. (2.20) to zero. This way we decouple the three-particle Green function that appears in Eq. (2.19), which we replace by the remaining terms in Eq. (2.20). With the definition in Eq. (2.13), we rewrite the EOM for the two-particle correlation function of opposite spin:

$$\begin{aligned}
[\tilde{G}_{\uparrow}^0(1)]^{-1}C_{2,\uparrow}(12; 1'2') &= |U| [G_{\downarrow}(1; 2')C_{2,\uparrow}(12; 1'1^+) + G_{\downarrow}(2; 1^+)C_{2,\uparrow}(11; 1'2') \\
&\quad - G_{\uparrow}(1; 1')C_{2,\downarrow}(21; 2'1^+) + G_{\uparrow}(1; 1')G_{\downarrow}(2; 1^+)G_{\downarrow}(1; 2')] \quad (2.21)
\end{aligned}$$

One can also write an EOM for the two-particle correlation function of parallel spin (after some algebra of the same type we have employed above):

$$[\tilde{G}_{\downarrow}^0(1)]^{-1}C_{2,\downarrow}(12; 1'2') = |U| [G_{\downarrow}(1; 2')C_{2,\uparrow}(12; 1^+1') - G_{\downarrow}(1; 1')C_{2,\uparrow}(12; 1^+2')] \quad (2.22)$$

Conveniently, this function is expressed only in terms of the correlation function for antiparallel spins. Integrating Eqs. (2.21) and (2.22), and replacing the correlation function for particles of parallel spins with its solution in integral form, we can write for the  $C_{2,\uparrow}$ :

$$\begin{aligned}
C_{2,\uparrow}(12; 1'2') &= |U|\tilde{G}_{\uparrow}^0(1; \mathbf{m}) \left\{ G_{\uparrow}(\mathbf{m}; 1')G_{\downarrow}(2; \mathbf{m}^+)G_{\downarrow}(\mathbf{m}; 2') \right. \\
&\quad + G_{\downarrow}(\mathbf{m}; 2')C_{2,\uparrow}(\mathbf{m}2; 1'\mathbf{m}^+) + G_{\downarrow}(2; \mathbf{m}^+)C_{2,\uparrow}(\mathbf{m}\mathbf{m}; 1'2') \\
&\quad \left. - |U|G_{\uparrow}(\mathbf{m}; 1')\tilde{G}_{\downarrow}^0(\mathbf{m}; \mathbf{n}) \left[ G_{\downarrow}(\mathbf{n}; 2')C_{2,\uparrow}(\mathbf{n}2; \mathbf{n}^+\mathbf{m}^+) \right. \right. \\
&\quad \left. \left. - G_{\downarrow}(\mathbf{n}; \mathbf{m}^+)C_{2,\uparrow}(\mathbf{n}2; \mathbf{n}^+2') \right] \right\} \quad (2.23)
\end{aligned}$$

We have in Eq. (2.16) and (2.23) a set of coupled equations for the one-particle Green function and the two-particle correlation function that must be solved self-consistently. Alternatively, one can use Eqs. (2.17) and (2.18),

and include correlation effects in the single-particle properties via the self-energy.

We have gotten thus far by retaining only correlations between two particles. In order to make further progress we need to make additional approximations. In what follows we will specialize the above-mentioned equations to the dilute limit, where the density of either particles or holes goes to zero,  $n(2-n) \rightarrow 0$ .

### 2.3.3 The T-matrix approximation

In order to make the dilute limit more transparent, we introduce the vertex function  $\Gamma$  representing a generalized interaction between particles of opposite spin, such that

$$C_{2,\uparrow\downarrow}(12; 1'2') = \tilde{G}_{\uparrow}^0(1; \mathbf{m})G_{\downarrow}(2; \mathbf{n})\Gamma(\mathbf{m}\mathbf{n}; \mathbf{m}'\mathbf{n}')G_{\uparrow}(\mathbf{m}'; 1')G_{\downarrow}(\mathbf{n}'; 2') \quad (2.24)$$

Substituting this into Eq. (2.23) and factoring out the external Green functions leaves an integral equation for  $\Gamma$ :

$$\begin{aligned} \Gamma(12; 1'2') &= |U|\delta(1, 2)\delta(1, 1')\delta(2, 2') \\ &+ |U|\delta(1, 2)\tilde{G}_{\uparrow}^0(1, \mathbf{m})G_{\downarrow}(2; \mathbf{n})\Gamma(\mathbf{m}\mathbf{n}; 1'2') \\ &+ |U|\delta(1, 2')\tilde{G}_{\uparrow}^0(1, \mathbf{m})G_{\downarrow}(\mathbf{n}; 1^+)\Gamma(\mathbf{m}2; 1'\mathbf{n}) \\ &- |U|^2\delta(1, 1')\tilde{G}_{\downarrow}^0(1; 2')G_{\downarrow}(\mathbf{m}; 1)\tilde{G}_{\uparrow}^0(2', \mathbf{n}')G_{\uparrow}(\mathbf{n}; 2')\Gamma(\mathbf{m}\mathbf{n}; 2\mathbf{n}') \\ &+ |U|^2\delta(1, 1')\tilde{G}_{\downarrow}^0(1; \mathbf{m})G_{\downarrow}(\mathbf{m}; 1^+)\tilde{G}_{\uparrow}^0(\mathbf{m}, \mathbf{n})G_{\uparrow}(\mathbf{n}'; \mathbf{m}^+)\Gamma(2\mathbf{n}; 2'\mathbf{n}') \end{aligned} \quad (2.25)$$

The above equation is known as the Bethe-Salpeter equation, by analogy with similar equations in relativistic field theory. It is illustrated diagrammatically in Fig. 2.3. Based on the definition in Eq. (2.24), one can also write an expression for the self-energy in terms of  $\Gamma$ .

$$\tilde{\Sigma}_{\uparrow}(1; 1') = -|U|\tilde{G}_{\uparrow}^0(1; \mathbf{m})G_{\downarrow}(1; \mathbf{n})\Gamma(\mathbf{m}\mathbf{n}; 1'\mathbf{n}')G_{\downarrow}(\mathbf{n}'; 1^+) \quad (2.26)$$

Aiming to make either of the two alternate routes (see discussion at the end of the previous section, §2.3.2) to self-consistency practical, we will argue that in the low density limit the number of terms in Eq. (2.25) can be reduced. We have outlined in §2.1, following the discussion in Ref. [60], that for such systems the relative weight of particle-hole scattering events to particle-particle

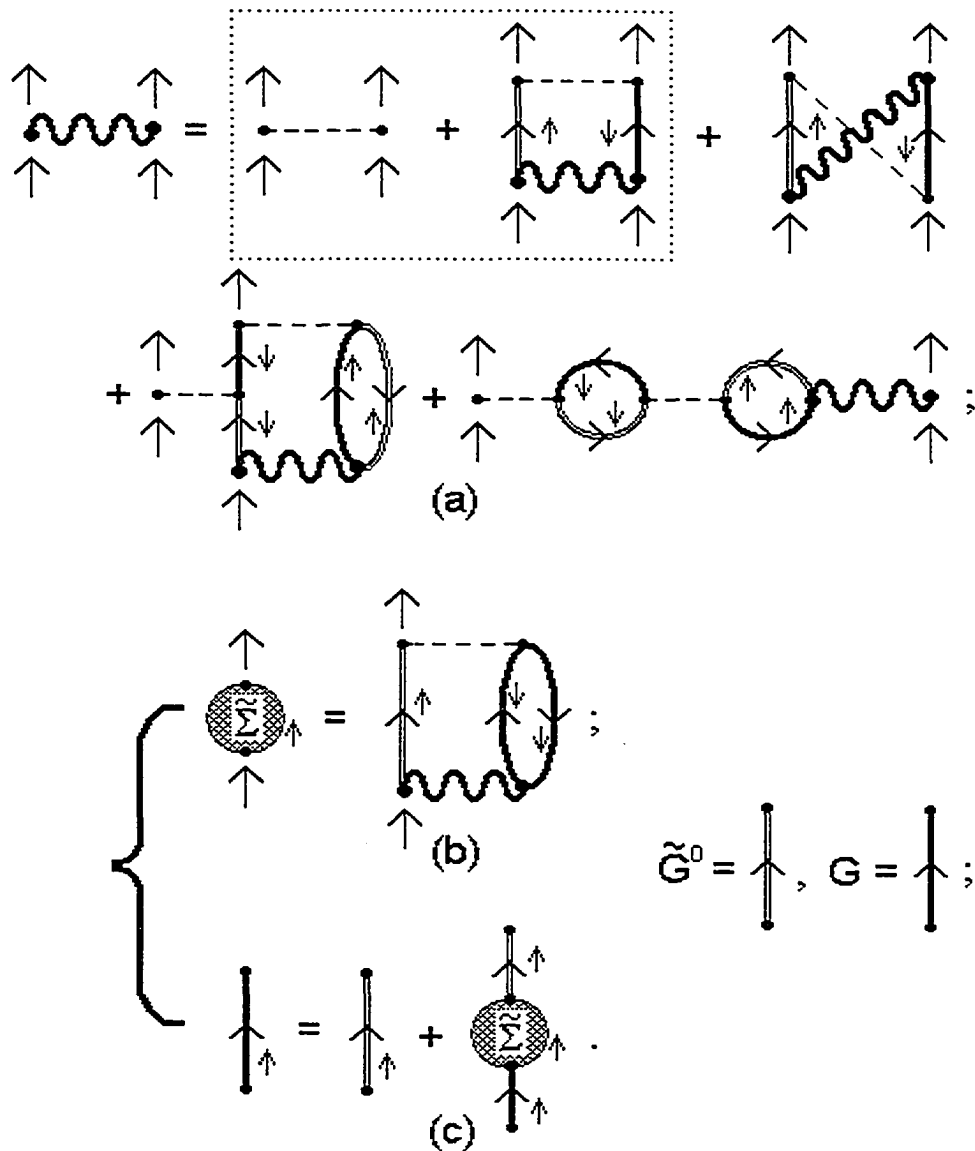


Figure 2.3: (a) Generalized interaction, as derived with EOM method for the AHM. The terms that survive in the T-matrix approximation are shown in box; (b) Proper self-energy expressed in terms of the generalized interaction; (c) Dyson's equation. Note that the equations illustrated in (b) and (c) need to be solved self-consistently. (The spin associated with each propagator is indicated by a little arrow.)



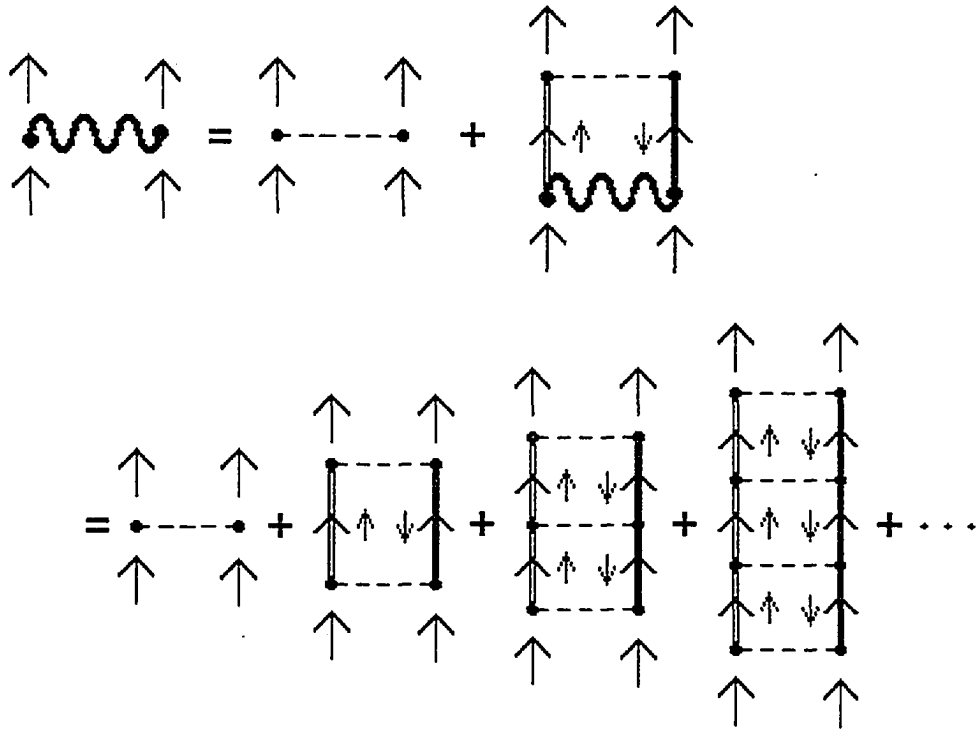


Figure 2.4: T-matrix approximation for the generalized interaction, as derived with the EOM method for the AHM (terms shown in box in Fig. 2.3(a)).

events becomes vanishingly small. Thus in the dilute limit the dominant contributions are expected to come from the first two terms in Eq. (2.25), so they are the only ones retained in the T-matrix approximation.

Referring back to §2.1 and comparing Fig. 2.2 with Fig. 2.3 and Fig. 2.4, we have demonstrated that the EOM method provides a way to decide which of the propagators appearing in the ladder diagrams are to be reinterpreted and self-consistently determined. Once again, we note that within this scheme even the ‘bare’ propagator  $\tilde{G}^0$  is not all that ‘bare’, because it contains a full Hartree term, and it is therefore very much involved in the self-consistency loop.

### 2.3.4 Fourier representation

Most of the time it is more convenient to work with momentum-frequency coordinates. For one thing, the pairing that leads to superconductivity takes place in momentum space. We will also see that discrete sums over Matsubara frequencies are more easily handled than integrals over imaginary time.

Because of the translational and imaginary time invariance of the AHM, the one-particle Green function  $G(1;1')$  depends on its coordinates only through  $1 - 1'$ . This naturally leads to the Fourier representation:

$$G_\alpha(1 - 1') = \sum_k e^{ik \cdot (1-1')} G_\alpha(k). \quad (2.27)$$

Here and elsewhere we will be using the following notations:

$$\begin{aligned} k &\equiv (\vec{k}, i\omega_m), \\ \sum_k &\equiv \frac{1}{\beta N} \sum_{\vec{k}} \sum_{m=-\infty}^{\infty}, \\ k \cdot (1 - 1') &\equiv \vec{k} \cdot (\vec{R}_{j_1} - \vec{R}_{j'_1}) - i\omega_m(\tau_1 - \tau_{1'}). \end{aligned} \quad (2.28)$$

In the above expressions,  $\vec{k}$  is the momentum associated with the injected particle described by the one-particle Green function and  $i\omega_m \equiv i\pi T(2m - 1)$ ,  $m \in \mathbb{Z}$ , is the fermionic Matsubara frequency.

The Fourier transform for the two-particle Green function involves a three-index object  $G_{2,\alpha\alpha'}(kQq)$ :

$$G_{2,\alpha\alpha'}(12; 1'2') = \sum_{kQq} e^{ik \cdot (1-2-1'+2')} e^{iQ \cdot (2-2')} e^{iq \cdot (1-2)} G_{2,\alpha\alpha'}(kQq) \quad (2.29)$$

Here, the upper case index  $Q \equiv (\bar{Q}, i\nu_n)$  indicates that its frequency component is a bosonic Matsubara frequency,  $i\nu_n \equiv i2\pi Tn$ ,  $n \in \mathbb{Z}$ . The significance of the momentum indices is as follows:  $2\vec{k}$  is the relative momentum of the particle pair,  $\bar{Q}$  is the momentum of the center of mass, and  $\vec{q}$  is the momentum transfer between the particles.

In the general case, the Fourier transform of  $\Gamma(12; 1'2')$  is a three-index object  $\Gamma(kQq)$  as well. It enters the equation for the proper self-energy in momentum-frequency coordinates, obtained from the Fourier transformation of Eq. (2.26):

$$\tilde{\Sigma}_\uparrow(k) = -|U| \sum_{Qq} \Gamma(kQq) \tilde{G}_\uparrow^0(k+q) G_\downarrow(Q-k-q) G_\downarrow(Q-k) \quad (2.30)$$

However, when only the ladder diagrams are retained, as discussed in §2.3.3 and indicated by the box in Fig. 2.3, the vertex function really is  $\Gamma(12; 1'2') \equiv \delta(1,2)\delta(1'2')\Gamma(11; 1'1')$ , and its Fourier transform loses its  $k$  and  $q$  dependence:

$$\begin{aligned} \Gamma(kQq) &\xrightarrow{\text{dilutelimit}} T(Q) = |U| + |U|\chi_0(Q)T(Q) \\ &= \frac{|U|}{1 - |U|\chi_0(Q)}. \end{aligned} \quad (2.31)$$

We have introduced in the above equation the ‘bare’ pairing susceptibility  $\chi_0(Q)$ , given by:

$$\chi_0(Q) = \sum_k \tilde{G}_\uparrow^0(k) G_\downarrow(Q-k). \quad (2.32)$$

We have mentioned before that one quantity of particular interest is the pair propagator,  $G_{2,\uparrow\downarrow}(11; 1'1')$ . Its Fourier transform depends only on  $Q$  as well, and working our way back to Eq. (2.11), making use of Eqs. (2.32), (2.31), (2.24) along the way, together with Fourier representation, we arrive at the following expression:

$$\begin{aligned} G_{2,\uparrow\downarrow}(Q) &\equiv \chi(Q) = \chi_0(Q) + [\chi_0(Q)]^2 T(Q) \\ &= \frac{1}{|U|} \chi_0(Q) T(Q) \\ &= \frac{\chi_0(Q)}{1 - |U|\chi_0(Q)}. \end{aligned} \quad (2.33)$$

One can view Eq. (2.33) as the linear response susceptibility to a fictitious ‘pairing’ field [67]. The zero in the denominator, occurring at zero frequency

and momentum, leads to a divergence in this quantity, which signals the superconducting instability [63, 68]. This is the so-called Thouless criterion:

$$1 - |U|\chi_0(\vec{0}, 0) = 0, \quad (2.34)$$

which can be used to calculate the superconducting transition temperature  $T_c$ .

Finally, within the T-matrix approximation, one derives the following expression for the self-energy:

$$\begin{aligned} \tilde{\Sigma}_\uparrow(k) &= -|U| \sum_{Q, k'} T(Q) \tilde{G}_\uparrow^0(k') G_\downarrow(Q - k') G_\downarrow(Q - k) \\ &= -|U| \sum_Q T(Q) \chi_0(Q) G_\downarrow(Q - k) \\ &= -|U|^2 \sum_Q \chi(Q) G_\downarrow(Q - k). \end{aligned} \quad (2.35)$$

Eq. (2.35) has been obtained by substituting Eqs. (2.31) and (2.33) into Eq. (2.30).

Inspecting one more time Eqs. (2.32), (2.33) and (2.35), we note that there are three one-particle Green functions entering the expression for the self-energy. The first propagator in the pair susceptibility is the ‘noninteracting’ one,  $\tilde{G}_0(k)$ . The other two represent fully interacting Green functions. Through Dyson’s equation, the self-energy defines the full one-particle Green function:

$$G(k) = [\tilde{G}_0^{-1}(k) - \tilde{\Sigma}(k)]^{-1} \quad (2.36)$$

Eq. (2.36) is the Fourier space correspondent of Eq. (2.17). Thus the Dyson’s equation closes a self-consistency loop, ensuring that single-particle properties ‘feel’ the pairing tendency of the system, while the use of the full propagator in the pair susceptibility ensures that feedback is returned to two-particle properties.

One additional note here concerns the one-particle Green function  $\tilde{G}^0(k)$ . Analogously to the derivation in Appendix A, one can write

$$\tilde{G}^0(\vec{k}, i\omega_m) = [i\omega_m - (\epsilon_{\vec{k}} - \mu') ]^{-1}. \quad (2.37)$$

The difference between this function and the truly noninteracting  $G^0$  given by Eq. (A.17) comes from the use of the modified chemical potential  $\mu'$ . As

a result of Eq. (2.13), a Hartree term has been absorbed in the chemical potential:  $\mu' = \mu + |U|n/2$ . As shown in Eq. (2.5), which we re-write below in Fourier representation:

$$\begin{aligned} n &= 2G(1; 1^+) = 2 \sum_k G(k) e^{i\omega_m 0^+} \\ &= 1 + \frac{2}{\beta N} \sum_{\vec{k}} \sum_{m=-\infty}^{\infty} \text{Re} G(\vec{k}, i\omega_m), \end{aligned} \quad (2.38)$$

this implies that the full Green function  $G(k)$  enters  $\mu'$  via  $n$ , involving  $\tilde{G}^0$  itself in the self-consistency loop, as we have already pointed out.

Before we end this section, for future reference, we also re-write the double-occupancy, given by Eq. (2.6), in Fourier space:

$$\langle n_{\uparrow} n_{\downarrow} \rangle = G_{2,\uparrow\downarrow}(11; 1^+ 1^+) = \sum_Q G_{2,\uparrow\downarrow}(Q) e^{i\nu_n 0^+}. \quad (2.39)$$

Alternatively, one can use Eqs. (2.11) and (2.18) to express double-occupancy in terms of one-particle properties:

$$\begin{aligned} \langle n_{\uparrow} n_{\downarrow} \rangle &= G_{2,\uparrow\downarrow}(11; 1^+ 1^+) \\ &= G(1; 1^+) G(1; 1^+) - \frac{1}{|U|} \tilde{\Sigma}(1; \mathbf{m}) G(\mathbf{m}; 1^+) \\ &= \frac{n^2}{4} - \frac{1}{|U|} \sum_k \tilde{\Sigma}(k) G(k). \end{aligned} \quad (2.40)$$

## 2.4 Self-consistency, BCS limit and conservation laws in the T-matrix approximation

In section §2.3, we have shown a way to formulate a self-consistent scheme that allows a controlled, systematic inclusion of correlations into single particle properties, as follows from the Kadanoff-Martin work described in [65]. Anticipating the next section, the self-consistency is needed to improve on the work started by Thouless [63] and re-addressed later on, in the context of high  $T_c$  cuprates, by Schmitt-Rink, Varma and Ruckenstein [69], by returning feedback to the two-particle properties, once the single-particle ones have been renormalized.

There are, however, problems with the Kadanoff-Martin scheme. First of all, the weak-coupling limit of this particular scheme, expected to reproduce the BCS results, leads to the presence of states in the superconducting gap. In fact, any self-consistent scheme where the full propagator is used for the third Green function in the self-energy, the one that appears explicitly in Eq. (2.35) (see the last line), proved unable to properly reproduce the BCS gap [70, 29].

In order to correct this difficulty with the Kadanoff-Martin prescription, Patton [71] argued that the Green function in question should be replaced by its noninteracting counterpart. This ‘fix’ is based on the possibility that vertex corrections, dropped in the T-matrix approximation, partially cancel some of the contributions retained in the above-described scheme. In recent times, this approach has been championed by Levin and co-workers [72] and has found some agreement with experiments on high  $T_c$  cuprates. However, the adjustment is completely *ad hoc*, and it doesn’t cure another problem with Kadanoff-Martin scheme, the problem with the number conservation. Any given diagrammatic approximation must comply with a set of conditions derived by Baym and Kadanoff in order to ensure conservation of particle number, energy and angular momentum. In particular, the asymmetric form of the independent particle susceptibility (see Eq. (2.32)) is not consistent with a number conserving approximation. This was already acknowledged by Kadanoff and Martin in Ref. [65] (see the discussion at the end of section 3).

Alternatively, Bickers and coworkers [73] extended the theory formulated earlier by Baym [74], based on functional derivatives of a free energy functional. This procedure guaranteed that the resulting approximation, so-called ‘ $\Phi$ -derivable’, would be fully conserving. Its extension to lattice electrons is known as the FLuctuation EXchange approximation (FLEX) [73]. The T-matrix version of this theory (only particle-particle channel is retained) has all three instances of the one-particle Green function in the self-energy fully self-consistent. Although such a formulation would appear to be the most accurate of the T-matrix approximations, since it contains the most number of diagrams, it takes us right back into the problem with the states in the gap, as discussed above. The partial cancellation between terms dropped in T-matrix theories and some of the contributions retained appears likely.

Based on the arguments presented above, it would seem that the only viable choice is a symmetric form of the independent particle susceptibility (this translates into both fully self-consistent Green functions in Eq. (2.32)), and replacing the third Green function in Eq. (2.35) for the self-energy with

its noninteracting counterpart. Indeed, this has been suggested [70, 75]. While this version of the T-matrix is not ‘ $\Phi$ -derivable’ in the Baym sense, it does lead to two-particle quantities that are conserving, and is able to reproduce the BCS gap.

We hope to have convinced the reader of the lively debate in the literature as to what the best self-consistent T-matrix theory might be. Any particular scheme has its advocates, with viable arguments *pro* their theory of choice and *contra* any other. Another altogether different approach was adopted by Vilk and Tremblay [29], implemented by Kyung *et al.* [76] for the AHM. They designed a technique that enforces self-consistency at the two-particle level, and determines the irreducible spin and charge vertices. This is in contrast to the T-matrix-type approaches, which attempt to get single particle properties most correctly.

In the next chapter we will examine this issue once again, in a limit where exact results are available and a direct comparison with the prediction of different schemes may help discriminate between candidate theories.

## 2.5 Non-Self-Consistent T-matrix approximation: is it enough?

We have mentioned a few times already that T-matrix-type approximations came to be used in the context of superconductivity following the original work of Thouless in 1960 [63]. In his approach, a pairing susceptibility was defined, just like in Eq. (2.33), but with both propagators ‘bare’. In the conventional framework, this pairing susceptibility diverges at  $T_c$ , as defined by the BCS theory. Thus the Thouless criterion, Eq. (2.34), constitutes an alternate means of defining the transition temperature.

In more recent times (1980), a revival of pair fluctuations ideas was initiated by Leggett in Ref. [23]. His work was extended five years later by Nozières and Schmitt-Rink [64], who developed a diagrammatic scheme designed to include the effect of pairing fluctuations above  $T_c$  at the lowest order.

The unusual properties of High  $T_c$  superconductors motivated Schmitt-Rink, Varma and Ruckenstein (SVR) [69] to extend the scheme developed by Nozières and Schmitt-Rink [64] to two dimensions (2D). One important technical point clarified in [64] was that the equation for the superconducting

gap and the number equation had to be solved together. For two-dimensional systems, the Thouless criterion leads to a finite value of  $T_c$  if the chemical potential is held constant. Any finite temperature phase transition in two (or lower) dimensions is prohibited by the Mermin-Wagner theorem [77]. When the number equation is also considered, SVR concluded that, for a given electron density, as the temperature is lowered, the chemical potential would self-consistently adjust to avoid the Thouless instability. In fact, any value of the electron density would result in a situation at  $T = 0$  in which the Fermi surface no longer existed; the electrons are paired in Bose-like bound states, and the chemical potential is simply half of the single pair bound state energy. This result violates Luttinger's theorem [53], which states that the volume of the Fermi sea should be conserved. We warn the reader that this situation is different than the BCS-BE crossover scenario, where varying the coupling strength the two limits could both be reached; instead, here the depletion of the Fermi surface happens for a fixed strength of the interaction, when the temperature is lowered toward zero.

Improvements to the the SVR prescription due to Serene [78] and, a few years later, Tokumitsu *et al.* [79], were motivated by an attempt to correct this unphysical behavior found by Schmitt-Rink *et al.* in 2D. However, despite claims by Serene [78] that including repeated scattering of an electron by independent pair fluctuations restored the robust character of the Fermi liquid behavior, such claims were proved unfounded, at least for lattice fermions [75]. In fact, including multiple scattering in the number equation do make the results for lattice fermions more physical, for example the electron density goes to one on the curve that signals the Thouless instability in the  $T - \mu$  plane (Thouless curve), instead of being a diverging quantity. Again, the importance of simultaneous solutions for the superconducting transition and for the number equation must be emphasized. But the physics of Ref. [69] survives such an improvement.

The work of Serene made it clear that the SVR treatment amounted to the Non-Self-Consistent (NSC) T-matrix approximation. This corresponds to a pair susceptibility and a self-energy with only noninteracting one-particle Green functions in Eq. (2.32) and Eq. (2.35), respectively. Such a formulation has the appeal that further progress can be made analytically. Since the noninteracting propagators have known analytical form, shown in Eq. (2.37), the frequency summations in the non-self-consistent versions of Eq. (2.32) and Eq. (2.35) can be readily performed. Moreover, referring back to section §2.4, with Serene's improvement the approximation is conserving, 'Φ-derivable' in



the Baym sense. But it leads to certain pathologies for lower dimensionality. The fact that such a treatment violates Luttinger's theorem immediately suggests that renormalization of the single-particle propagators is important.

The impact of self-consistency on the SVR results of Ref. [69] is related to the more general question of feedback effects on the Thouless criterion. The existence of a diverging pairing susceptibility as the system is cooled towards the superconducting instability should affect the single-particle properties, so the electrons should 'know' about the pairing tendency of the system, and 'adjust' to it. Thus, self-consistent treatment is required. Indeed, it has been shown that any degree of self-consistency in the T-matrix is sufficient to drive the Thouless instability to zero temperature [72, 75]. Whether or not the self-consistent solution corresponds to a superconducting phase depends on the particular self-consistent scheme employed to calculate the self-energy.

With this discussion, we end the current chapter dedicated to formulating approximate diagrammatic techniques and move next to discuss results in the atomic limit.

# Chapter 3

## Atomic Limit

We have shown in Chapter 2 that self-consistency can be enforced in the T-matrix in many ways. Deciding what configuration of bare and dressed propagators is most successful depends on which physical properties of the model one wants to reproduce.

This chapter is motivated by the fact that in the atomic limit an exact solution is readily available. This enables us to discriminate between different approximate theories. For the AHM the atomic limit represents the strong coupling limit, where the on-site coupling is very strong and the hopping becomes insignificant, leaving the different sites uncorrelated (0-dimensional limit). We intend to use the analysis presented here as a guide for suitable approximations in higher dimensions. We will also consider the Two-Particle Self-Consistent (TPSC) approach developed by Vilk and Tremblay [29] and implemented for the AHM by Kyung et al. [76].

### 3.1 Exact Results

We will formulate the problem in a manner that avoids Hartree diagrams, thus reducing the number of possible self-consistent versions one has to consider [80]. The Hamiltonian is given by:

$$\hat{H} = -t \sum_{\langle ij \rangle, \sigma} (\hat{c}_{i\sigma}^\dagger \hat{c}_{j\sigma} + h.c.) - \mu' \sum_{i, \sigma} \hat{n}_{i\sigma} - |U| \sum_i (\hat{n}_{i\uparrow} - n/2)(\hat{n}_{i\downarrow} - n/2), \quad (3.1)$$

where the sum in the first term (the hopping term) is restricted, as usual, to the nearest neighbors only. The mean field expectation value  $\langle \hat{n}_{i\sigma} \rangle =$

$n_\sigma = n/2$  is subtracted from the electron density operator in the interaction term and the modified chemical potential  $\mu'$  is given in terms of the actual chemical by the relation  $\mu' = \mu + |U|n/2$ . The use of  $\mu'$  instead of  $\mu$  insures that all Hartree diagrams have been included automatically.

In the atomic limit (*i.e.*, the zero- $t$  limit, where the problem reduces to a single site problem), one can proceed with the equation of motion method outlined in §2.3.2 and find that the hierarchy of equations will decouple at the two-particle level. This allows us to obtain the one- and two-particle propagators in closed form. For the one-particle propagator we find:

$$G_\uparrow(z) = \frac{1 - n_\downarrow}{z + \mu' - |U|n_\downarrow} + \frac{n_\downarrow}{z + \mu' + |U|(1 - n_\downarrow)}, \quad (3.2)$$

and therefore, with the noninteracting limit,  $G_0(z) = 1/(z + \mu')$  as a reference state,

$$\Sigma_\uparrow(z) = \frac{|U|^2 n_\downarrow (1 - n_\downarrow)}{z + \mu' + |U|(1 - 2n_\downarrow)}. \quad (3.3)$$

Notably, the exact solution has a simple structure, with two poles, analogous to a lower and upper Hubbard band in the repulsive model, with energies separated by  $|U|$ .

The electron density is easily obtained in terms of the modified chemical potential  $\mu'$ , from Eq. (2.38) specialized to the atomic limit:

$$\begin{aligned} n &= \frac{2}{\beta} \sum_{i\omega_m} G(i\omega_m) e^{i\omega_m 0^+} \\ &= \frac{2f(-\mu' + |U|n/2)}{1 + f(-\mu' + |U|n/2) - f(-\mu' - |U|(1 - n/2))}. \end{aligned} \quad (3.4)$$

Inverting this relation, one obtains for the chemical potential:

$$\mu' = -\frac{|U|}{2}(1 - n) - T \ln(a(n)/n). \quad (3.5)$$

Here the zero temperature result is given in the first term, while the second term gives the finite temperature corrections, with:

$$a(n) = (1 - n) \exp(-\beta|U|/2) + \sqrt{n(2 - n) + (1 - n)^2 \exp(-\beta|U|)}.$$

The pair propagator:

$$G_{2,\uparrow\downarrow}(z) \equiv \chi(z) = \frac{1 - n}{z + 2\mu' + |U|(1 - n)} \quad (3.6)$$

leads to the following expression for double-occupancy:

$$\begin{aligned}\langle n_{\uparrow}n_{\downarrow} \rangle &= \frac{1}{\beta} \sum_{i\nu_l} G_{2,\uparrow\downarrow}(i\nu_l) e^{i\nu_l 0^+} \\ &= (1-n)N(-2\mu' - |U|(1-n)),\end{aligned}\quad (3.7)$$

where  $N(x) \equiv 1/(e^{\beta x} - 1)$  is the Bose function. With the result of Eq. (3.5) this ‘simplifies’ to

$$\langle n_{\uparrow}n_{\downarrow} \rangle = \frac{n^2}{2} \frac{1}{n + a(n) \exp(-\beta|U|/2)}.\quad (3.8)$$

As  $T \rightarrow 0$  the result is quite simple and expected,  $\langle n_{\uparrow}n_{\downarrow} \rangle \rightarrow n/2$ .

## 3.2 T-Matrix Approximation

### 3.2.1 NSC T-matrix

The NSC T-Matrix approximation corresponds to the all-bare configuration of propagators in Eq. (2.35). In this formulation of the problem, while pairing effects are included in the one-particle self-energy, no feedback is returned to the T-matrix. This leads to certain pathologies when the available phase space is small, and we will see this exemplified in the atomic limit. However, we believe that it provides some insight into how pairing fluctuations modify the structure of single-particle properties. Moreover, this approach becomes increasingly more reliable as the temperature is increased and feedback effects are less important.

The NSC result for the pair propagator is obtained from Eq. (2.31) when both Green functions in the pair susceptibility, Eq. (2.33), are the ‘bare’, noninteracting ones:

$$G_{2,\uparrow\downarrow}^{NSC}(z) \equiv \chi^{NSC}(z) = \frac{1 - n_0}{z + 2\mu' + |U|(1 - n_0)},\quad (3.9)$$

where  $n_0 = \frac{2}{\beta} \sum_{i\omega_m} G_0(i\omega_m) e^{i\omega_m 0^+} = 2f(-\mu')$  is the noninteracting value for the electron density and  $f(x) \equiv 1/(e^{\beta x} + 1)$  is the Fermi function. Substituting this pair propagator into Eq. (2.35) leads to the following self-energy:

$$\Sigma^{NSC}(z) = \frac{a}{z + \mu' + b}.\quad (3.10)$$

The one-particle propagator is then given by the Dyson's equation, Eq. (2.36), and has the following form:

$$G^{NSC}(z) = \frac{c_1}{z + \mu' - z_1} + \frac{c_2}{z + \mu' - z_2}. \quad (3.11)$$

In Eqs. (3.10) and (3.11) we have used the following notations:

$$\begin{aligned} z_{1,2} &= -\frac{b}{2} \pm \sqrt{\left(\frac{b}{2}\right)^2 + a}, \\ c_{1,2} &= \left[ \pm \frac{b}{2} + \sqrt{\left(\frac{b}{2}\right)^2 + a} \right] / \left[ 2\sqrt{\left(\frac{b}{2}\right)^2 + a} \right], \\ b &= |U|(1 - n_0) \text{ and} \\ a &= |U|^2 \left[ \langle n_\uparrow n_\downarrow \rangle^{NSC} + \frac{n_0}{2}(1 - n_0) \right]. \end{aligned} \quad (3.12)$$

Analogously to Eq. (3.7), the double occupancy is given by

$$\langle n_\uparrow n_\downarrow \rangle^{NSC} = (1 - n_0)N(-2\mu' - |U|(1 - n_0)). \quad (3.13)$$

The Green function in Eq. (3.11) provides  $n$  via Eq. (2.38), but this  $n$  does *not* replace  $n_0$  in Eq. (3.9), so there is no feedback on  $\chi$ . The divergence of the pair propagator, occurring at zero energy and zero momentum, signals the superconducting instability. For the NSC T-matrix approximation, the zero of the denominator in Eq. (3.9) leads to a non-zero solution for  $T_c$ :

$$T_c = \frac{\mu'}{\ln \left[ \left( \frac{|U|}{2} + \mu' \right) / \left( \frac{|U|}{2} - \mu' \right) \right]} \quad (3.14)$$

This defines the 'Thouless curve' in the  $\mu' - T$  plane, and this is where an instability would occur when the temperature is lowered and  $\mu'$  is held fixed. The Thouless curve delimits a region where no solutions exist for  $\mu'$ . The divergence of the pair propagator leads to a divergence in the self-energy, and as a result the number density goes to one on the Thouless curve, as made evident by the second line in Eq. (2.38). At the two-particle level, it naturally leads to a diverging double-occupancy, which is clearly unphysical. Indeed, Fig. 3.1(b) shows that when the electron density is kept fixed (a more

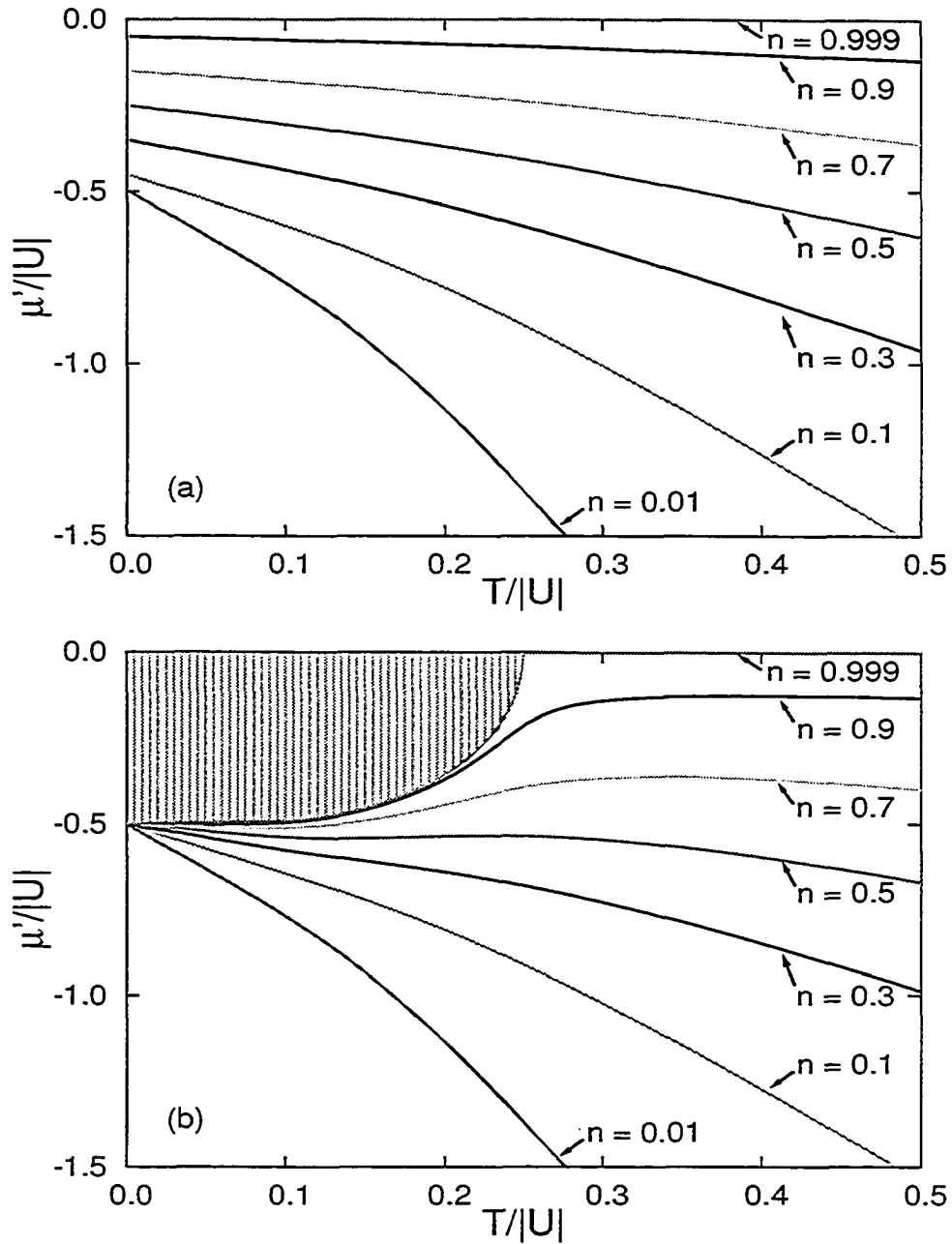


Figure 3.1: (a) Exact solutions (Eq. (3.5)) and (b)  $(G_0G_0)G_0$  (NSC) results for  $\mu'$  vs. temperature for different densities. In (b) the shaded region is the so-called Thouless region (see Eq. (3.14)). Note that it is absent in the exact solution.

physical procedure),  $\mu'$  adjusts so that a finite temperature phase transition is avoided (in accordance with the Mermin-Wagner theorem). As in higher dimensions (see the discussion in §2.5), the electrons form bound states, the Fermi sea is depleted and a finite temperature transition is avoided *for the wrong reason*, as the comparison with the exact results shown in Fig. 3.1(a) demonstrates.

### 3.2.2 Enforcing self-consistency

We have seen that the NSC T-matrix is poor. Now, we address the question of enforcing self-consistency.

Work done in higher dimensions [72, 75], shows that indeed, self-consistency can correct the unphysical features of the NSC T-matrix related to the superconducting instability. The root of the problem comes from neglecting the importance of feedback effects on the Thouless criterion. That is, the single-particle propagators should ‘know’ about the pairing tendency of the system as the temperature is lowered and ‘respond’ accordingly, and that will influence that pairing tendency.

The difficulty lies in deciding: how? We have mentioned in §2.4 the lengthy debate in the literature regarding the ‘proper’ way to include feedback in the T-matrix theory. Since the outcome of a self-consistent calculation can differ dramatically when different schemes are employed, one must proceed with caution. The fact that several theoretical approaches may be used to rigorously derive different self-consistent schemes, some of which fail to reproduce expected physics, only adds to the confusion.

Given the above considerations, we have decided to examine all the possible self-consistent schemes in the atomic limit and compare their predictions with the exact results. In this limit, with the particular form of the Hamiltonian given in Eq. (3.1), the self-energy in Eq. (2.35) becomes:

$$\Sigma(i\omega_m) = -|U|^2 \frac{1}{\beta} \sum_n \frac{\chi_0(i\nu_n)}{1 - |U|\chi_0(i\nu_n)} G_c(-i\omega_m + i\nu_n). \quad (3.15)$$

The ‘bare’ susceptibility  $\chi_0(i\nu_n)$  is given by (rewriting Eq. (2.32) in the atomic limit):

$$\chi_0(i\nu_n) = \frac{1}{\beta} \sum_m G_a(i\omega_m) G_b(-i\omega_m + i\nu_n), \quad (3.16)$$

where the subscripts  $a$ ,  $b$ , and  $c$  in the above two equations can either be absent (to indicate that the fully interacting Green function should be used) or can be set to ‘0’, to indicate that the noninteracting Green function is used. When all the subscripts are ‘0’ one has the NSC case discussed in the previous section. If any of the Green functions occurring in Eqs. (3.15), (3.16) is the fully interacting one,  $G$  and  $\Sigma$  must be determined self-consistently using Dyson’s equation, Eq. (2.36).

### 3.3 TPSC Approach

The TPSC approach is fully documented for the Hubbard model in Ref. [29], and for the attractive Hubbard model in Ref. [76]. We summarize below the main results, specialized to the AHM, as given by Eq. (3.1), in the atomic limit.

These authors utilize an ansatz for the particle-particle irreducible vertex. In the case of the AHM it is:

$$|U_{pp}| = |U| \frac{\langle (1 - n_{\uparrow})n_{\downarrow} \rangle}{\langle 1 - n_{\uparrow} \rangle \langle n_{\downarrow} \rangle}, \quad (3.17)$$

where  $n_{\sigma}$  is the particle density operator for spin  $\sigma$ , and the angular brackets denote expectation values. Based on a series of conservation laws and sum rules, the self-energy at the first level of the approximation is derived:

$$\tilde{\Sigma}^{(1)} = (|U_{pp}| - |U|)(1 - n)/2, \quad (3.18)$$

This expression for the self-energy differs from the original one derived in [76] by a Hartree term. The quantity of interest is  $\mu'$ . This enters the single-particle Green function in the combination  $\mu'^{(1)} - \tilde{\Sigma}^{(1)}$ :

$$G^{(1)}(z) = \left[ z + \mu'^{(1)} - \tilde{\Sigma}^{(1)} \right]^{-1}, \quad (3.19)$$

which should be the same as  $\mu^{(1)} - \Sigma^{(1)}$  derived in the original formalism (the upper index indicates the level of the approximation). Since the contribution from the Hartree diagrams is included in  $\mu'$ , we subtracted it off the self-energy. This is related to the use of the special form of the Hamiltonian in Eq. (3.1).

As one can see in Eq. (3.17), the double occupancy is needed in order to obtain the irreducible vertex. This can be determined self-consistently from



Eq. (2.39), where the two-particle susceptibility is given by an expression similar to Eq. (2.33), with one important difference, the ‘bare’ interaction  $|U|$  is replaced by the irreducible vertex  $|U_{pp}|$ . The resulting self-consistent equation for  $\langle n_{\uparrow}n_{\downarrow} \rangle$  is:

$$\frac{1}{\beta} \sum_l \frac{\chi_0^{(1)}(i\nu_l)}{1 - |U_{pp}| \chi_0^{(1)}(i\nu_l)} e^{i\nu_l 0^+} = \langle n_{\uparrow}n_{\downarrow} \rangle, \quad (3.20)$$

Here, the ‘bare’ pair susceptibility  $\chi_0^{(1)}(i\nu_l)$  is given by Eq. (3.16), but with both one-particle Green functions evaluated at the first level of the approximation, Eq. (3.19).

Eqs. (3.17) - (3.20), together with the number equation, Eq. (2.38), form a system of coupled equations, from which the double-occupancy  $\langle n_{\uparrow}n_{\downarrow} \rangle$ , the irreducible vertex  $U_{pp}$  and the chemical potential,  $\mu'$ , can be determined for fixed electron density.

A second level of approximation can be implemented within the TPSC approach, where an exact expression for the single electron self-energy [29] is used; the (unknown) functions required are obtained from the first step described above. The resulting self-energy resembles that obtained from a Migdal-like approach (where vertex corrections are neglected, as is the case with T-matrix theories); a very important difference is that one of the vertices is fully dressed:

$$\tilde{\Sigma}^{(2)}(i\omega_m) = -|U| |U_{pp}| \frac{1}{\beta} \sum_n \frac{\chi_0^{(1)}(i\nu_n)}{1 - |U_{pp}| \chi_0^{(1)}(i\nu_n)} G^{(1)}(-i\omega_m + i\nu_n). \quad (3.21)$$

Again, note that the Hartree term has been subtracted, for the same reasons as explained above. By computing the self-energy at this second level, the next level of approximation can be obtained. In the atomic limit, we can proceed analytically to get

$$\tilde{\Sigma}^{(2)}(z) = \frac{a}{z + \mu'^{(2)} + b} \quad (3.22)$$

for the self-energy, and

$$G^{(2)}(z) = \frac{c_1}{z + \mu'^{(2)} - z_1} + \frac{c_2}{z + \mu'^{(2)} - z_2} \quad (3.23)$$

for the one-particle Green function. This Green function is then substituted in the number equation, Eq. (2.38), which can be inverted to provide  $\mu'$  for fixed  $n$ . In Eqs. (3.22) and (3.23) we have used the following notations:

$$\begin{aligned}
z_{1,2} &= -\frac{b}{2} \pm \sqrt{\left(\frac{b}{2}\right)^2 + a}, \\
c_{1,2} &= \left[ \pm \frac{b}{2} + \sqrt{\left(\frac{b}{2}\right)^2 + a} \right] / \left[ 2\sqrt{\left(\frac{b}{2}\right)^2 + a} \right], \\
b &= |U_{pp}|(1-n) + \frac{1}{\beta} \ln \left( \frac{n}{2-n} \right) - \mu'^{(2)} \quad \text{and} \\
a &= |U||U_{pp}| \left[ \langle n_{\uparrow} n_{\downarrow} \rangle + \frac{n}{2}(1-n) \right].
\end{aligned} \tag{3.24}$$

## 3.4 Comparison of results

### 3.4.1 Chemical potential

We have examined all the possible variations for Eqs. (3.15), (3.16) at low electron densities. The results for  $\mu'$  vs.  $T$  at a low electron density,  $n = 0.3$ , are shown in Fig. 3.2(a). In addition we have also computed the result for the Vilk-Tremblay [76] TPSC theory. At very low electron densities all approximations work reasonably well. At low (but not too low) electron densities, two emerge as particularly accurate, the  $(GG_0)G_0$  T-matrix theory, and the Vilk-Tremblay theory. We use a nomenclature for the T-matrix theory to correspond to  $(G_a G_b)G_c$ , where the  $a$ ,  $b$ , and  $c$  refer to the labels in Eqs. (3.15), (3.16). Focussing on the low temperature regime, two approximations emerge as most accurate: the Vilk-Tremblay TPSC result and the  $(GG_0)G_0$  T-matrix approximation. For  $n = 0.3$  the TPSC result is more accurate over an extended temperature range; in fact, at still lower densities ( $n = 0.1$  shown in Fig. 3.3) the  $(GG_0)G_0$  result becomes more accurate than the TPSC result, and these two remain the front-runners for all electron densities. Interestingly, both the TPSC and the  $(GG_0)G_0$  results appear to become exact at low temperatures.

Indeed, we will use an ansatz appropriate for the zero temperature limit to confirm this analytically. In the  $(GG_0)G_0$  formulation the ansatz

$$\Sigma(i\omega_m) = \frac{\Delta^2}{i\omega_m - \mu'} \quad (3.25)$$

emerges if one considers only the term in Eq. (3.15) with  $n = 0$ . Then  $\Delta^2 = T|U|^2\chi_0(0)/(1 - |U|\chi_0(0))$ . Insertion of this self energy into the one electron Green function allows one to evaluate the bare susceptibility in Eq. (3.16) at zero frequency. Earlier work [75] indicated that any degree of self-consistency in the ‘bare’ susceptibility drives the superconducting transition (signalled by  $1 = |U|\chi_0(0)$ ) to zero temperature. Adopting this requirement in this case gives the parameter  $\Delta^2$  in terms of  $|U|$  and  $\mu'$ . The number equation, Eq. (2.38), provides a second relation between  $\Delta^2$  and  $\mu'$ ; with these two equations all the zero temperature properties can be obtained analytically. Thus, for the chemical potential one obtains

$$\mu' = -\frac{|U|}{2}(1 - n), \quad (3.26)$$

which, remarkably, is the part of the exact result in Eq. (3.5) that survives in the  $T \rightarrow 0$  limit. Thus, the suppression of the Thouless instability to zero temperature is a feature in common with higher dimensional solutions.

In the case of the TPSC approximation, inverting the number equation, Eq. (2.38), where  $G^{(1)}(i\omega_m)$  given by Eqs. (3.19), (3.18) is used, leads to the following relation:

$$\mu'^{(1)} = \frac{(|U_{pp}| - |U|)}{2}(1 - n) - T \ln \left( \frac{2 - n}{n} \right) \quad (3.27)$$

In the  $T \rightarrow 0$  limit, solving Eq. (3.20) for  $\langle n_{\uparrow}n_{\downarrow} \rangle$  self-consistently drives the irreducible vertex  $U_{pp}$  to zero, so the zero-temperature result is identical to Eq. (3.26).

### 3.4.2 Two-particle correlations

We can press further the comparison between different approximations, and in particular probe two-particle correlations. An easy way to do this is by examining the energy per lattice site  $E$ . We use the exact relation [60] (in

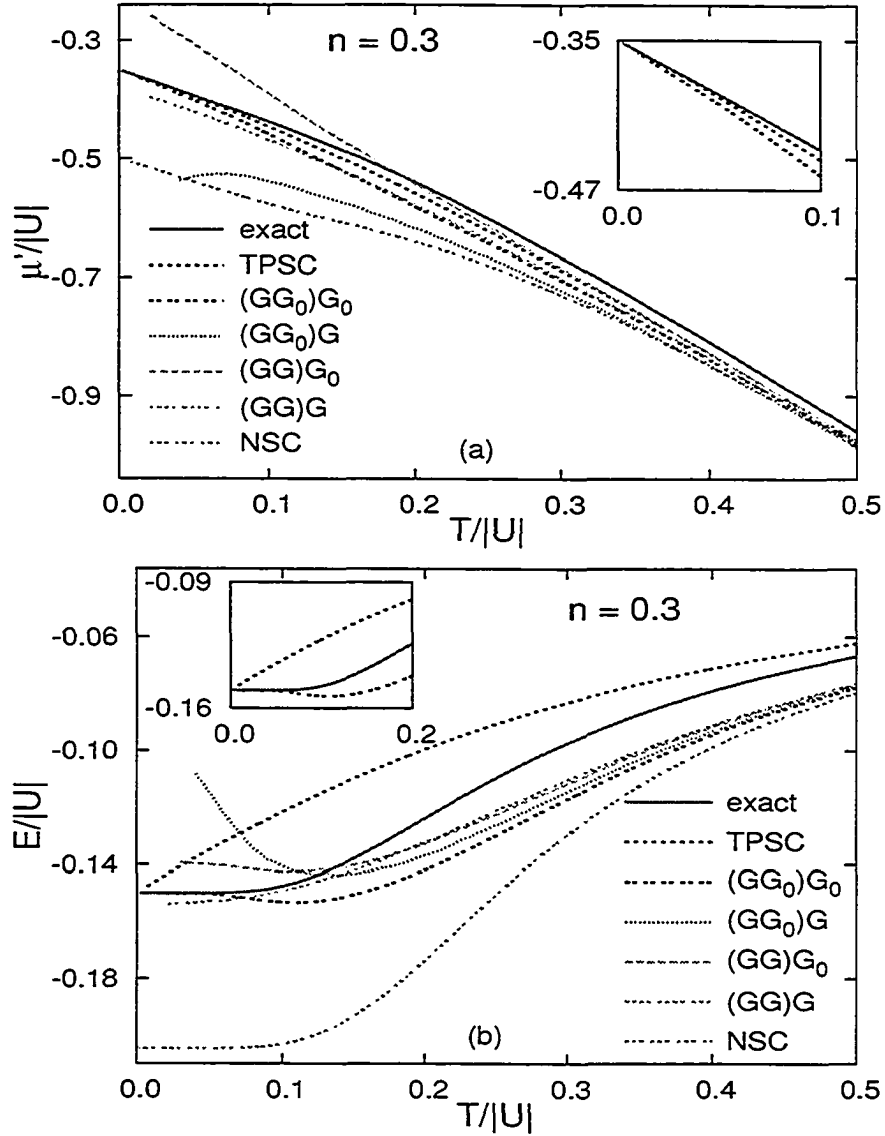


Figure 3.2: A comparison of the different approximations at  $n = 0.3$ ; (a)  $\mu'$  vs. temperature; (b) energy (according to Eq. (3.29)) vs. temperature. The different T-matrix formulations are indicated according to Eqs. (3.15), (3.16). Note that the TPSC result (first step only) and the  $(GG_0)G_0$  T-matrix approximation are the most accurate; they both become exact as  $T \rightarrow 0$ . The insets focus on the TPSC and  $(GG_0)G_0$  results at low temperatures; note in (b) how well the  $(GG_0)G_0$  curve approaches the exact result over an extended temperature range.

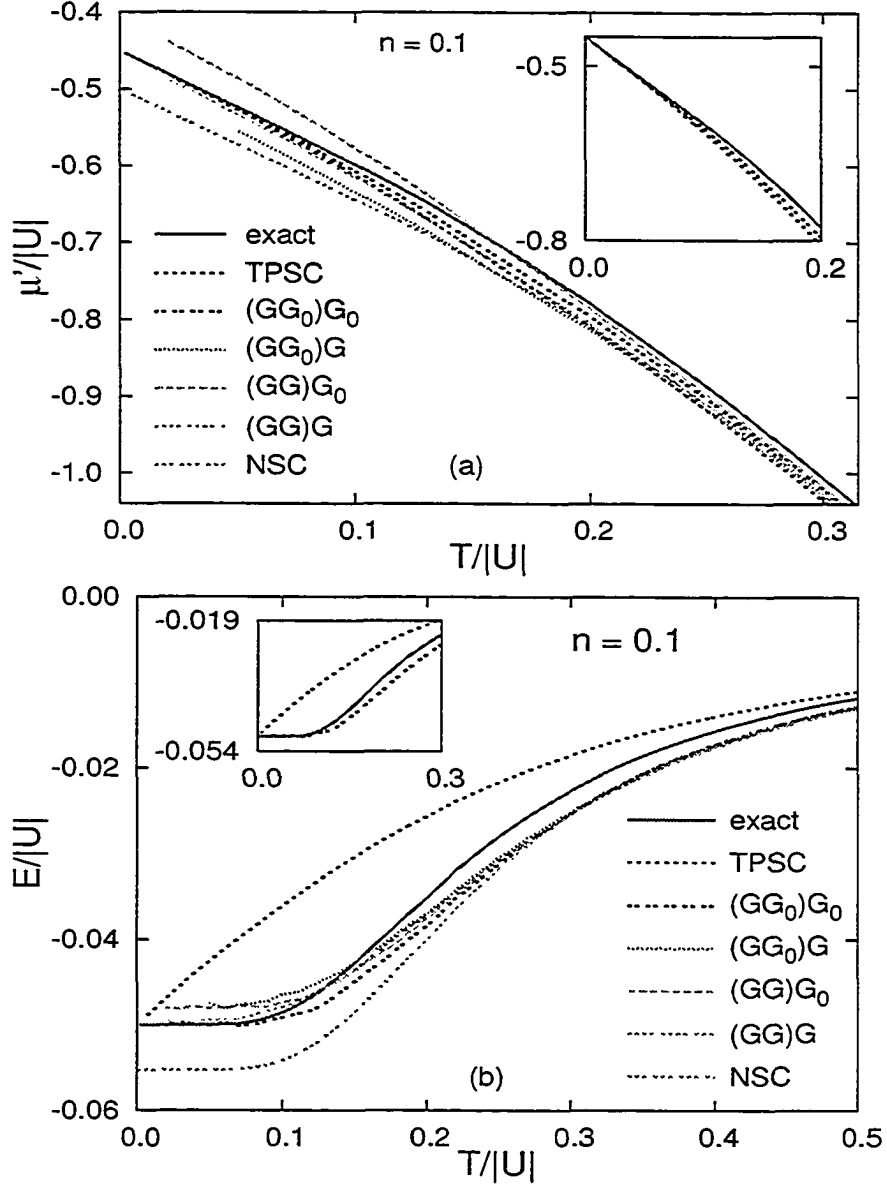


Figure 3.3: Same as Fig. 3.2 but for a lower density,  $n = 0.1$ ; (a)  $\mu'$  vs. temperature; (b) energy (according to Eq. (3.29)) vs. temperature. The insets focus on the TPSC and  $(GG_0)G_0$  results at low temperatures. Note that, for this density, the  $(GG_0)G_0$  T-matrix approximation is more accurate than TPSC result; again, they both become exact as  $T \rightarrow 0$ .

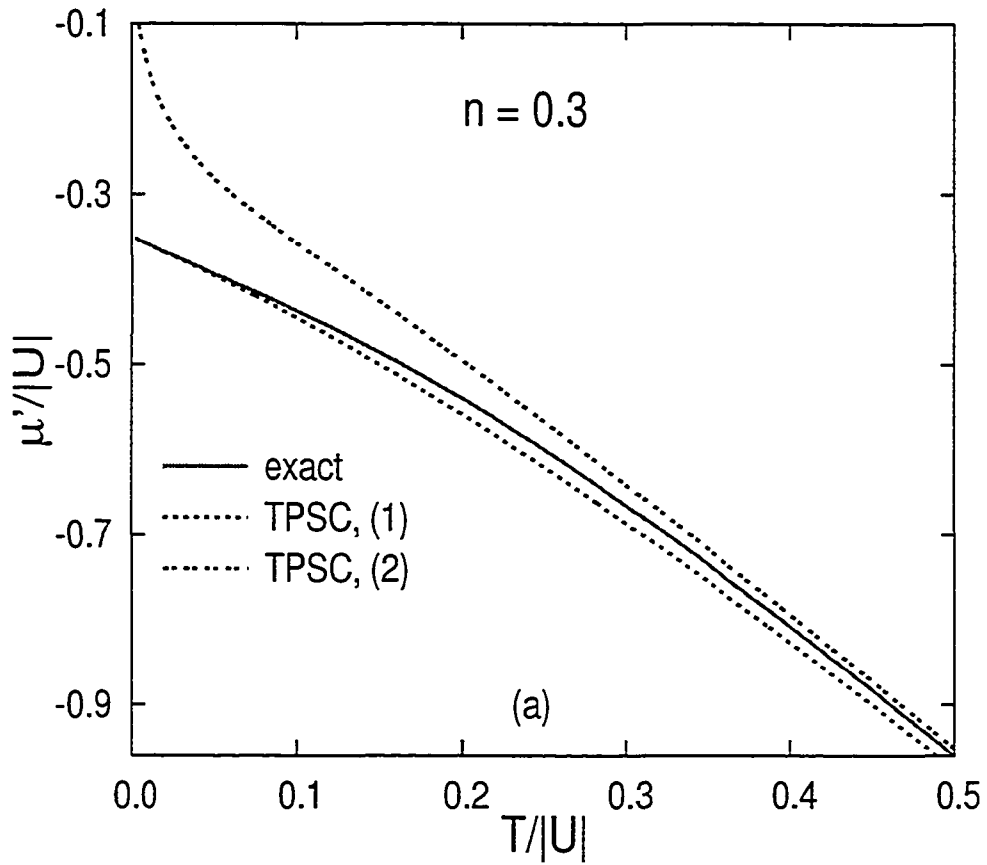


Figure 3.4: Level 1 (Eq. (3.27)) vs. level 2 of the TPSC approximation at  $n = 0.3$ . Note that ‘improving’ the approximation fails spectacularly in the low temperature regime.

the atomic limit there is no kinetic energy term)

$$E = \frac{1}{\beta} \sum_m \Sigma(i\omega_m) G(i\omega_m) \exp(i\omega_m 0^+), \quad (3.28)$$

to obtain the energy at any temperature, in the T-matrix theories. This equation and the atomic limit version of Eq. (2.40) lead to the following relation between  $E$  and  $\langle n_\uparrow n_\downarrow \rangle$ :

$$E = -|U| \langle n_\uparrow n_\downarrow \rangle + |U| \left(\frac{n}{2}\right)^2. \quad (3.29)$$

Normally,  $E$  would be simply proportional to the double occupancy in the atomic limit. However, because of the special form of the Hamiltonian in Eq. (3.1), the contribution of the Hartree diagrams is not included in the self-energy, and this is reflected in the second term on the right-hand-side of Eq. (3.29).

Fig. 3.2(b) shows the energy determined within the various approximation schemes along with the exact and the TPSC result, for  $n = 0.3$ . Once again the TPSC and  $(GG_0)G_0$  results are exact at zero temperature. However, the TPSC result deviates immediately for  $T > 0$ , while the  $(GG_0)G_0$  result follows closely over some temperature range. The same behavior is observed for the lower density ( $n = 0.1$ ) exemplified in Fig. 3.3(b), where the better agreement of the  $(GG_0)G_0$  T-matrix persists over an extended temperature range. That this latter result is true follows also from the analytical work described at the end of §3.4.1.

For the TPSC theory, the results used in the above analysis are for the first step in the TPSC approach described in §3.3 following Ref. [76]. If one presses further with the second step, the results deteriorate, as illustrated in Fig. 3.4.

### 3.4.3 Spectral properties

To probe further the analytical structure of the various approximations, one would like to examine the spectral function. To that end, the Green function on the real axis is needed (see Appendix B):

$$A(\omega) \equiv -\text{Im}G(\omega + i\delta)/\pi \quad (3.30)$$

The analytic continuation of the exact finite temperature Green function from the imaginary axis to the whole complex plane is trivial (and was implicit

in §3.1),  $i\omega_m$  is simply replaced by  $z$ . Once this is done, one can evaluate it anywhere in the complex plane, including just above the real axis ( $z = \omega + i\delta$ ,  $\delta \rightarrow 0^+$ ). As mentioned in §3.1, the exact Green function in Eq. (3.2) has two poles, resulting in two  $\delta$ -functions in the spectral function, separated by  $|U|$ :

$$A(\omega) = \left(1 - \frac{n}{2}\right) \delta\left(\omega + \mu' - \frac{n}{2}|U|\right) + \frac{n}{2} \delta\left(\omega + \mu' + |U|\left(1 - \frac{n}{2}\right)\right) \quad (3.31)$$

The spectral weight is distributed between the two  $\delta$ -functions, and the sum of their weight factors equals one, as it should.

For the TPSC approach, the analytic continuation of  $G$  is just as trivial (and again, was implicit in §3.3), since the atomic limit allows closed form expressions for  $\Sigma$  and  $G$  to be derived as well. At the first level of the approximation the self-energy is a constant, and the noninteracting propagator accommodates a simple Hartree-like renormalization. This accounts for a single pole in the one-particle propagator, which in turn produces a single  $\delta$ -function in the spectral function

$$A^{(1)}(\omega) = \delta\left(\omega + \mu'^{(1)} - (|U_{pp}| - |U|)\frac{1-n}{2}\right), \quad (3.32)$$

in obvious disagreement with the exact result. The result obtained in the second step of the TPSC approximation does contain two poles:

$$A^{(2)}(\omega) = c_1 \delta(\omega + \mu'^{(2)} - z_1) + c_2 \delta(\omega + \mu'^{(2)} - z_2), \quad (3.33)$$

where the notations used are the same as in Eq. (3.24). However, as shown in Fig. 3.5, it is fairly inaccurate.

The extrapolation of self-consistent T-matrix theories to the real axis is not so straightforward, and it must be handled with care. In Fig. 3.5 the spectral function for the  $(GG_0)G_0$  has been obtained through Padé approximants (see §B.2). As already noted, the  $(GG_0)G_0$  theory reproduces the exact result at zero temperature. The agreement with the exact result at low temperatures is remarkable. Thus, even though both the TPSC theory and the  $(GG_0)G_0$  T-matrix approximation give exact results for the chemical potential and the energy at low temperatures, only the latter fully reproduces the exact result as a function of frequency. Inspection of Fig. 3.2 shows that ‘improving’ the degree of self-consistency deteriorates the agreement. This would mean that at low temperatures some cancellation occurs between the fully self-consistent T-matrix diagrams ( $(GG)G$  theory) and the omitted vertex corrections. This possibility remains to be shown, however.



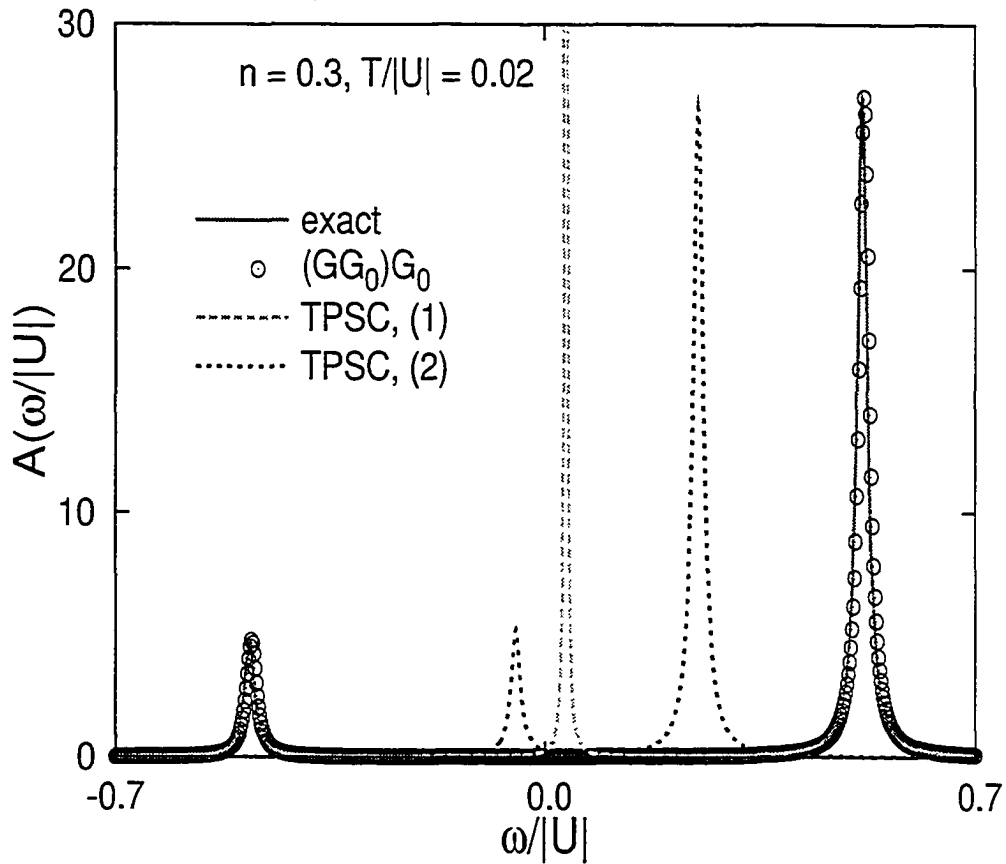


Figure 3.5: The spectral function for the  $(GG_0)G_0$  T-matrix approximation (symbols), compared with the exact result (solid curve, Eq. (3.31)). The remarkable agreement shows that only partial self-consistency is a requirement to reproduce the exact result. The TPSC result (both first (Eq. (3.32)) and second (Eq. (3.33)) steps) are poorer in comparison. We have used a small artificial broadening,  $\delta = 0.01|U|$  to plot these results.

### 3.4.4 Discussion

The agreement of the  $(GG_0)G_0$  T-matrix and TPSC approximations for the thermodynamics (i.e. the chemical potential) at  $T = 0$  (note that neither approximation is particularly accurate at intermediate temperatures) raises the question of the origin of the effective potential,  $|U_{pp}|$ , in the TPSC theory. Within a conserving approximation, a frequency-independent irreducible vertex,  $|U_{pp}|$ , is accompanied by single electron propagators that, aside from a simple Hartree-like correction, are otherwise unrenormalized [76]. The  $(GG_0)G_0$  T-matrix approach, however, suggests that the origin of an effective interaction is from the (partial) renormalization of the single electron propagator. That is, we can construct a theory that appears similar to the TPSC theory, i.e. with unrenormalized propagators everywhere in Eqs.(3.15), (3.16), but with an *effective* interaction vertex. Eq.(3.15) suggests this will be accomplished by

$$|U|\chi_0(i\nu_n) \equiv |U_{\text{eff}}|\chi_{00}(i\nu_n), \quad (3.34)$$

where  $\chi_{00}(i\nu_n) = \frac{1}{\beta} \sum_m G_0(i\omega_m)G_0(-i\omega_m + i\nu_n)$ . Note that this requires  $|U_{\text{eff}}|$  to depend on Matsubara frequency, but, in the spirit of TPSC (and many Parquet-like treatments of higher order corrections [73]), we will use Eq. (3.34) at zero Matsubara frequency to define an effective potential. Comparisons with  $|U_{pp}|$  as obtained in the TPSC formalism, illustrated in Fig. 3.6 show quantitative discrepancies, particularly as the temperature approaches zero. Thus, the two theories differ more substantively than Eq. (3.34) would suggest.

This difference is clearly illustrated in the results for the spectral function, Fig. 3.5. In the  $(GG_0)G_0$  approximation the spectral function is *exact* at low temperatures, while in the TPSC approximation it is qualitatively wrong in the first step. This also indicates that this level of T-matrix approximation does not just ‘mimic’ the TPSC result as was found above, in connection to Eq. (3.34). Rather, it would appear that a more profound cancellation of diagrams occurs, the significance of which eludes us a present.

Here we conclude our critical examination of various approximations for the attractive Hubbard model in the dilute and strong coupling limit. We find that minimal self-consistency in the T-matrix approximation (the  $(GG_0)G_0$  theory promoted in particular in Ref. [72]) and the TPSC theory of Vilk-Tremblay [29] both reproduce the exact result best, particularly at low temperatures, where both become exact. Surprisingly, ‘improving’ the degree of self-consistency within a T-matrix approach leads to less accurate results.

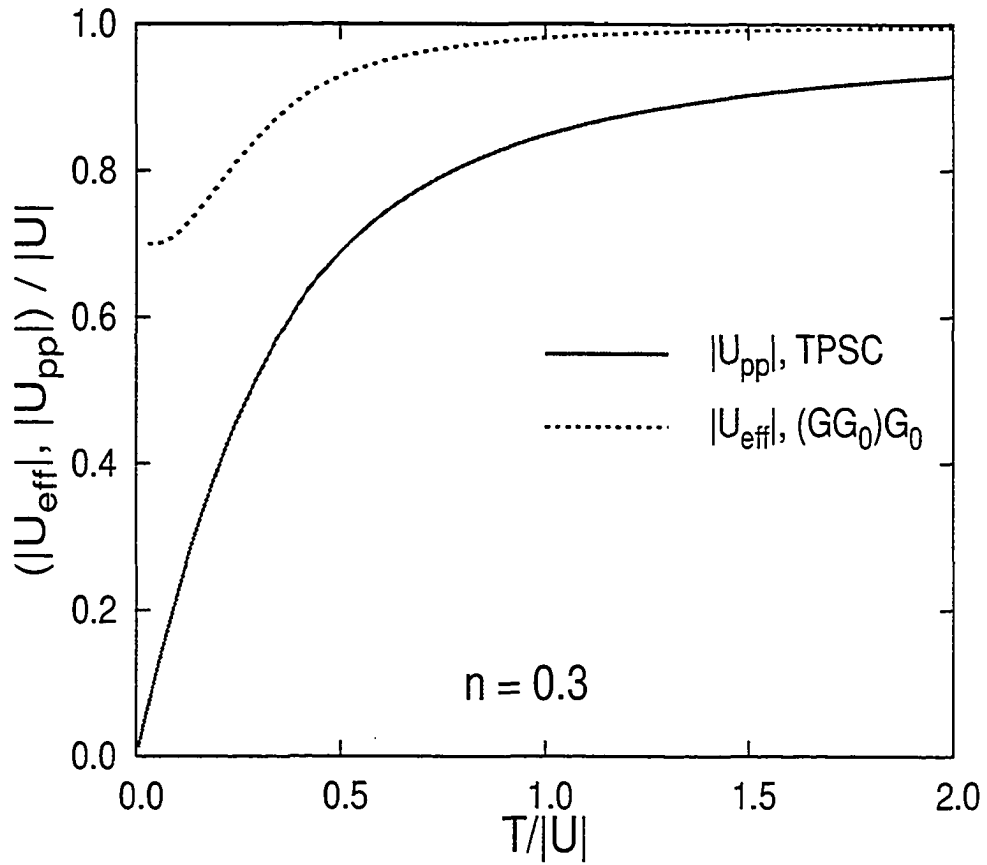


Figure 3.6: The 'effective interaction' associated with the  $(GG_0)G_0$  version of the T-matrix approximation (see Eq. (3.34)) vs. the irreducible vertex of the TPSC approximation, at  $n = 0.3$ .

Two-particle correlations (summarized in the total energy in this work) are faithfully reproduced by the  $(GG_0)G_0$  calculation for a range of low temperatures, and, finally, the one electron spectral function is remarkably accurate, even at nonzero temperature. These results suggest that, at least for low electron densities, this T-matrix formulation is useful for higher dimension calculations, which make the object of the next chapter.

# Chapter 4

## Higher Dimensions

Atomic limit (0-dimensional) work provided means to investigate how well different approximations worked, at least in the strong coupling limit. While we believe that such work is insightful, it needs to be extended to higher dimensions, in order to be relevant to real systems.

In this chapter, we will explore the ability of T-matrix-type approximations to produce a pseudogap in the one-particle spectrum for higher dimension lattice fermions provided with an attractive interaction. In this case, the progress that can be made analytically is limited, and one has to rely on heavy computational work. The difficulties are twofold: on one hand, with increased dimensionality, the numerical calculations become more computationally costly; on the other hand, as a matter of practicality, we perform our calculations on finite lattices, and we must find ways to manage finite size effects, especially near instabilities (ideally, one is interested in the thermodynamic limit,  $N \rightarrow \infty$ ). An additional challenge is related to the necessity to extrapolate to the real frequency axis, when one seeks to study dynamic properties of the model. We will address these issues while investigating the effect of pairing correlations on the normal state of the AHM.

### 4.1 The quest for the Pseudogap

We motivated our work by the presence of an unconventional pseudogap state above the superconducting transition on the underdoped side of the highly anisotropic, quasi-two-dimensional High  $T_c$  cuprates. This really means a depletion of single-particle states near the Fermi energy, anticipative of the

true gap in the density of states in the superconducting phase of these materials. Adopting the ‘precursor scenario’ line of thought, we have described a technique designed to incorporate pairing fluctuations into single-particle properties - the T-matrix approximation. There are many interpretations to this theory, the merits and shortcomings of which were outlined in §2.4 and investigated in greater detail in the atomic limit in Chapter 3. We hope to have given the reader a sense of the great deal of effort invested in T-matrix-type calculations by many researchers over the years. In addition, arguments against such formulations and in favor of alternate treatments requiring vertex corrections have also appeared, and we have mentioned the TPSC approach of Vilk-Tremblay [29]. The ‘lack of satisfaction’ with the T-matrix approaches can be traced to the difficulty of studying two-dimensional systems in which the Mermin-Wagner theorem precludes the existence of true long-range order. Thus no realistic approach of this type applied to two dimensional (2D) systems can aim to a quantitative agreement with experimental values of  $T_c$  in cuprate materials; by necessity  $T_c$  from any Thouless criterion approach (by which we refer to any attempt to identify  $T_c$  through a diverging pair susceptibility) must be zero. In the case of the T-matrix approximation, we have shown that self-consistency ‘does the trick’, even in minimal formulation. Once the Mermin-Wagner result is restored, one can look for a pseudogap signature in the single-particle properties in the normal state, above  $T_c = 0$ . (To connect with real cuprate materials, their finite  $T_c$  is necessarily the result of coupling between the planes, unless the transition is to the Kosterlitz-Thouless phase [82], the existence of which is still debated in the cuprates [83]; the Kosterlitz-Thouless physics is beyond the competence of T-matrix-type approximations.)

Alternatively, one can avoid the problem with the Mermin-Wagner theorem by studying a three dimensional (3D) system. In this case we avoid the necessity (and the computational effort) of using a self-consistent theory. For an infinite lattice in three dimensions, the NSC Thouless criterion gives precisely the BCS result for  $T_c$ . It is true that most of the research on the subject associates the pseudogap with the lower dimensionality of the cuprates; in terms of fluctuations, this is simply a statement that one expects enhanced fluctuations towards the low-temperature phase, the lower the effective dimensionality of the system. However, an interesting question is: should one expect a pseudogap in a 3D system with purely electronic attractions? In fact, we will show that a pseudogap does appear in the single-particle density of states of the 3D AHM at half filling, even at weak coupling. Moreover,

the weak coupling magnitude of the pseudogap compares well with the BCS gap that would be found at zero temperature.

## 4.2 Imaginary axis calculations - finite size effects

Any numerical treatment of a lattice model suffers from finite size effects, *i.e.* the results depend on the size of the system considered. While at high enough temperatures the differences are usually small, the size dependence becomes important near instabilities. The larger the size of the system one can afford to work with, the closer the results to the thermodynamical limit (appropriate for real systems, with very large  $N$ ). For 1D systems one can normally afford to increase the size of the lattice until the results stop changing, indicating that the thermodynamic limit has been reached. This procedure becomes less practical with every added dimension. Moreover, the ability to increase the size might not be enough when one has to deal with diverging integrands. We will illustrate this issue by using the NSC T-matrix to solve for the AHM in one, two and three dimensions. We stress that this is not intended to provide an adequate solution for the 1D and 2D cases, where we have established that the NSC T-matrix approximation is not adequate. But it will demonstrate where the difficulty comes from and how increasing dimensionality changes the nature of the problem.

### 4.2.1 NSC T-matrix

In the NSC T-matrix approximation, the independent pairing susceptibility is obtained by replacing the fully dressed one-particle Green function in Eq. (2.32) with the noninteracting one:

$$\chi_{00}(\vec{q}, i\nu_n) = \frac{1}{\beta N} \sum_{\vec{k}} \sum_l G^0(\vec{k}, i\omega_l) G^0(-\vec{k} + \vec{q}, -i\omega_l + i\nu_n), \quad (4.1)$$

where  $G^0(\vec{k}, i\omega_m) = [i\omega_m - \xi_{\vec{k}}]^{-1}$ . This substitution allows for the frequency summation in Eq. (4.1) to be done analytically, leading to

$$\chi_{00}(\vec{q}, i\nu_n) = -\frac{1}{N} \sum_{\vec{k}} \frac{1 - f(\xi_{\vec{k}}) - f(\xi_{-\vec{k}+\vec{q}})}{i\nu_n - \xi_{\vec{k}} - \xi_{-\vec{k}+\vec{q}}}. \quad (4.2)$$

In the above equations, like elsewhere in this thesis,  $i\omega_m \equiv i\pi T(2m - 1)$  and  $i\nu_n \equiv i2\pi Tn$ , with  $m, n \in \mathbb{Z}$ , are the fermionic and bosonic Matsubara frequencies, respectively,  $f(x) \equiv 1/(e^{\beta x} + 1)$  is the Fermi distribution function and  $\xi_{\vec{k}} \equiv (\epsilon_{\vec{k}} - \mu')$  represents the independent one-particle energy measured from the ‘corrected’ chemical potential  $\mu'$ . Here, as in the rest of this work, we understand that  $\mu'$  differs from the true chemical potential by a Hartree term:  $\mu' = \mu + |U|n/2$ . In what follows we will ignore the prime in the notation, for simplicity.

The self-energy, according to the NSC version of Eq. (2.35), is then given by

$$\begin{aligned} \Sigma(\vec{k}, i\omega_m) &= -\frac{|U|^2}{\beta N} \sum_{\vec{q}, n} \chi(\vec{q}, i\nu_n) G^0(-\vec{k} + \vec{q}, -i\omega_m + i\nu_n) \\ &= -\frac{|U|^2}{\beta N} \sum_{\vec{q}, n} \frac{\chi_{00}(\vec{q}, i\nu_n)}{1 - |U|\chi_{00}(\vec{q}, i\nu_n)} G^0(-\vec{k} + \vec{q}, -i\omega_m + i\nu_n). \end{aligned} \quad (4.3)$$

All the quantities entering Eq. (4.3) are known. Nonetheless it is not in a convenient form for two reasons. First, the Matsubara sum extends over all  $n \in \mathbb{Z}$ . Numerically, it must be truncated, and it is important that this is done in some sensible manner. Secondly, we use discrete momentum sums over the First Brillouin Zone (FBZ) of the finite size lattice considered for numerical calculations. While this works well at high temperatures, it fails for temperatures and chemical potentials near the Thouless curve. As  $T \rightarrow T_c$ , the Thouless criterion  $1 = |U|\chi_{00}(\vec{q} = 0, i\nu_n = 0)$  leads to a diverging pair susceptibility  $\chi$ . Using discrete momentum sums, the  $(\vec{q} = 0, i\nu_n = 0)$  contribution, which contains the pairing instability, will lead to a self-energy that diverges *in any dimension*. This is the expected behavior in 1D and 2D, however, a space phase argument following the Mermin-Wagner theorem [77] shows that the self-energy should *not* diverge in 3D. We need to remedy the numerical evaluation of Eq. (4.3) to capture this distinction between one, two and three dimensions.

## 4.2.2 Low $\vec{q}$ analytical integration

In order to do that, we isolate the  $(\vec{q} = 0, i\nu_n = 0)$  contribution to the sum in Eq. (4.3). As a results, the self-energy can be separated into a singular and a non-singular part:

$$\Sigma(\vec{k}, i\omega_m) = \Sigma^s(\vec{k}, i\omega_m) + \Sigma^{ns}(\vec{k}, i\omega_m). \quad (4.4)$$



The singular part

$$\Sigma^s(\vec{k}, i\omega_m) = -\frac{|U|^2}{\beta N} \frac{\chi_{00}(\vec{q}=0, 0)}{1 - |U|\chi_{00}(\vec{q}=0, 0)} G^0(-\vec{k} + (\vec{q}=0), -i\omega_m) \quad (4.5)$$

diverges as  $(T - T_c)^{-1}$  in all dimensions. The remaining contribution is

$$\Sigma^{ns}(\vec{k}, i\omega_m) = -\frac{|U|^2}{\beta N} \sum'_{\vec{q}, n} \frac{\chi_{00}(\vec{q}, i\nu_n)}{1 - |U|\chi_{00}(\vec{q}, i\nu_n)} G^0(-\vec{k} + \vec{q}, -i\omega_m + i\nu_n). \quad (4.6)$$

Fig. 4.1 shows the FBZ for a  $8 \times 8$  square lattice. In this example, for each Matsubara frequency, the summand in Eq. (4.3) is evaluated at each momentum point and added up. For zero frequency, the singular contribution comes from the point marked with “0”, with the weight  $1/N$ . The correct results, corresponding to the thermodynamic limit, would involve a  $D$ -dimensional (two-dimensional, in the example in Fig. 4.1) integral over the whole FBZ. Treated numerically, even with a finer mesh, there will still be a singular contribution at point “0”, but with less and less weight, as  $N$  increases. Also, increasing  $N$  becomes more and more computationally costly.

Instead, we will use a low  $\vec{q}$  expansion for  $\chi_{00}$ , which allows an analytical treatment. It is true that this expansion is done here before the summation over the bosonic Matsubara frequencies, however, we assume we are in the renormalized classical regime, where the most important contribution comes from  $i\nu_n = 0$  [29]. The low  $\vec{q}$  expansion allows us to do the integration over the region around  $\vec{q} = 0$  *analytically*, and add to it the rest of the terms in the sum for a reasonably low size finite lattice. With this procedure we hope to capture the thermodynamic behavior with much smaller lattices. We will demonstrate shortly that it works remarkably well.

With the above considerations, we replace the singular part of the self-energy in Eq. (4.5) by

$$\Sigma^s(\vec{k}, i\omega_m) = -\frac{|U|^2}{\beta} \int_{-\vec{q}_0}^{\vec{q}_0} \frac{d^D q}{(2\pi)^D} \frac{\chi_{00}(\vec{q}, 0)}{1 - |U|\chi_{00}(\vec{q}, 0)} G^0(-\vec{k} + \vec{q}, -i\omega_m). \quad (4.7)$$

For small  $\vec{q}$ , the ‘bare’ pairing susceptibility  $\chi_{00}$  can be approximated by

$$\chi_{00}(\vec{q}, 0) \approx a^2 - b^2 q^2, \quad (4.8)$$

where  $q = |\vec{q}|$ ,  $a^2 = \chi_{00}(0, 0)$  and  $b^2 = -\frac{1}{2} \frac{\partial^2 \chi_{00}(\vec{q}, 0)}{\partial q^2} \Big|_{\vec{q}=0}$ . For practical purposes,  $a^2$  and  $b^2$  are obtained by fits to  $\chi_{00}(\vec{q}, 0)$  at  $\vec{q} = 0$  and  $\vec{q} = \vec{q}_0$ . Fig. 4.2

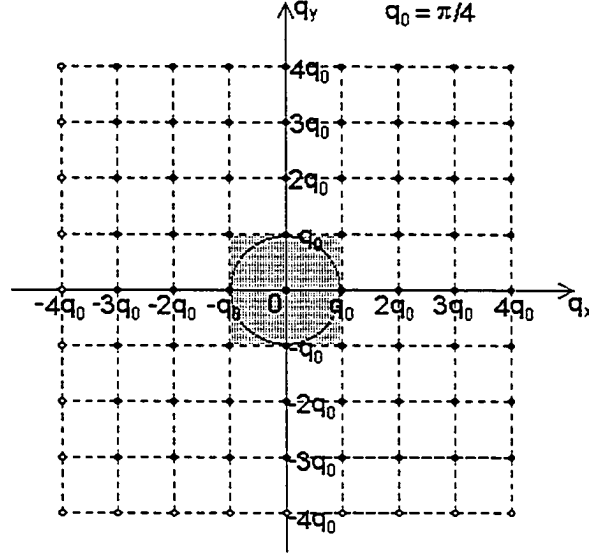


Figure 4.1: First Brillouin Zone for a 8x8 square lattice. The region around the origin is indicated for analytical treatment, as discussed in text.

shows an example in 1D. We note that in 2D and 3D we will use an average value of  $b^2$ , as fitting  $\chi_{00}(\vec{q}, 0)$  along different directions between  $\vec{q} = 0$  and  $\vec{q} = \vec{q}_0$  results in slightly different values for this parameter. Fig. 4.3 illustrates that the 3D fit reproduces very accurately the thermodynamic limit result at low  $\vec{q}$ , even with the average value of the parameter  $b^2$  from fits along  $(0,0,0)-(q_0,0,0)$ ,  $(0,0,0)-(q_0,q_0,0)$  and  $(0,0,0)-(q_0,q_0,q_0)$ .

If a low  $q$  expansion is also performed for  $G^0(-\vec{k} + \vec{q}, -i\omega_m)$ , the following compact form emerges for  $\Sigma^s$ , valid at small  $\vec{q}$ :

$$\Sigma^s(\vec{k}, i\omega_m) = \frac{|U|}{\beta} \frac{2}{(2\pi)^D} g_{\vec{k}} \int_0^{\vec{q}_0} d^D q \left\{ -1 + \frac{1}{A + Bq^2} \right\} \left\{ 1 + q^2 d_{\vec{k}} \right\}, \quad (4.9)$$

where  $D$  is the dimensionality and we have introduced the following notations:

$$\begin{aligned} A &\equiv 1 - |U|a^2, \quad B \equiv |U|b^2, \\ g_{\vec{k}} &\equiv 1/(i\omega_m + \xi_{\vec{k}}) \quad \text{and} \\ d_{\vec{k}} &\equiv \frac{g_{\vec{k}}^2}{D} \left[ \sum_{i=1}^D \left( \frac{\partial \xi_{\vec{k}}}{\partial k_i} \right)^2 \right] - \frac{g_{\vec{k}}}{2D} \left[ \sum_{i=1}^D \frac{\partial^2 \xi_{\vec{k}}}{\partial k_i^2} \right]. \end{aligned} \quad (4.10)$$

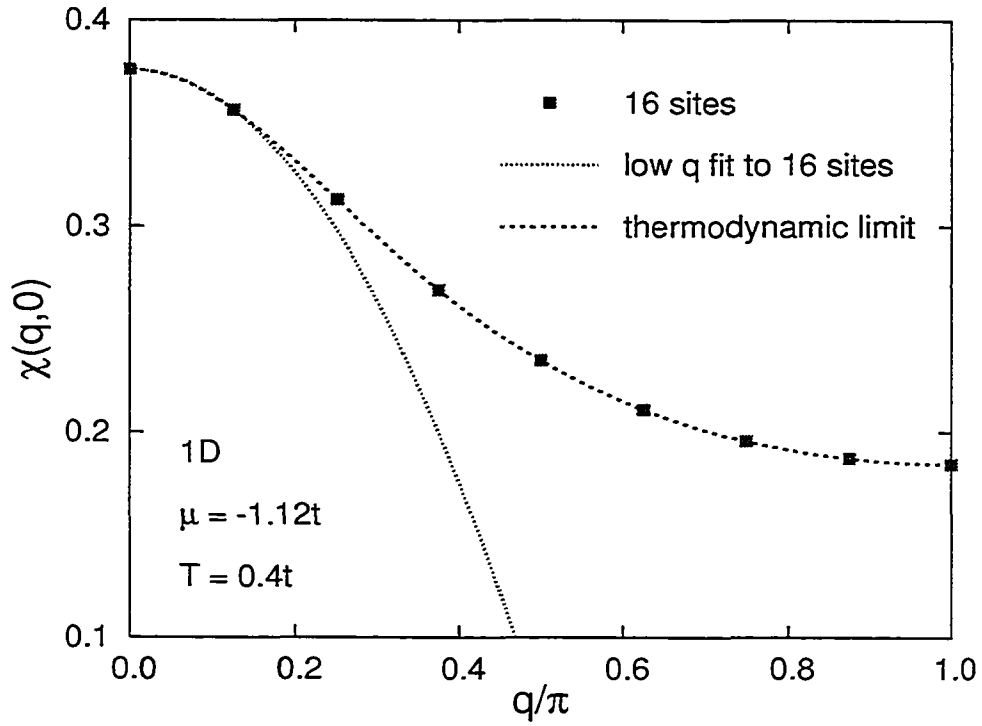


Figure 4.2: Real part of the noninteracting susceptibility (Eq. (4.2)) vs.  $q$  in 1D. The fit is obtained as described in text, based on the two lowest points ( $q = 0$  and  $q = \pi/8$ ); clearly, it reproduces very accurately the thermodynamic limit at low  $q$ .

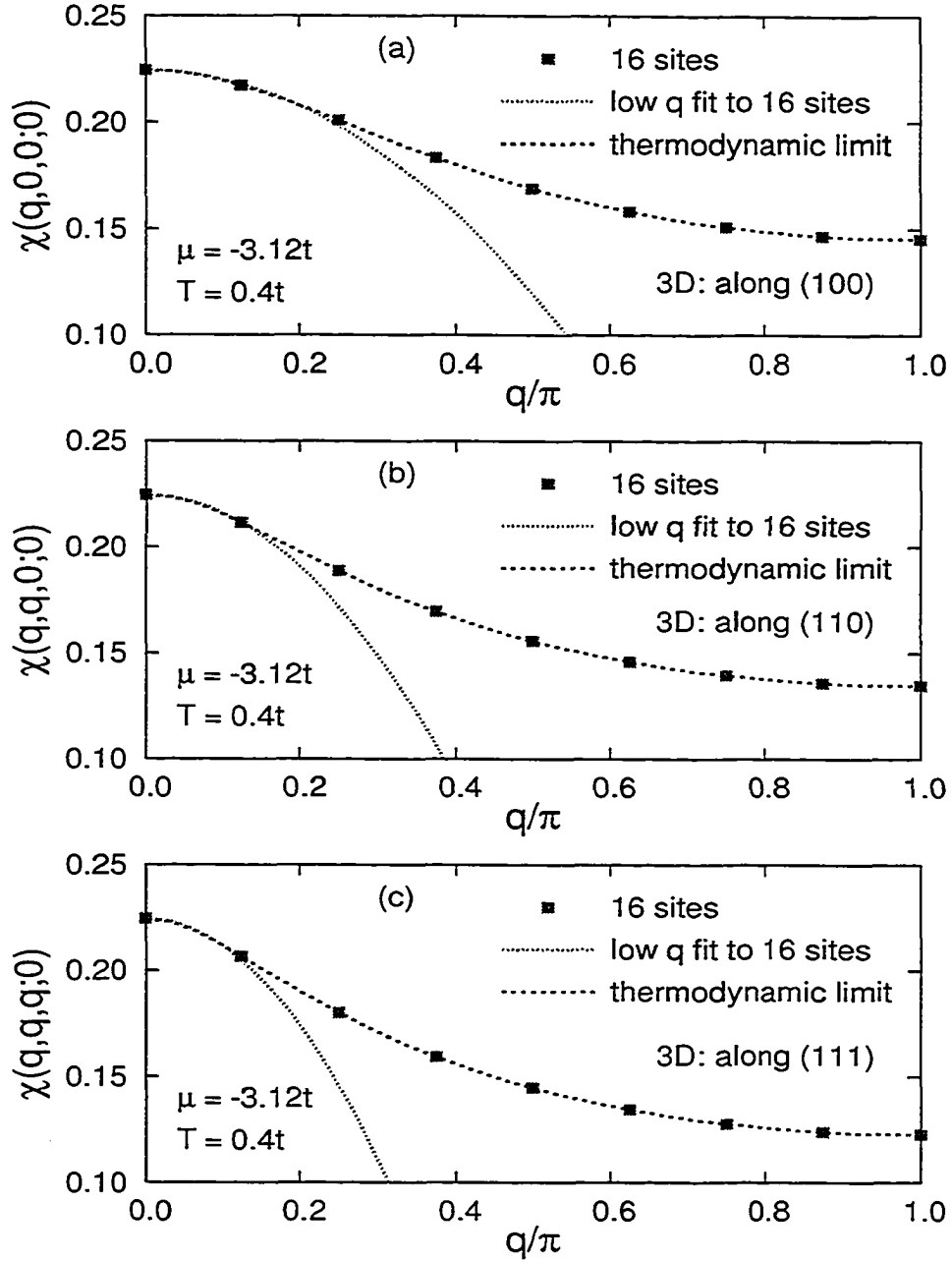


Figure 4.3: Real part of the noninteracting susceptibility (Eq. (4.2)) vs.  $q$  in 3D. The agreement with the thermodynamic limit at low  $q$  is remarkable, given that the fit has been obtained with the average fitting parameters along the (100), (110) and (111) directions.

$A$  and  $B$  are both positive numbers, however, the definition of  $a^2$  makes it clear that  $A$  is approaching zero as  $T \rightarrow T_c$ . Note that in deriving Eq. (4.9) we made use of the symmetry of the hyper-cubic lattice in  $D$  dimensions. With the additional definition

$$F_{\vec{k}}(q) \equiv \left\{ -1 + \frac{1}{A + Bq^2} \right\} \left\{ 1 + q^2 d_{\vec{k}} \right\}, \quad (4.11)$$

we will next specialize Eq. (4.9) to one, two and three dimensions.

### 1D results

In 1D, using the definition in Eq. (4.11) into Eq. (4.9) leads to the following expression for the singular part of the self-energy:

$$\Sigma^s(k, i\omega_m) = \frac{|U|}{\beta\pi} g_k \int_0^{q_0} dq F_k(q) \quad (4.12)$$

All the integrals in the above equation are elementary, with the following result:

$$\begin{aligned} \Sigma^s(k, i\omega_m) = \frac{|U|}{\beta\pi} g_k \left\{ \underbrace{-q_0 + \frac{1}{\sqrt{AB}} \arctan\left(\frac{q_0}{\sqrt{A/B}}\right)}_{\text{singular}} \right. \\ \left. + d_k \left[ -\frac{q_0^3}{3} + \frac{1}{B} \left( q_0 - \sqrt{\frac{A}{B}} \arctan\left(\frac{q_0}{\sqrt{A/B}}\right) \right) \right] \right\}. \quad (4.13) \end{aligned}$$

We have underlined the singular contribution in Eq. (4.13), all the other terms being finite. It is correct that this quantity diverges in 1D. We note, however, that handling the small  $\vec{q}$  integration analytically weakened the divergence; the singular term behaves now as  $1/\sqrt{T - T_c}$ , instead of the incorrect  $1/(T - T_c)$ .

Fig. 4.4 shows results for the number density in 1D, computed for different lattice sizes with and without the small  $\vec{q}$  correction. The results computed on a 128 site lattice are essentially in the thermodynamic limit, both the regular lattice summation and the low  $\vec{q}$  analytical treatment yielding virtually the same result. The figure shows how remarkably this method works; even with the smallest lattice size shown, the low  $\vec{q}$  integration technique produces results very close to the thermodynamic limit.

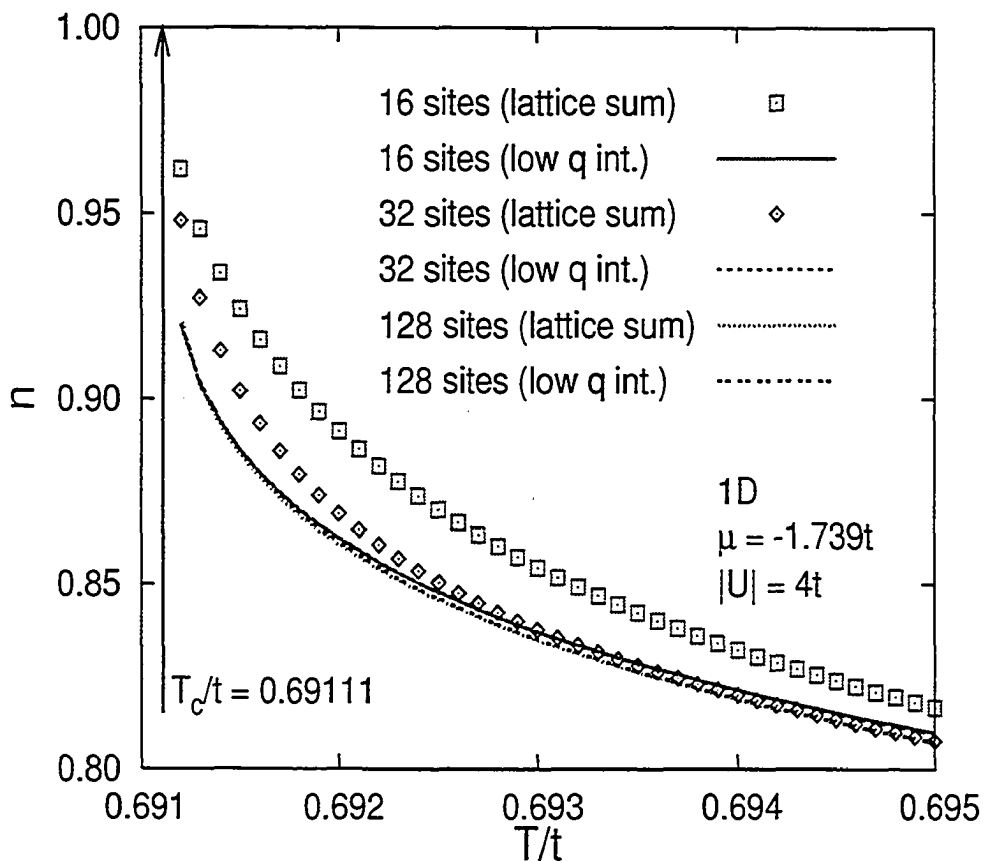


Figure 4.4: 1D - Electronic density vs. temperature computed with and without the analytical correction for small  $q$  (Eq. (4.13)). The results computed on a 128 site lattice are essentially in the thermodynamic limit, and there is barely any difference between the two procedures (the corresponding curves are on top of one another). For the other two lattice sizes shown, the refinement discussed in text clearly leads to a much more accurate answer than just using lattice sums.

## 2D results

Rigorously, the refinement to 2D requires an integration over a square with side of length  $2q_0$  (the filled square in Fig. 4.1). Going to polar coordinates we rewrite Eq. (4.9) with  $D = 2$  (in deriving Eq. (4.9) we already took into account the square symmetry of the lattice, so the domain of integration is reduced to the first quarter of the above-mentioned square):

$$\Sigma^s(\vec{k}, i\omega_m) = \frac{|U|}{2\beta\pi^2} g_{\vec{k}} \int_0^{\pi/2} d\varphi \int_0^{q_0(\varphi)} q dq F_{\vec{k}}(q), \quad (4.14)$$

where we have used the same definitions as in Eqs. (4.10), (4.11). The upper limit on the second integral,  $q_0(\varphi)$ , follows the edge of the elementary square. For the sake of simplicity we will integrate over a disc of radius  $q_0$  instead, and adjust the weight associated with the contribution to the discrete sum from the corner points to account for the missing area. We have checked numerically (both in 2D and in 3D, where we integrate over a sphere instead of a cube) that the difference to the final result is insignificant. With this simplification, the two integrals in Eq. (4.14) become independent and the result for self-energy is

$$\begin{aligned} \Sigma^s(k, i\omega_m) = \frac{|U|}{4\beta\pi} g_k \left\{ -\frac{q_0^2}{2} + \frac{1}{2B} \log \left( \frac{A + Bq_0^2}{A} \right) \right. \\ \left. + d_k \left[ -\frac{q_0^4}{4} + \frac{1}{B} \left( \frac{q_0^2}{2} - \frac{A}{2B} \log \left( \frac{A + Bq_0^2}{A} \right) \right) \right] \right\}. \quad (4.15) \end{aligned}$$

Thus we see that the 2D self-energy still diverges, now logarithmically with  $T - T_c$ .

As previously noted, a diverging self-energy will cause the number density to go to one, as evident from Eqs. (2.38), (2.36). This is still the case in two dimensions, but Fig. 4.5(a) shows that the singularity produced by the low  $\vec{q}$  integration technique is much weaker. Only very close to  $T_c$  is the effect of a logarithmically diverging self-energy visible at all, as opposed to the results obtained through regular lattice sums. Although thermodynamic limit results are not available for the 2D case, using the low  $\vec{q}$  treatment described above results in much less change with the size of the system, as shown in Fig. 4.5(b).

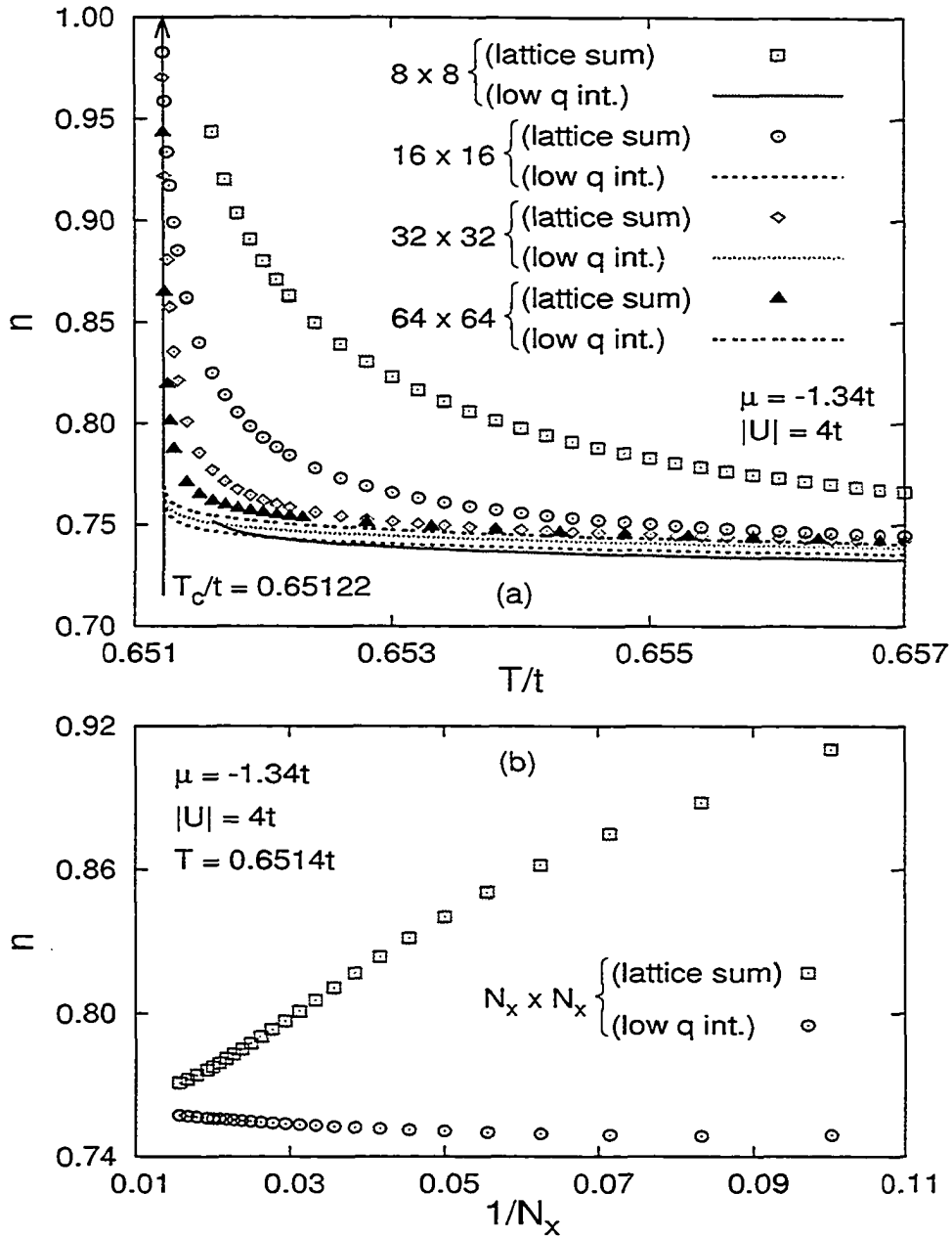


Figure 4.5: 2D - Electronic density vs. (a) temperature and (b)  $1/N_x$ , for a  $N_x \times N_x$  lattice, near the Thouless temperature. Note: in (a), while the effect of a very weak (logarithmic) singularity (see Eq. (4.15)) remains, it is exaggerated for the curves without the low  $q$  correction; in (b), the result with the low  $q$  analytical treatment converges much more quickly with lattice size.



### 3D results

Finally, in 3D we must integrate over a cube of side  $2q_0$  centered around origin. With the cubic symmetry already accounted for in Eq. (4.9) and going over to spherical coordinates, the 3D self-energy is given by:

$$\Sigma^s(\vec{k}, i\omega_m) = \frac{|U|}{4\beta\pi^3} g_{\vec{k}} \int_0^{\pi/2} d\varphi \int_0^{\pi/2} \sin(\theta) d\theta \int_0^{q_0(\theta, \varphi)} q^2 dq F_{\vec{k}}(q). \quad (4.16)$$

Like in the 2D case, we integrate over a sphere of radius  $q_0$  instead, and the upper limit on the third integral loses its  $\varphi$  and  $\theta$  dependence; the big difference in 3D is the Jacobian factor  $q^2$ , which removes the singular behavior as  $q \rightarrow 0$ . The result of the integration is:

$$\begin{aligned} \Sigma^s(k, i\omega_m) = & \frac{|U|}{8\beta\pi^2} g_k \left\{ -\frac{q_0^3}{3} + \frac{1}{B} \left[ q_0 - \sqrt{\frac{A}{B}} \arctan\left(\frac{q_0}{\sqrt{A/B}}\right) \right] \right. \\ & \left. + d_k \left[ -\frac{q_0^5}{5} + \frac{1}{B} \left( \frac{q_0^3}{3} - \frac{A}{B} q_0 + \left(\frac{A}{B}\right)^{3/2} \arctan\left(\frac{q_0}{\sqrt{A/B}}\right) \right) \right] \right\}. \quad (4.17) \end{aligned}$$

Inspection of Eq. (4.17) shows that as  $T \rightarrow T_c$ , *i.e.* as  $A \rightarrow 0$ , the self-energy remains finite. In fact, terms that diverged in 1D and 2D now vanish as  $A \rightarrow 0$ . As is apparent from Fig. 4.6, this leads to qualitatively different behavior in 3D, compared with lower dimensions.

#### 4.2.3 High frequency correction

We end this section on a technical note, concerning the frequency cutoff. We mentioned that numerically, the Matsubara frequency sums must be truncated; to ensure that this has a minimal impact on the results, in the actual calculations we have added and subtracted the 'noninteracting' pair susceptibility in the following manner:

$$\begin{aligned} \Sigma(\vec{k}, i\omega_m) = & -\frac{|U|^2}{\beta N} \sum_{\vec{q}, n} \left[ \frac{\chi_{00}(\vec{q}, i\nu_n)}{1 - |U|\chi_{00}(\vec{q}, i\nu_n)} - \chi_{00}(\vec{q}, i\nu_n) \right] G^0(-\vec{k} + \vec{q}, -i\omega_m + i\nu_n) \\ & - \frac{|U|^2}{\beta N} \sum_{\vec{q}, n} \chi_{00}(\vec{q}, i\nu_n) G^0(-\vec{k} + \vec{q}, -i\omega_m + i\nu_n). \quad (4.18) \end{aligned}$$

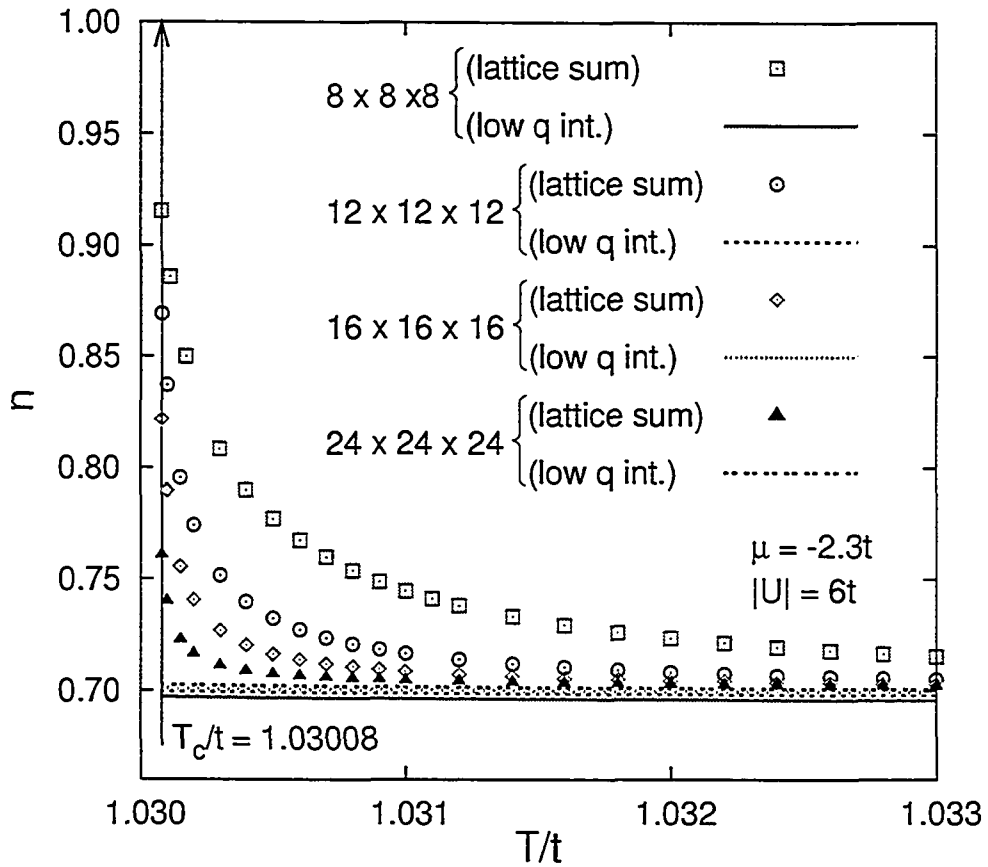


Figure 4.6: 3D - Electronic density vs. temperature, with and without the low  $q$  analytical integration. Note that there is very little size dependence of the results computed with the low  $q$  correction; also, with this technique there is no remaining singularity in the electron density at the Thouless temperature (see Eq. (4.17)), while the singularity is clearly visible in the results computed just using lattice sums.

The first term in Eq. (4.18) converges much more quickly at infinity now, and a straightforward truncation will work well; the small  $\bar{q}$  treatment remains qualitatively the same, since no potential singularities exist in the noninteracting susceptibility. The Matsubara sum in the second term can be done analytically, with the following result:

$$\Sigma_{\text{corr}}(\bar{k}, i\omega_m) = \frac{|U|^2}{N^2} \sum_{\bar{k}', \bar{q}} \frac{\left[1 - f(\xi_{\bar{k}'} - \xi_{-\bar{k}'+\bar{q}})\right] f(\xi_{-\bar{k}+\bar{q}}) + f(\xi_{\bar{k}'})f(\xi_{-\bar{k}'+\bar{q}})}{i\omega_m - \xi_{\bar{k}'} - \xi_{-\bar{k}'+\bar{q}} + \xi_{-\bar{k}+\bar{q}}}, \quad (4.19)$$

where  $\Sigma_{\text{corr}}$  refers to the second line of Eq. (4.18).

### 4.3 Real axis calculations

The Matsubara formalism is very convenient and easy to use. Imaginary axis calculations provide thermodynamic quantities such the density, energy and specific heat, and we showed them ‘at work’ in the last section. However, in order to study spectral properties of the interacting many-body system one needs to extrapolate to the real frequency axis, and this must be done carefully. For example, in Eq. (4.2) the analytic continuation of  $\chi_{00}(\bar{q}, i\nu_n)$  to the complex plane is achieved trivially by the substitution  $i\nu_n \rightarrow z$ , where  $z$  can be anywhere in the complex plane, including just above the real axis:  $z = \omega + i\delta$ . However, in Eq. (4.3) it would be incorrect to replace  $i\omega_m$  by  $z$  before the Matsubara sum over  $i\nu_n$  is done.

#### 4.3.1 Continued fraction approach

One way to approach the problem is to notice that the pair propagator

$$\chi(\bar{q}, z) = \frac{\chi_{00}(\bar{q}, z)}{1 - |U|\chi_{00}(\bar{q}, z)} = \frac{-\frac{1}{N} \sum_{\bar{k}} \frac{1 - f(\xi_{\bar{k}}) - f(\xi_{-\bar{k}+\bar{q}})}{z - \xi_{\bar{k}} - \xi_{-\bar{k}+\bar{q}}}}{1 + |U| \frac{1}{N} \sum_{\bar{k}} \frac{1 - f(\xi_{\bar{k}}) - f(\xi_{-\bar{k}+\bar{q}})}{z - \xi_{\bar{k}} - \xi_{-\bar{k}+\bar{q}}}} \quad (4.20)$$

admits a partial fraction decomposition, which can be written as:

$$\chi(\bar{q}, z) = -\frac{\text{sgn}\left(E_{\bar{q}}^{(1)}\right) R_{\bar{q}}^{(1)}}{z - E_{\bar{q}}^{(1)}} - \frac{\text{sgn}\left(E_{\bar{q}}^{(2)}\right) R_{\bar{q}}^{(2)}}{z - E_{\bar{q}}^{(2)}} - \dots - \frac{\text{sgn}\left(E_{\bar{q}}^{(s_{\bar{q}})}\right) R_{\bar{q}}^{(s_{\bar{q}})}}{z - E_{\bar{q}}^{(s_{\bar{q}})}}, \quad (4.21)$$

where  $s_{\vec{q}}$  denotes the number of poles for each  $\vec{q}$ , the energies  $E_{\vec{q}}^{(\ell)}$  are real and the residues  $R_{\vec{q}}^{(\ell)}$  are strictly positive, for  $\ell = 1, \dots, s_{\vec{q}}$ . Substituting the above expansion into Eq. (4.3) and completing the Matsubara frequency sum analytically allows us to write the following analytic continuation for the self-energy:

$$\Sigma(\vec{k}, z) = \frac{|U|^2}{N} \sum_{\vec{q}} \sum_{\ell=1}^{s_{\vec{q}}} \frac{\text{sgn}(E_{\vec{q}}^{(\ell)}) R_{\vec{q}}^{(\ell)} [N(E_{\vec{q}}^{(\ell)} - \mu) + f(\xi_{-\vec{k}+\vec{q}})]}{z + \xi_{-\vec{k}+\vec{q}} - (E_{\vec{q}}^{(\ell)} - \mu)}. \quad (4.22)$$

(We note that strictly speaking, one should use different notations for the functions in Eqs. (4.21), (4.22) than for their imaginary axis counterparts; we kept the same notations for simplicity.) As elsewhere in this thesis,  $N(x) \equiv 1/(e^{\beta x} - 1)$  and  $f(x) \equiv 1/(e^{\beta x} + 1)$  are the Bose and Fermi distribution functions, respectively. The self-energy in Eq. (4.22) requires the determination of the poles and residues of the partial fraction decomposition of the pair propagator. This approach was used in Ref. [84], together with a computer algebra system allowing for a symbolic calculation that produces numerical results for the poles and residues [70, 86].

### 4.3.2 Kramers-Kronig technique

We outline below a different approach, which will exploit the fact that the real and imaginary parts of the self-energy are related through a Kramers-Kronig integral. Using the spectral representation for the pair propagator

$$\chi(\vec{q}, z) = \int_{-\infty}^{\infty} \frac{B(\vec{q}, \nu)}{z - \nu} d\nu \quad (4.23)$$

in the expression for self-energy, Eq. (4.22), enables us to perform the Matsubara sum analytically. Then the analytic continuation is achieved by the substitution  $i\omega_m \rightarrow z$ , with the following result:

$$\Sigma(\vec{k}, z) = -\frac{|U|^2}{N} \sum_{\vec{q}} \int_{-\infty}^{\infty} \frac{B(\vec{q}, \nu) [N(\nu) + f(\xi_{-\vec{k}+\vec{q}})]}{z - \nu + \xi_{-\vec{k}+\vec{q}}} d\nu. \quad (4.24)$$

In the above equations, we have used the following definition for the spectral function associated to the pair propagator:

$$B(\vec{q}, \nu) \equiv -\frac{1}{\pi} \text{Im} \chi(\vec{q}, \nu + i\delta). \quad (4.25)$$

Eq. (4.24) can provide the self-energy just above the real frequency axis,  $z = \omega + i\delta$  ( $\delta \rightarrow 0^+$ ). However, the frequency integral on top of the momentum sum of a complex integrand is difficult to tackle computationally. The matter simplifies considerably if we separate the imaginary part and make use of the relation

$$\frac{1}{\omega + i\delta} \equiv \mathcal{P} \frac{1}{\omega} - i\pi\delta(\omega), \quad \delta \rightarrow 0^+, \quad (4.26)$$

where  $\mathcal{P}$  denotes the principal part. Thus the imaginary part of Eq. (4.24) at  $z = \omega + i\delta$  involves a  $\delta$ -function, which enables us to perform the frequency integral right away:

$$\begin{aligned} \Sigma_2(\vec{k}, \omega + i\delta) &= \pi \frac{|U|^2}{N} \sum_{\vec{q}} \int_{-\infty}^{\infty} B(\vec{q}, \nu) \left[ N(\nu) + f(\xi_{-\vec{k}+\vec{q}}) \right] \delta(\omega - \nu + \xi_{-\vec{k}+\vec{q}}) d\nu \\ &= \pi \frac{|U|^2}{N} \sum_{\vec{q}} B(\vec{q}, \omega + \xi_{-\vec{k}+\vec{q}}) \left[ N(\omega + \xi_{-\vec{k}+\vec{q}}) + f(\xi_{-\vec{k}+\vec{q}}) \right], \end{aligned} \quad (4.27)$$

where we have used the definition  $\Sigma \equiv \Sigma_1 + i\Sigma_2$ .

In order to calculate  $\Sigma_2$ , we need the spectral function  $B(\vec{q}, \nu)$ . According to Eq.(4.25), it works out to be

$$B(\vec{q}, \nu) = -\frac{\chi_{00,2}(\vec{q}, \nu + i\delta)}{[1 - |U|\chi_{00,1}(\vec{q}, \nu + i\delta)]^2 + |U|^2\chi_{00,2}^2(\vec{q}, \nu + i\delta)}. \quad (4.28)$$

$\chi_{00,1}$  and  $\chi_{00,2}$  denote the real and imaginary part of the noninteracting pair propagator:  $\chi_{00} = \chi_{00,1} + i\chi_{00,2}$ . They are obtained by substituting  $i\nu_n \rightarrow z \rightarrow \nu + i\delta$  in Eq. (4.2) and using Eq. (4.26):

$$\begin{aligned} \chi_{00,2}(\vec{q}, \nu + i\delta) &= \frac{\pi}{N} \sum_{\vec{k}} \left[ 1 - f(\xi_{\vec{k}}) - f(\xi_{-\vec{k}+\vec{q}}) \right] \delta(\nu - \xi_{\vec{k}} - \xi_{-\vec{k}+\vec{q}}), \\ \chi_{00,1}(\vec{q}, \nu + i\delta) &= -\frac{1}{N} \sum_{\vec{k}} \mathcal{P} \frac{1 - f(\xi_{\vec{k}}) - f(\xi_{-\vec{k}+\vec{q}})}{\nu - \xi_{\vec{k}} - \xi_{-\vec{k}+\vec{q}}} \end{aligned} \quad (4.29)$$

We now have all the ‘ingredients’ needed to calculate  $\Sigma_2$ . Once the imaginary part is calculated, the real part of the self-energy is obtained through a Kramers-Kronig integral:

$$\Sigma_1(\vec{k}, \omega + i\delta) = -\frac{1}{\pi} \int_{-\infty}^{\infty} \mathcal{P} \frac{\Sigma_2(\vec{k}, \omega' + i\delta)}{\omega - \omega'} d\omega'. \quad (4.30)$$

The spectral function is then calculated from:

$$\begin{aligned}
A(\vec{k}, \omega) &\equiv -\frac{1}{\pi} \text{Im} \left[ G(\vec{k}, \omega + i\delta) \right] \\
&= -\frac{1}{\pi} \frac{\Sigma_2(\vec{k}, \omega + i\delta)}{\left[ \omega - \xi_{\vec{k}} - \Sigma_1(\vec{k}, \omega + i\delta) \right]^2 + \Sigma_2^2(\vec{k}, \omega + i\delta)}. \quad (4.31)
\end{aligned}$$

The Density Of States (DOS) is given by

$$\mathcal{N}(\omega) = \frac{1}{N} \sum_{\vec{k}} A(\vec{k}, \omega) \quad (4.32)$$

### 4.3.3 Numerical treatment - finite size and broadening effects

Like the computations on the imaginary axis, the numerical treatment of the equations in §4.3.2 has to take into account finite size effects. Unfortunately, the low  $\vec{q}$  treatment described in §4.2.2 is complicated by the fact that  $\chi_{00}$  is now a complex, continuous function of frequency, so a low frequency expansion is needed as well. No longer do we have the possibility of separating the zero frequency term in a discrete sum. That prevents us from being able to integrate the low momentum region analytically, and a regular lattice sum will include the  $\vec{q} = 0, z = 0$  divergence in the pair propagator, leading to a diverging self-energy. The smaller the size of the lattice, the more weight (equal to  $1/N$ ) the divergent term will have in the sum.

There is a simple solution to by-pass the diverging term. In the thermodynamic limit, the sum becomes a momentum integral over the FBZ. The regular sum over the FBZ of a hyper-cubic lattice is in fact numerically equivalent to the trapezoidal rule for performing the momentum integral. However, numerically this integral would be called ‘improper’, because it has an integrable singularity at the lower limit (at  $\vec{q} = 0$ ). To perform such an integral, the evaluation of the integrand at endpoints should be avoided, and this is done by using the *mid-point rule* [85]. In our case, we evaluate the integrand *half-way* between points in the FBZ. This way we avoid the divergent contribution at  $\vec{q} = 0$  and the self-energy will remain finite. Evidently, this leads to incorrect results in one and two dimensions, where the NSC T-matrix self-energy *should* diverge. This is because in 1D and 2D the integral

is not ‘improper’, it is infinite (the  $\vec{q} = 0$  singularity is not integrable, as was illustrated in §4.2). Trying to find a numerical treatment for such an integral would be an ill-posed problem. For this reason, the NSC T-matrix approximation is not appropriate for the 1D and 2D cases. Thus we will only apply it to the 3D case, and use the mid-point trapezoidal method to calculate a self-energy that remains finite.

Another numerical difficulty is related to  $\delta \rightarrow 0^+$ . The importance of this parameter is that it places the quantities of interest in the complex plane above, but infinitesimally close to the real axis. Numerically,  $\delta$  can be small but is by necessity a finite quantity, and its value may affect the outcome of the numerical calculation. We address this issue by progressively decreasing our numerical  $\delta$  and looking at the effect on the resulting density of states.

Finally, similarly to the imaginary axis calculations, a frequency cut-off is needed for the numerical treatment of the Kramers-Kronig integral, Eq. (4.30). Also, we will make the integrand more quickly convergent around the  $\omega = \omega'$  singularity by adding and subtracting a term:

$$\begin{aligned} \Sigma_1(\vec{k}, \omega + i\delta) &= \frac{1}{\pi} \int_{-\infty}^{\infty} \mathcal{P} \left[ \frac{\Sigma_2(\vec{k}, \omega + i\delta) - \Sigma_2(\vec{k}, \omega' + i\delta)}{\omega - \omega'} \right] d\omega' \\ &\quad - \Sigma_2(\vec{k}, \omega + i\delta) \frac{1}{\pi} \int_{-\infty}^{\infty} \mathcal{P} \frac{d\omega'}{\omega - \omega'} \end{aligned} \quad (4.33)$$

The term on second line of Eq. (4.33) turns out to be zero, which is easily seen after making a change of variables  $y = \omega' - \omega$  and noticing that the integrand is an odd function of  $y$ . Thus, the real part of the self-energy is given by the term on the first line of Eq. (4.33).

#### 4.3.4 3D density of states - results

We have calculated the 3D DOS for a range of coupling strengths, using the mid-point trapezoidal rule for the momentum integration. DOS results on a  $16 \times 16 \times 16$  lattice for two values of the coupling strength, corresponding to strong and weak coupling, respectively, are shown in Fig. 4.7, for a numerical broadening of  $\delta = 0.01t$ . Partly due to the interest in the cuprate superconductors and doped Mott insulators, and also for convenience, we have examined a noninteracting density of  $\langle n \rangle_0 = 1$ , *viz.* half-filling. Also, DOS results for the same parameters, obtained through a partial fraction decomposition algorithm, are available for comparison in Ref. [84]. Fig. 4.7(a)

shows results for the stronger coupling  $|U| = 6t$ . Each DOS curve presents peak structures that become sharper as the temperature is lowered towards  $T_c$ . It is natural to associate the location of these peaks with something analogous to the superconducting gap. Of course, the NSC T-Matrix approximation is a normal state theory, and the DOS does not ever go to zero (at  $\omega/t = 0$ ), so the locations of the peaks are not true superconducting gaps. Instead, we think of the peak locations as indicating the energy of a *pseudogap*. Perhaps not surprisingly, a robust pseudogap is found for the strong coupling case. However, as illustrated in Fig. 4.7(b), a similar analysis for  $|U| = 3t$  finds evidence for a pseudogap (albeit much weaker) persisting to lower couplings.

As a function of temperature, the pseudogap does not change appreciatively for small reduced temperature ( $[T - T_c]/T_c$  less than 0.1). At sufficiently high temperatures the gap disappears, and we find that it does so by filling in, as opposed to the pseudogap energy going to zero.

We note that the pseudogap we find does not diverge as the temperature is lowered very close to  $T_c$ . In addition, Fig. 4.8 shows that for two different lattice sizes the pseudogap does not change. These two facts are an indication that the mid-point trapezoidal  $\bar{q}$  integration leads to results that are a good approximation to the thermodynamic limit. We contrast this finding to Ref. [84], where a  $1/N^2$  scaling is used to extrapolate the pseudogap results, displaying strong finite size effects, to the thermodynamic limit. Our pseudogap values correlate well with the extrapolated results of Ref. [84], for both strong and weak coupling. Furthermore, one can use BCS theory to calculate the superconducting gap at  $T = 0$ . Fig. 4.9(c) compares the pseudogap, as obtained from the DOS peak positions for different coupling constants going from weak to strong coupling (shown on panels (a,b) of the same figure), with the BCS superconducting gap  $\Delta_{BCS}(0)$ . Remarkably, the lower coupling pseudogap follows the BCS results very closely for a range of coupling strengths, before crossing over to a higher energy scale at strong coupling, roughly three times larger than the BCS gap energy. The reason for the large difference in the strong coupling limit is unclear to us at present.

The purpose of Fig. 4.10 is to justify the value of the broadening parameter  $\delta$  we have chosen for our DOS results. We mentioned that a finite value of  $\delta$  may affect the outcome of the calculations. While this is confirmed for values of  $\delta/t$  greater than 0.01, for  $\delta/t$  below this value we find that results become noisier, but the position of the peaks in the DOS does not change. Thus we trust that the energy of the pseudogap that we find using a numer-



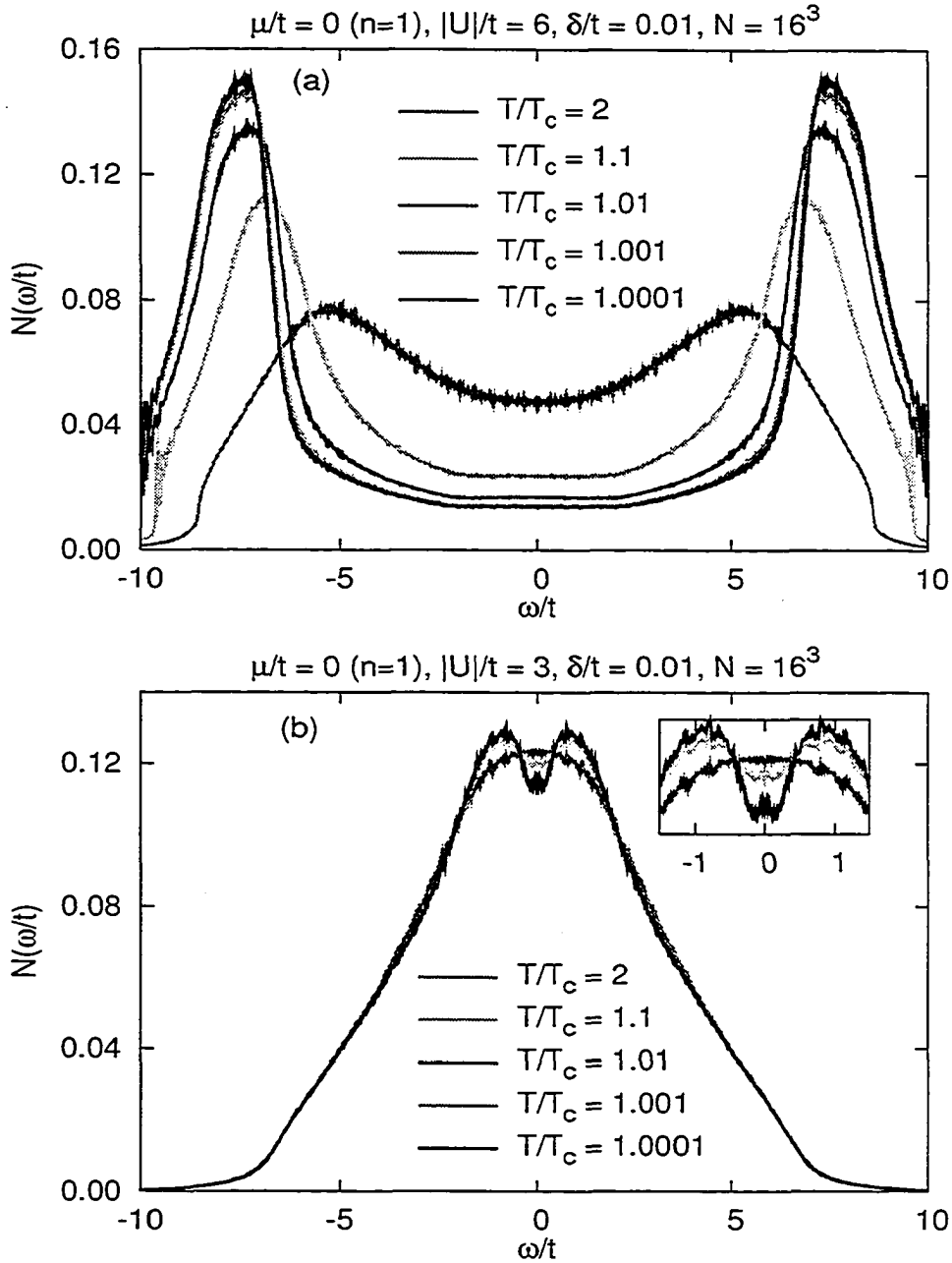


Figure 4.7: DOS (Eq. (4.32)) for (a)  $|U|/t = 6$  and (b)  $|U|/t = 3$  at half-filling, for a  $16^3$  simple cubic lattice, at different temperatures above (and moving towards)  $T_c$ . Note the peak structures in the DOS curves, indicative of a pseudogap that fills in at higher temperatures.

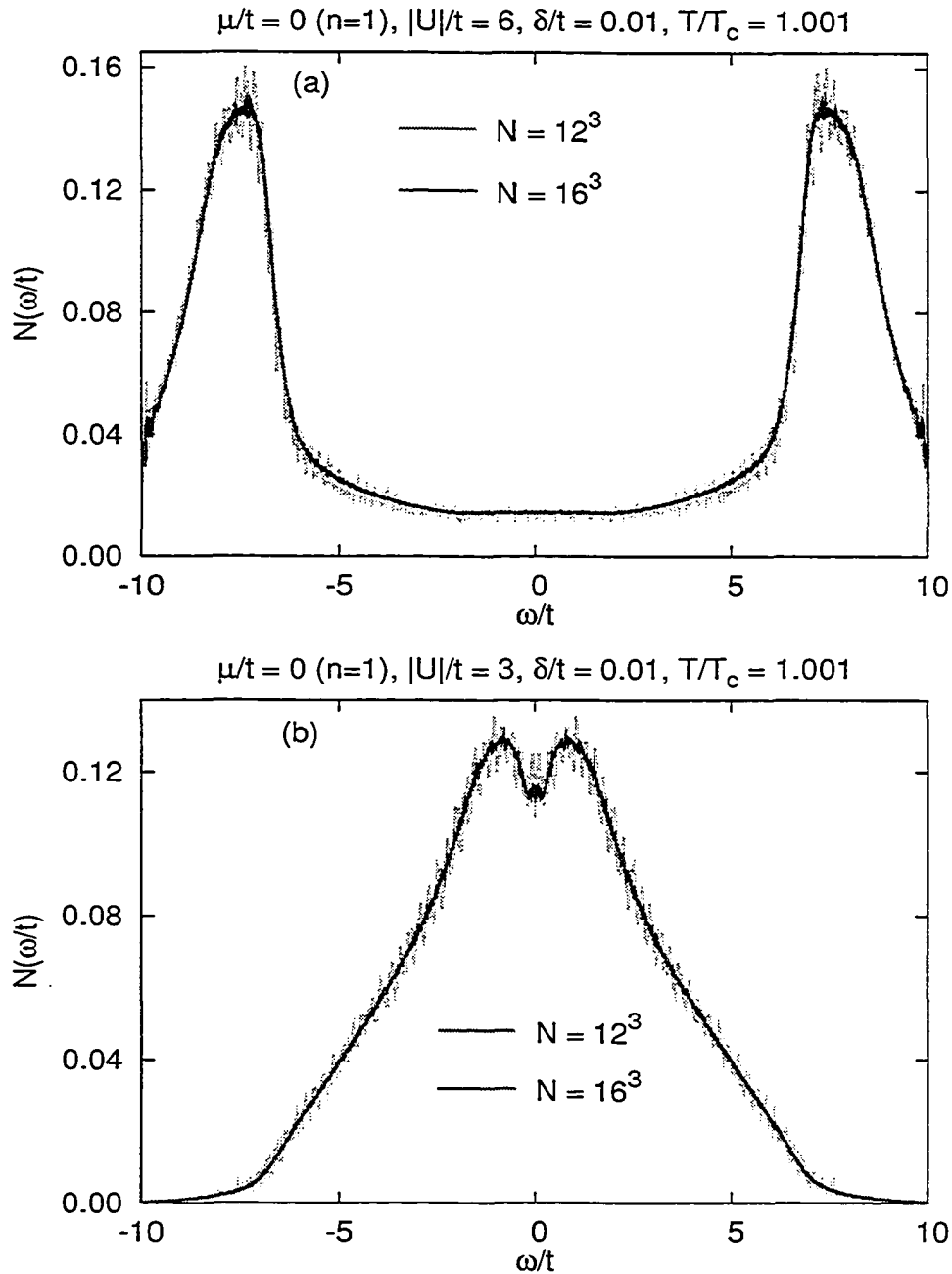


Figure 4.8: DOS (Eq. (4.32)) for (a)  $|U|/t = 6$  and (b)  $|U|/t = 3$  at half-filling, near  $T_c$ , for two different lattice sizes. Note that the position of the peaks does not change with the size of the lattice.

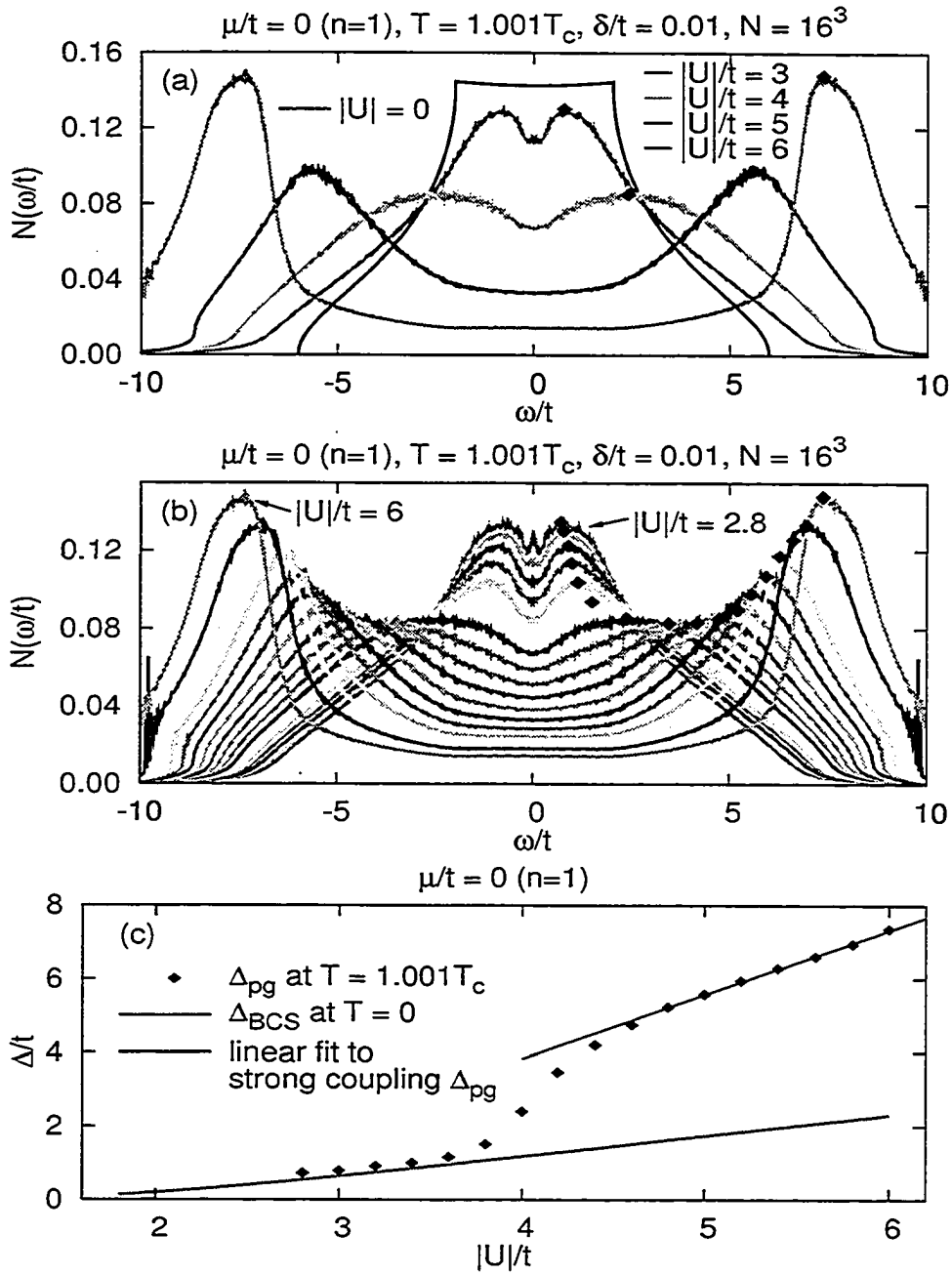


Figure 4.9: (a,b) DOS (Eq. (4.32)) for different coupling strengths at a temperature of  $1.001T_c$ , for a  $16^3$  simple cubic lattice at half-filling. The  $|U|/t$  increment in (b) is 0.2; the peak position is indicated for each coupling strength. (c) Comparison of the pseudogap with the BCS SC gap at  $T = 0$ .

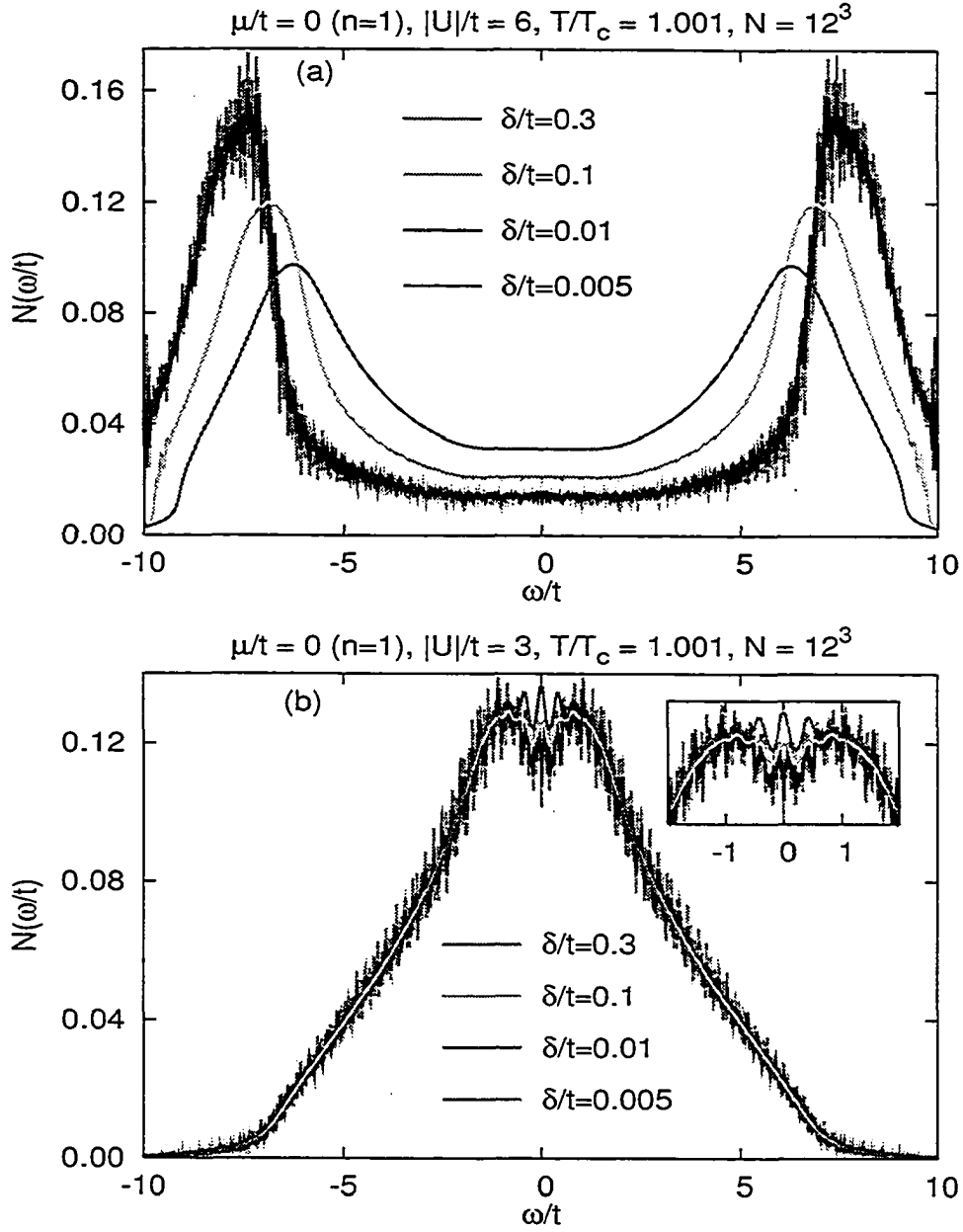


Figure 4.10: DOS (Eq. (4.32)) for (a)  $|U|/t = 6$  and (b)  $|U|/t = 3$  for a  $12^3$  lattice at half-filling, near  $T_c$ , for different values of the broadening parameter  $\delta$ . Note that while the position of the peaks changes with  $\delta$  above  $\delta/t = 0.01$ , it stays the same for  $\delta/t$  less than this value (results for  $\delta/t = 0.002$ , not shown, confirm this finding).

ical broadening of 0.01 (in units of  $t$ ) is indeed correct, and not an artifact of the chosen  $\delta$ .

The existence of a pseudogap in a model of a three-dimensional strongly correlated electronic system agrees with earlier (three-dimensional) work by Levin and coworkers [72]. However, they propose that the pseudogap they find can be understood in terms of a T-matrix resonance caused by intermediate to large  $|U|$ , whereas we are finding the full value of the BCS gap above  $T_c$  even for weak coupling.

## 4.4 2D case - self-consistent treatment

The two dimensional case is of special interest, because the physics of the HTSC materials is essentially two-dimensional. We advocate the view that the anomalous normal state in the cuprates, *i.e.* the pseudogap phase, may be the result of pairing fluctuations above  $T_c$ . The simplest way to incorporate pairing correlations into single particle properties is the NSC T-matrix approximation, used in the previous section for 3D calculations. While capable of producing a well-defined pseudogap at low temperatures reminiscent of experiment [87], this approximation fails in two dimensions for reasons amply discussed in §2.5 and illustrated in the atomic limit in chapter 3.

The main conclusion of the atomic limit work is that self-consistency does indeed correct the anomalies of the NSC T-matrix theory. In that context, a minimal formulation of the self-consistent T-matrix theory seemed to work best, especially in the low-temperature, low-density regimes. In fact, it proved to be *exact* at  $T = 0$ , and followed very closely the exact results for an extended temperature range above zero.

In this section we will use that minimally self-consistent version of the T-matrix approximation to solve for the attractive Hubbard model in two dimensions. Specifically, we will be searching whether or not this formulation produces a ‘normal state gap’ in the single particle spectrum.

### 4.4.1 The approximation

We will include feedback effects into the T-matrix through the use of one full propagator in the ‘bare’ pair susceptibility:

$$\chi_0(\vec{q}, i\nu_n) = \frac{1}{\beta N} \sum_{\vec{k}, l} G(\vec{k}, i\omega_l) G^0(-\vec{k} + \vec{q}, -i\omega_l + i\nu_n). \quad (4.34)$$

The self-energy is given by

$$\begin{aligned}\Sigma(\vec{k}, i\omega_m) &= -\frac{|U|^2}{\beta N} \sum_{\vec{q}, n} \chi(\vec{q}, i\nu_n) G^0(-\vec{k} + \vec{q}, -i\omega_m + i\nu_n) \\ &= -\frac{|U|^2}{\beta N} \sum_{\vec{q}, n} \frac{\chi_0(\vec{q}, i\nu_n)}{1 - |U|\chi_0(\vec{q}, i\nu_n)} G^0(-\vec{k} + \vec{q}, -i\omega_m + i\nu_n).\end{aligned}\quad (4.35)$$

This self-energy ‘dresses’ the one-particle propagator via Dyson’s equation, Eq. (2.36), which closes the self-consistency loop.

The calculations we have done in the atomic limit, as well as previous work on higher dimensions [72, 75], have shown that any degree of self-consistency drives the superconducting instability to zero temperature. We illustrate this property once again in Fig. 4.11, by comparing the 2D electron density obtained through a self-consistent calculation with the NSC density we calculated in §4.2.2, both with and without the low  $\vec{q}$  refinement discussed there. While the NSC density goes abruptly to one as the Thouless temperature is approached, indicating a diverging self-energy, the self-consistent result continues on smoothly, demonstrating the absence of a Thouless region. Once this has been established, one can look for a pseudogap signature in the single-particle properties in the normal state, above  $T = 0$ .

#### 4.4.2 2D density of states

As Eqs. (4.31), (4.32) show, calculating the DOS requires the one-particle Green function on the real axis. Within the Matsubara formalism we calculate  $G(\vec{k}, i\omega_m)$  from its self-energy via Dyson’s equation, Eq. (2.36). Baym and Mermin [88] have proved that it is possible, in principle, to analytically continue the temperature Green function to the whole complex plane, provided that we know its value at an infinite set of points on the imaginary axis. Supposing that the analytical continuation can be found, we merely evaluate it along the real axis, setting  $z = \omega + i0^+$ . In practice, however, any numerical treatment provides the value of  $\Sigma(\vec{k}, i\omega_m)$  (and thus  $G$ ) at a *finite* set of points. Moreover, the theorem of Baym and Mermin only shows the existence and uniqueness of the analytical continuation, but there is no general prescription to find it, hence the need to resort to approximate techniques.

A widely used technique is the Padé approximant method, in which a continued fractions decomposition of the function to be extrapolated to the

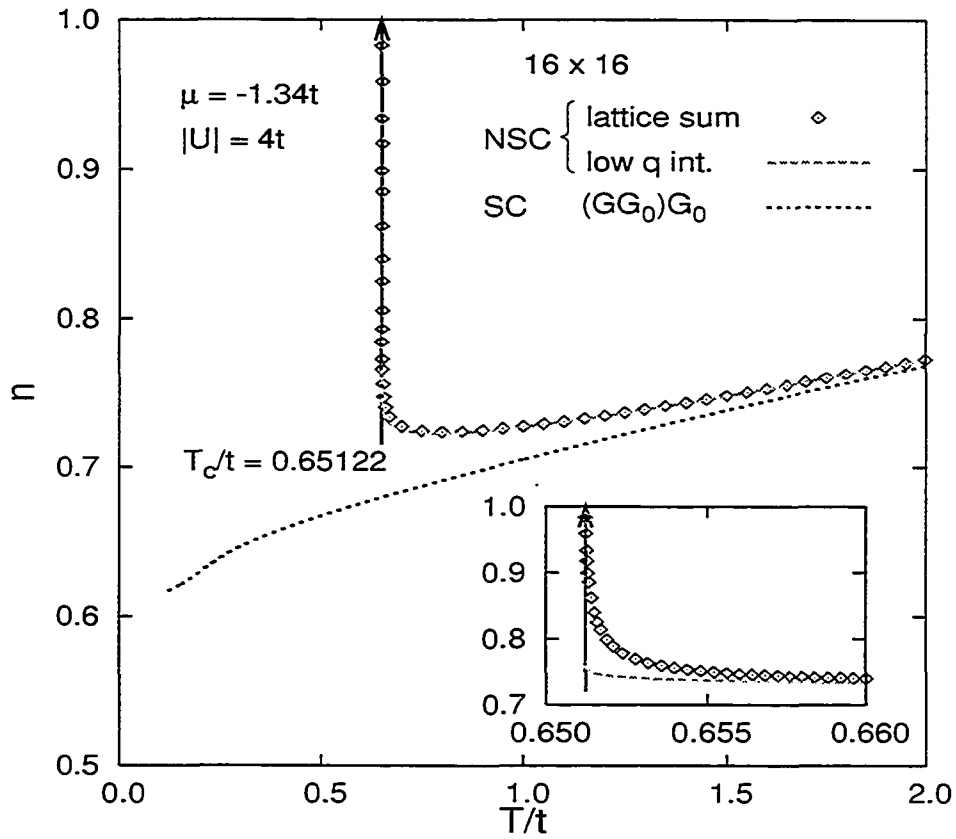


Figure 4.11: 2D - Electronic density vs. temperature and for a  $16 \times 16$  lattice. Note the absence of a Thouless region in the self-consistent calculation (see Eqs. (4.34), (4.35)). The inset focuses on the region near the Thouless temperature, emphasizing once again the weaker (logarithmic) singularity when the low  $\bar{q}$  contribution is handled analytically (see §4.2.2 for discussion).

real axis (see an example for the NSC pair propagator in §4.3.1) is artificially terminated. Numerically, this procedure is equivalent to fitting the function of interest by ratios of polynomials. The most common scheme, a recursive algorithm called Thiele's Reciprocal Difference Method, is presented in Appendix B. This approximation was used by Vidberg and Serene [89] in the context of the Eliashberg equations.

The main concern with this technique is the high degree of accuracy it requires for the values on the imaginary axis of the function to be fitted, which puts a difficult strain on computer resources, especially when self-consistent calculations are involved. This prevented us from obtaining results for very low temperatures, where we felt that the output function could not be trusted to produce meaningful results. Fortunately, as we will see next, enhanced fluctuations in two dimensions come into effect well above the  $T = 0$  instability, making the access of the very low temperature regime not a necessity. This also alleviates our concern about finite size effects, expected to become important close to the pairing instability, but less of a factor away from it.

Next, we present DOS results obtained for the AHM on a 2D square lattice, solved with the SC T-matrix approximation presented in §4.4.1. We have obtained results for interaction parameters ranging from weak to strong coupling. Peak structures in the DOS curves indicate that a pseudogap is present in the single particle DOS, even for smaller values of the coupling strength. As Figs. 4.12 and 4.13 show, the pseudogap opens at higher temperatures, the stronger the coupling. For a given  $|U|/t$  value, the peak energy changes little with temperature for an extended temperature range. As the temperature is raised further, the pseudogap itself seems to fill in rather than close (*i.e.*, its energy going to zero). This behavior is similar to that of the 3D NSC pseudogap we found in §4.3.4. An important difference, compared to the 3D case, is the fact that in two dimensions a pseudogap is present at temperatures well above the critical temperature  $T_c = 0$ . This is not a surprise, however, since enhanced fluctuations towards the low-temperature phase are expected, the lower the dimensionality of the system.

Like in three dimensions, one can use BCS theory to calculate the superconducting gap at  $T = 0$ . Fig. 4.14(b) shows that in the lower coupling regime the pseudogap energy is very close to the BCS ( $T=0$ ) gap energy, while in the strong coupling regime the pseudogap energy is much larger. This is similar to what we have found in the 3D case. At the moment we don't understand the significance of the large difference in the strong cou-



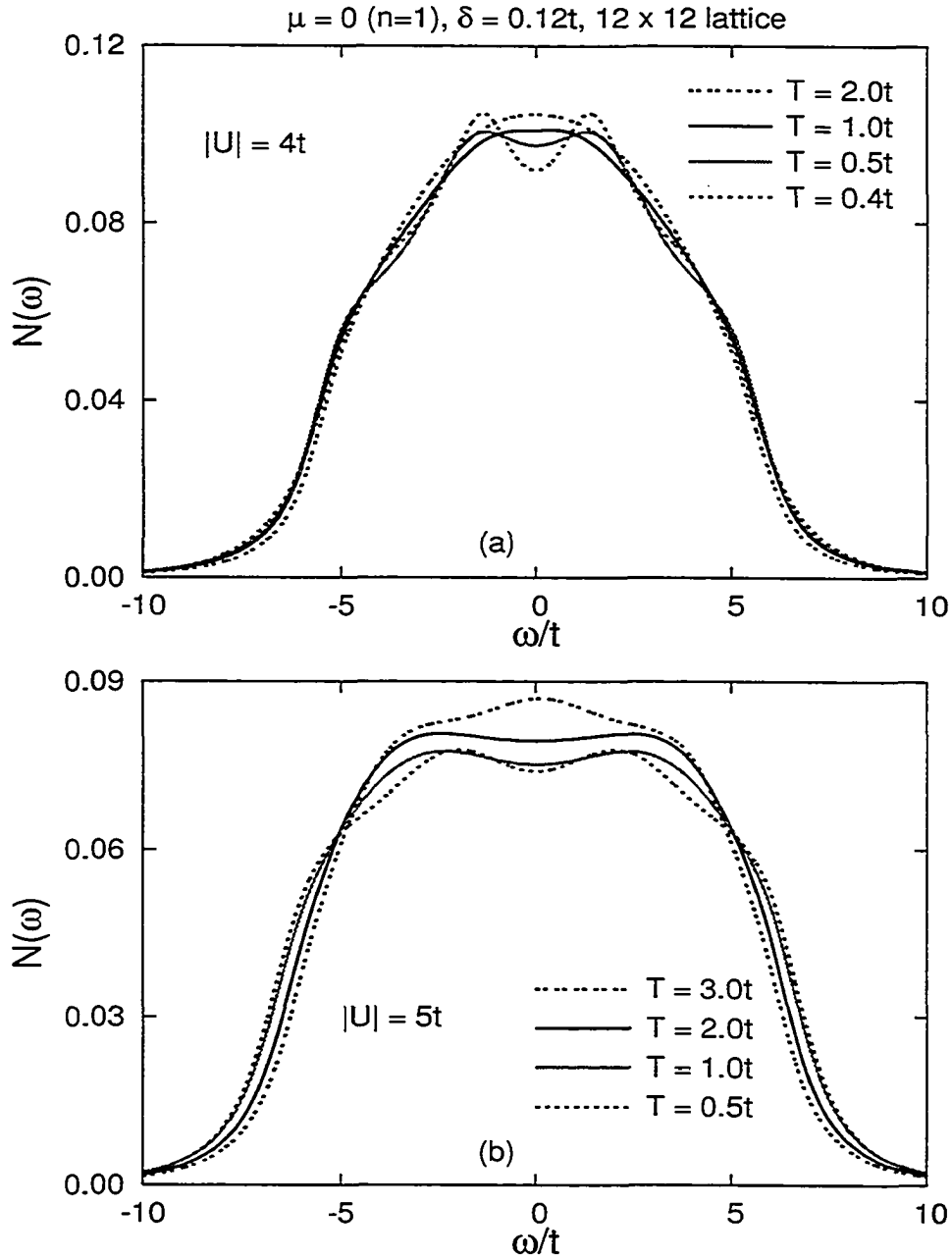


Figure 4.12: 2D - DOS (Eq. (4.32)) for (a)  $|U|/t = 4$  and (b)  $|U|/t = 5$  for a  $12 \times 12$  lattice at half-filling, from a self-consistent calculation (see Eqs. (4.34), (4.35)). We have used a broadening of 3% of the noninteracting bandwidth, namely  $0.12t$ .

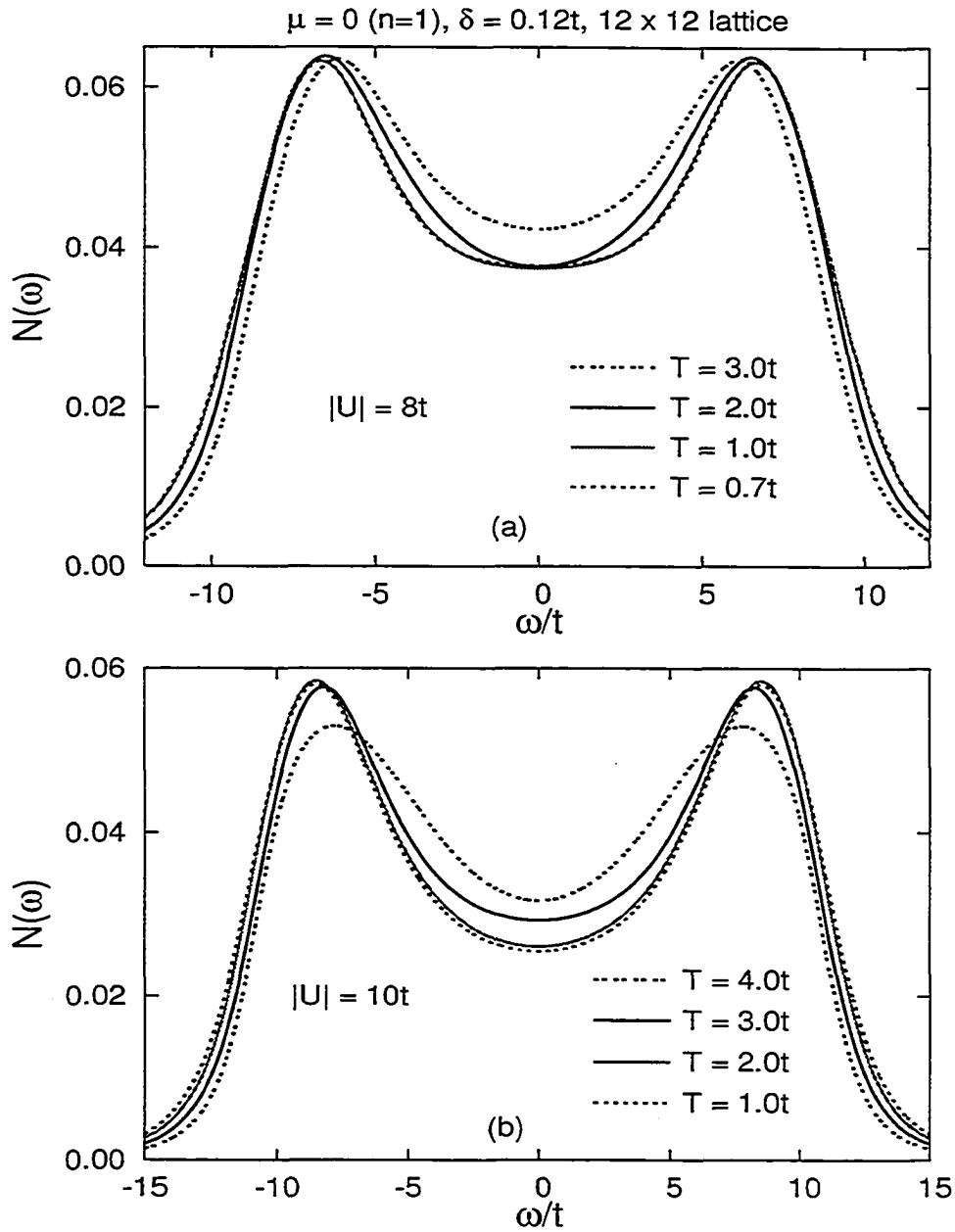


Figure 4.13: 2D - DOS (Eq. (4.32)) for (a)  $|U|/t = 8$  and (b)  $|U|/t = 10$  for a  $12 \times 12$  lattice at half-filling, from a self-consistent calculation (see Eqs. (4.34), (4.35)). We have used a broadening of 3% of the noninteracting bandwidth, namely  $0.12t$ . Note the presence of a pseudogap at larger temperature as the coupling is increased.

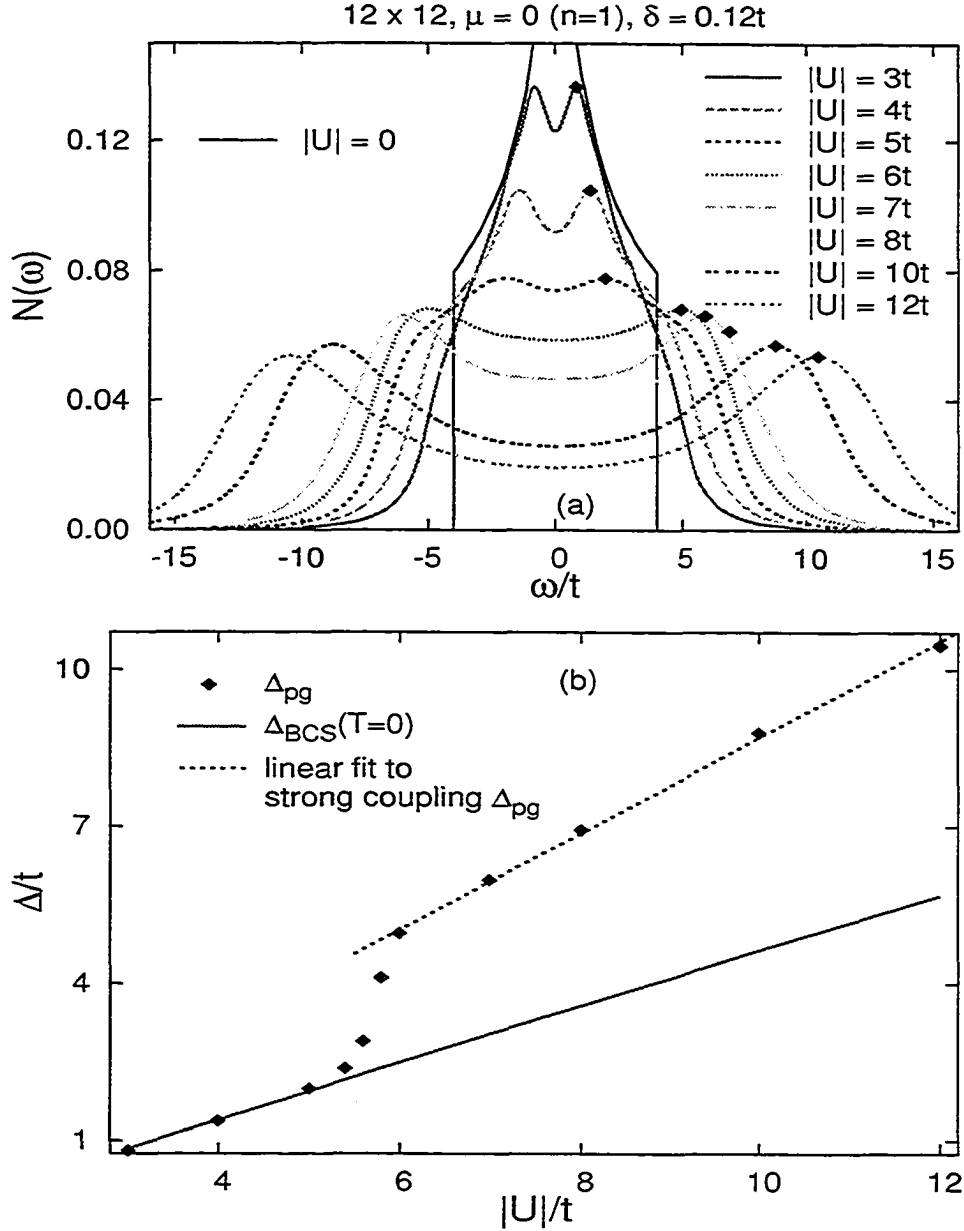


Figure 4.14: 2D - (a) DOS (Eq. (4.32)) for different coupling strengths, for a  $12 \times 12$  simple cubic lattice at half-filling; the peak position is indicated for each coupling strength. The temperature for  $|U|/t = 3$  and  $|U|/t = 4$  is  $0.4t$ , for  $|U|/t = 5$  and  $|U|/t = 6$  it is  $0.5t$ , and for all the other coupling values it is  $0.7t$ . (b) Comparison of the pseudogap with the BCS SC gap at  $T = 0$ .

pling limit; we can only speculate that strong coupling effects, not accounted for in the BCS theory, set a larger energy scale in the superconducting state, sensed by the pseudogap on the normal side of the transition.

## 4.5 Summary

In this chapter, we have extended the study of the T-matrix approximation we have done in the atomic limit (0-dimensions) in Chapter 3 to higher dimensions. In its simplest form, the non-self-consistent version, this approximation correctly predicts a true phase transition at a nonzero temperature in three dimensions. We find that the NSC T-matrix approximation leads to a pseudogap in the single-particle density of states in the normal phase, even when the attraction is weak. Moreover, the energy of the 'normal state gap' is comparable to the  $T = 0$  BCS superconducting gap energy in the weak coupling limit; for larger coupling parameters we find a pseudogap energy that is much larger than the  $T = 0$  BCS gap energy.

As the analysis in §4.2 demonstrated, the nature of the problem changes with dimensionality, and the NSC T-matrix theory prediction of a finite temperature pairing instability leads to anomalies in lower dimensions. The inclusion of feedback effects on the Thouless criterion drives the superconducting instability to zero temperature, in agreement with the Mermin-Wagner theorem. In two dimensions, within a minimally self-consistent treatment, a pseudogap is present in the single particle DOS over an extended temperature range above the  $T_c = 0$  superconducting transition. Similarly to the 3D case, the lower coupling pseudogap energy is comparable to the  $T = 0$  BCS gap energy, while the strong coupling pseudogap exceeds it significantly. The reason for the large difference in the strong coupling limit eludes us at present. We speculate that there might be strong coupling corrections that lead to such large gap values (in the superconducting state). Then it would be natural that the pseudogap senses this larger energy scale, in the same way it does for the BCS gap in the weak coupling regime.

# Chapter 5

## Conclusion

### 5.1 Summary of the T-matrix Approximation

This thesis has explored the effect of pairing correlations above the superconducting transition, for a system of lattice fermions provided with an attractive isotropic interaction. We have used the T-matrix approximation, a diagrammatic scheme presented in Chapter 2, designed to include two-particle correlation effects into single particle properties. The discussion in §2.5, as well as our work on the atomic (strong coupling) limit in Chapter 3, have demonstrated the importance of returning feedback to the two-particle properties, once the single particle quantities have been renormalized. This is particularly stringent when the available phase space is small, where neglecting such feedback effects can lead to certain pathologies.

For lower dimensionality, self-consistency is required to correct the unphysical behavior rooted in the NSC prediction of a finite temperature instability. A finite temperature phase transition is prohibited by the Mermin Wagner theorem. The Schmitt-Rink, Varma and Ruckenstein (SVR) treatment [69], improved by Serene [78], allows the system to adjust itself to avoid the instability. However, in doing so it leads to the destruction of the Fermi surface, in violation of Luttinger's theorem, which requires that the Fermi volume be conserved.

The way in which self-consistency is enforced is equally important. While any degree of self-consistency will drive  $T_c$  (as calculated from the Thouless criterion) to zero, certain self-consistent formulations may have problems connecting smoothly with the BCS theory, which, in the low-coupling limit at

least, is the appropriate theory when approaching  $T_c$  from the superconducting side. It has been shown [70] that any self-consistent scheme where the full propagator is used to close the self-energy (see the last line in Eq. (2.35) and Fig. 2.3(b)), leads to gapless superconductivity at  $T_c$ .

We have done an extensive analysis of different self-consistent versions of the T-matrix theory in the atomic limit in Chapter 3. We were motivated by the fact in this limit an exact solution is available, enabling us to discriminate between different candidate theories. We have also included in our analysis an alternate scheme, the TPSC approach of Vilk-Tremblay [29]. There, one of the ‘bare’ vertices  $|U|$  is replaced by a frequency-independent irreducible vertex  $|U_{pp}|$ , accompanied by propagators that contain a simple Hartree-like renormalization. The TPSC approximation, together with a minimally self-consistent formulation of the T-matrix approximation, promoted in particular by the Levin group [72], proved to be ‘front-runners’, when compared with the exact solution. Both theories appear to be exact at  $T = 0$ , and analytical work has demonstrated that this is indeed the case. However, analysis of the dynamics in the two approaches clearly favor the T-matrix formulation, which remains remarkably accurate over a broader temperature range above zero, at least for low electron densities. A greater degree of self-consistency does not translate in improved results. In fact, the contrary is true, the renormalization of more than one propagator in the pairing susceptibility deteriorates the agreement. This finding supports suggestions [65, 90] that at low temperatures some cancellation occurs between the fully self-consistent T-matrix diagrams and vertex corrections, omitted in all standard T-matrix approximations. The significance of this cancellation eludes us at present.

In three dimensions, the non-self-consistent version of the T-matrix approximation seems to suffice. As formulated in the original work by Thouless [63], the divergence of the NSC pairing susceptibility at  $T_c$  - the NSC Thouless criterion - reproduces precisely the BCS result for the transition temperature. Our three dimensional study in Chapter 4 demonstrates that this approximation is capable of producing a pseudogap in the normal state density of states, even for low coupling. Moreover, in the same low coupling regime the energy of the pseudogap agrees very well with the  $T = 0$  BCS gap. In this case a self-consistent treatment is not deemed necessary, although we do expect feedback effects to reinforce the NSC result.

For the two-dimensional case, we have enforced minimal self-consistency, as suggested by the atomic limit work. We find a pseudogap in the single

particle DOS over an extended temperature range above the  $T_c = 0$  superconducting transition. Similarly to the 3D case, the lower coupling pseudogap energy is comparable to the  $T = 0$  BCS gap energy. Both in two and three dimensions, the energy of the strong coupling pseudogap exceeds the BCS gap energy significantly. Currently, we don't fully understand the reason for the large difference in the strong coupling limit. We can only make the tentative assertion that one should look for an answer in the superconducting state, where strong coupling corrections beyond BCS theory may lead to a much larger energy scale for the superconducting gap. It would follow naturally that the pseudogap senses this larger energy scale, in the same way it does for the BCS gap in the weak coupling regime. We note, however, that exact strong coupling theory (atomic limit), as well as strong coupling BCS theory, gives  $\Delta = |U|/2$  at half filling, and our results are well above this value, particularly in 3D.

## 5.2 Relevance to High $T_c$ Superconductors

We have shown that pairing fluctuations above  $T_c$  are indeed capable of producing a pseudogap in the normal state DOS. This result has general validity, since the model used throughout the thesis, the AHM, does not assume any particular pairing mechanism. It is true that for a complete description of High  $T_c$  superconductivity in its full complexity one must have a microscopic theory that, among other things, gives the correct symmetry of the order parameter and takes into account magnetic correlations. The latter are expected to become increasingly important as decreasing doping brings the metal-insulator transition nearer. Nevertheless, we believe that the conclusions of our work are relevant to the high  $T_c$  systems independent of microscopic details.

Most of the research on the subject associates the pseudogap phenomenon with the lower dimensionality of the cuprates; indeed, for these materials, it is clear that quasi two dimensionality will enhance critical fluctuations, and therefore reinforce the pseudogap effects. However, we find a pseudogap in three dimensions, even for low  $|U|$ . In previous 3D work [72] this effect is seen as a result of intermediate to large coupling. This would place stronger constraints on the mechanism leading to superconductivity in HTSC. As our work demonstrates, independently of the underlying mechanism and intensity of coupling, pairing correlations contribute to the pseudogap. Whether they

are the sole contributor or only a factor of the entire pseudogap scenario remains to be established. Magnetic correlations or other effects may, also, ultimately play a role, especially in the extreme underdoped regime. In any case, it is clear that the role of pairing correlations must be calibrated in order to fully understand the physics of the cuprate superconductors.



# Bibliography

- [1] J. G. Bednorz and K. A. Müller, *Z. Phys. B* **64**, 189 (1986).
- [2] J. Bardeen, L.N. Cooper and J.R. Schrieffer, *Phys. Rev.* **106**, 162 (1957); *Phys. Rev.* **108**, 1175 (1957).
- [3] M. K. Wu, J. R. Ashburn, C. J. Torng, P. H. Hor, R. L. Meng, L. Goa, Z. J. Huang, Y. Q. Wang and C. W. Chu, *Phys. Rev. Lett.* **58**, 908 (1987).
- [4] See the 11 May 1987 issue of *Time* magazine.
- [5] P. J. White, Z.-X. Shen, C. Kim, J. M. Harris, A. G. Loeser, P. Fournier and A. Kapitulnik, *Phys. Rev. B* **54**, R15669 (1996).
- [6] J. M. Harris, Z.-X. Shen, P. J. White, D. S. Marshall, M. C. Schabel, J. N. Eckstein and I. Bozovic, *Phys. Rev. B* **54**, R15665 (1996).
- [7] T. Timusk and B. Statt, *Rep. Prog. Phys.* **62**, 61 (1999).
- [8] W. W. Warren, R. E. Walstedt, J. F. Brennert, R. J. Cava, R. Tycko, R. F. Bell and G. Dabbagh, *Phys. Rev. Lett.* **62**, 1193 (1989).
- [9] J. W. Loram, K. A. Mirza, J. R. Cooper, W. Y. Liang and J. M. Wade, *Physica C* **282-287**, 1405 (1997).
- [10] B. Bucher, P. Steiner, J. Karpinski, E. Kaldis and P. Watcher, *Phys. Rev. Lett.* **70**, 2012 (1993).
- [11] K. Krishana, N. P. Ong, Q. Li, G. D. Gu and N. Koshizuka, *Science* **277**, 83 (1997).
- [12] N. P. Ong, *Physica C* **135-140**, 2191 (1994).

- [13] D. N. Basov, R. Liang, B. Dabrowski, D. A. Bonn, W N Hardy and T. Timusk, *Phys. Rev. Lett.* **77**, 4090 (1996).
- [14] C. Renner, B. Revaz, J.-Y. Genoud, K. Kadowaki and O. Fisher, *Phys. Rev. Lett.* **80**, 149 (1998); C. Renner, B. Revaz, K. Kadowaki, I. Maggio-Aprile and O. Fisher, *Phys. Rev. Lett.* **80**, 3606 (1998).
- [15] A. G. Loeser, Z.-X. Shen, D. S. Dessau, D. S. Marshall, C. H. Park, P. Fournier and A. Kapitulnik, *Science* **273**, 325 (1996).
- [16] H. Ding, T. Yokoya, J. C. Campuzano, T. Takahashi, M. Randeria, M. R. Norman, T. Mochiku, K. Kadowaki and J. Giapintzakis, *Nature* **382**, 51 (1996).
- [17] A. Damascelli, Z.-X. Shen and Z. Hussein, *Rev. Mod. Phys.* **75**, 453 (2003)
- [18] J. C. Campuzano, M. R. Norman and M. Randeria, in *Physics of Superconductors*, edited by K. H. Bennemann and J. B. Ketterson (Springer, Berlin, 2004) p. 167-273.
- [19] M. Randeria and J. C. Campuzano, eprint cond-mat/9709107 (1997).
- [20] C. C. Homes, T. Timusk, R. Liang, D. A. Bonn, W N Hardy and *Phys. Rev. Lett.* **71**, 1645 (1993).
- [21] K. McElroy, D.-H. Lee, J. E. Hoffman, K. M. Lang, J. Orenstein, J. Lee, E. W. Hudson, H. Eisaki, S. Uchida and J. C. Davis, *Phys. Rev. Lett* **94**, 197005 (2005); K. McElroy, R. W. Simmonds, J. E. Hoffman, D.-H. Lee, J. Orenstein, H. Eisaki, S. Uchida and J. C. Davis, *Nature* **422**, 592 (2003).
- [22] M. R. Norman and C. Pépin, *Rep. Prog. Phys.* **66**, 1547 (2003).
- [23] A.J. Leggett, *J. de Physique, C7*, **41**, 19 (1980);  
A.J. Leggett, in *Modern Trends in the Theory of Condensed Matter*, edited by S. Pekalski and J. Przystawa (Springer, Berlin, 1980) p. 13.
- [24] V. J. Emery and S. A. Kivelson, *Nature* **374**, 434 (1995).
- [25] P. W. Anderson, *Science* **235**, 1196 (1987).

- [26] E. Lieb, F. Y. Wu, *Phys. Rev. Lett.* **20**, 1445 (1968).
- [27] J. M. Tranquada, B. J. Sternlieb, J. D. Axe, Y. Nakamura and S. Uchida, *Nature* **375**, 561 (1995).
- [28] A. V. Chubukov, D. Pines and J. Schmalian, in *Physics of Superconductors*, edited by K. H. Bennemann and J. B. Ketterson (Springer, Berlin, 2004) p. 495-590; A. Abanov, A. V. Chubukov and J. Schmalian, *Adv. Phys.* **52**, 119 (2003).
- [29] Y. M. Vilk and A.-M. S. Tremblay, *J. de Physique I (France)* **7**, 1309 (1997) and references therein.
- [30] B. Kyung, V. Hankevych, A.-M. Daré and A.-M. S. Tremblay, *Phys. Rev. Lett.* **93**, 147004 (2004).
- [31] R. B. Laughlin, *Adv. Phys.* **47**, 943 (1998).
- [32] S. Sachdev, *Science* **288**, 475 (2000).
- [33] J. L. Tallon and J. W. Loram, *Physica C* **349**, 53 (2001).
- [34] A. Kaminski, S. Rosenkranz, H. M. Fretwell, J. C. Campuzano, Z. Li, H. Raffy, W. G. Cullen, H. You, C. G. Olsen, C. M. Varma, and H. Höchst, *Nature* **416**, 610 (2002).
- [35] C. M. Varma, *Phys. Rev. Lett.* **83**, 3538 (1999); M. E. Simon and C. M. Varma, *Phys. Rev. Lett.* **89**, 247003 (2002).
- [36] S. Chakravarty, R. B. Laughlin, D. K. Morr and C. Nayak, *Phys. Rev. B* **63**, 094503 (2001).
- [37] D. M. Eagles, *Phys. Rev.* **186**, 456 (1969).
- [38] J. Ranninger and J. M. Robin, *Phys. Rev. B* **53**, R11961 (1996).
- [39] V. Geshkenbein, L. Ioffe and A. Larkin, *Phys. Rev. B* **55**, 3173 (1997).
- [40] L. N. Cooper, *Phys. Rev.* **104**, 1189 (1956).
- [41] H. Frölich, *Phys. Rev.* **79**, 845 (1950).

- [42] A. B. Migdal, Zh. Eksper. Teor. Fiz. **34**, 1438 (1958) [Soviet Phys. JETP **7**, 996 (1958)].
- [43] G.M. Eliashberg, Zh. Eksper. Teor. Fiz. **38**, 966 (1960) [Soviet Phys. JETP **11**, 696 (1960)].
- [44] A. Lanzara, P. V. Bogdanov, X. J. Zhou, S. A. Kellar, D. L. Feng, E. D. Lu, T. Yoshida, H. Eisaki, A. Fujimori, K. Kishio, J.-I. Shimoyama, T. Noda, S. Uchida, Z. Hussain, and Z.-X. Shen, Nature **412** 510 (2001).
- [45] S. Verga, A. Knigavko and F. Marsiglio, Phys. Rev. B **67**, 054503 (2003).
- [46] P. B. Allen and B. Mitrović, in *Solid State Physics*, edited by H. Ehrenreich, F. Seitz and D. Turnbull (Academic, New York, 1982) Vol. **37**, p. 1.
- [47] , F. Marsiglio and J. P. Carbotte, in *The Physics of Conventional and Unconventional Superconductors*, edited by K. H. Bennemann and J. B. Ketterson (Springer-Verlag, 2003), p. 233.
- [48] V. J. Emery, Phys. Rev. Lett. **58**, 2794 (1987).
- [49] C. M. Varma, S. Schmitt-Rink and E. Abrahams, in *Novel Mechanisms of Superconductivity*, edited by S. A. Wolf and V. Z. Kresin (Plenum Press, solid New York, 1987), p. 355; Solid State Commun. **62**, 681 (1987).
- [50] F. C. Zhang and T. M. Rice, Phys. Rev. B **37**, 3759 1988.
- [51] E. Dagotto, Rev. Mod. Phys. **66**, 763 (1994).
- [52] M. Y. Kagan and T. M. Rice, J. Phys. Cond. Matt. **6**, 3771 (1994).
- [53] J. M. Luttinger, Phys. Rev. **119**, 1153 (1960).
- [54] C. Sá de Melo, M. Randeria and J. R. Engelbrecht, Phys. Rev. Lett. **71**, 3202 (1993).
- [55] J. R. Engelbrecht, M. Randeria and C. Sá de Melo, Phys. Rev. B **55**, 15153 (1997).

- [56] M. Randeria, in *Bose-Einstein Condensation*, edited by A. Griffin, D. W. Snoke and S. Stringari (Cambridge University Press, New York, 1995), p. 355.
- [57] A. Moreo, D. J. Scalapino and S. R. White, *Phys. Rev. B* **45**, 7544 (1992); M. Randeria, N. Trivedi, A. Moreo and R. T. Scalettar, *Phys. Rev. Lett.* **69**, 2001 (1992); N. Trivedi and M. Randeria, *Phys. Rev. Lett.* **75**, 312 (1995); N. Trivedi and M. Randeria, *J. of Superconductivity* **9**, 13 (1996); J. M. Singer, M. H. Pedersen, T. Schneider, H. Beck and H.-G. Matuttis, *Phys. Rev. B* **54**, 1286 (1996); J. M. Singer, T. Schneider and M. H. Pedersen, *Eur. Phys. J. B* **2**, 17 (1998); J. M. Singer, T. Schneider and P. F. Meier, *Eur. Phys. J. B* **7**, 37 (1999); S. Allen, H. Touchette, S. Moukouri, Y. M. Vilks and A.-M. S. Tremblay, *Phys. Rev. Lett.* **83**, 4128 (1999).
- [58] A. Sewer, X. Zotos and H. Beck, *Phys. Rev. B.* **66**, 140504R (2002).
- [59] See for example K. E. Schmidt and M. H. Kalos in *Monte Carlo Methods in Statistical Physics II*, edited by K. Binder (Springer 1984).
- [60] Alexander L. Fetter and John Dirk Walecka, *Quantum Theory of Many-Particle Systems* (McGraw-Hill, New York, 1971).
- [61] P. Pieri and G. C. Strinati, *Phys. Rev. B* **61**, 15370 (2000).
- [62] D. S. Petrov, C. Salomon and G. V. Shlyapnikov, *Phys. Rev. Lett.* **93**, 090404 (2004).
- [63] D.J. Thouless, *Ann. Phys.* **10**, 553 (1960).
- [64] P. Nozières and S. Schmitt-Rink, *J. Low Temp. Phys.* **59**, 195 (1985).
- [65] L. P. Kadanoff and P. C. Martin, *Phys. Rev* **124**, 670
- [66] G. Baym and L.P. Kadanoff, *Phys. Rev.* **124**, 287 (1961).
- [67] P. B. Allen, in *Modern Trends in the Theory of Condensed Matter, Proceedings, Karpacz, 1979*, edited by A. Pekalski and J. Przystawa (Springer Verlag, New York, 1980), p. 388.
- [68] V. Ambegaokar, in *Superconductivity*, edited by R. D. Parks (Marcel Dekker, New York, 1969), Vol. 1, p. 259.

- [69] S. Schmitt-Rink, C. Varma, and A.E. Ruckenstein, *Phys. Rev. Lett.* **63**, 445 (1989).
- [70] K. S. D. Beach, M.Sc. Thesis (Queen's University) 1999.
- [71] B. R. Patton, *Phys. Rev. Lett.* **27**, 1273 (1971); Ph.D. Thesis (Cornell University) 1970.
- [72] B. Janko, J. Maly, and K. Levin, *Phys. Rev. B* **56**, 11407 (1997); I. Kosztin, Q. Chen, B. Janko, and K. Levin, *Phys. Rev. B* **58**, 5936 (1998). See also Q. Chen, K. Levin, and I. Kosztin, *Phys. Rev. B* **63**, 184519 (2001), and references therein.
- [73] See, for example, N.E. Bickers, in *Theoretical Methods for Strongly Correlated Electrons*, edited by D. Sénéchal, A.-M. Tremblay, and C. Bourbonnais (Springer, Berlin, 2004), p. 235.
- [74] G. Baym, *Phys. Rev.* **127**, 1391 (1962).
- [75] K. S. D. Beach, R.J. Gooding, and F. Marsiglio, *Phys. Lett. A* **282**, 319 (2001).
- [76] S. Allen and A.-M. S. Tremblay, *Phys. Rev. B* **64**, 075115 (2001); B. Kyung, S. Allen and A.-M. S. Tremblay, *Phys. Rev. B* **64**, 075116 (2001).
- [77] N. D. Mermin, H. Wagner, *Phys. Rev. Lett.* **17**, 1133 (1966); P. C. Hohenberg, *Phys. Rev.* **158**, 383 (1967); S. Coleman, *Comm. Math. Phys.* **31**, 259 (1973).
- [78] J. Serene, *Phys. Rev. B* **40**, 10873 (1989).
- [79] A. Tokumitsu, K. Miyake and K. Yamada, *Phys. Rev. B* **47**, 11988 (1993).
- [80] V. Zlatić, B. Horvatić, B. Dolički, S. Gabowski, P. Entel and K.-D. Schotte, *Phys. Rev. B* **63**, 035104 (2000).
- [81] S. Allen, A.-M.S. Tremblay, and Y.M. Vil'k, in *Theoretical Methods for Strongly Correlated Electrons*, edited by D. Sénéchal, A.-M. Tremblay, and C. Bourbonnais, Springer, 2004, p. 341.
- [82] V. L. Berezinski, *Zh. Eksper. Teor. Fiz.* **59**, 907 (1970) [*Soviet Phys. JETP* **32**, 493 (1970)]; J. Kosterlitz and D. Thouless, *J. Phys. C* **6**, 1181 (1973).

- [83] J. Corson, R. Mallozzi, J. Orenstein, J. N. Eckstein and I. Bozović, *Nature* **398**, 221 (1999).
- [84] R. J. Gooding, F. Marsiglio, S. Verga and K. S. D. Beach, *J. Low Temp. Phys.* **136**, 191 (2004).
- [85] W. H. Press, B. P. Flannery, S. A. Teukolsky and W. T. Vetterling, *Numerical Recipes* (Cambridge University Press, Cambridge, 1986), p. 115.
- [86] K. S. D. Beach, R.J. Gooding, and F. Marsiglio, *Phys. Rev. B* **61**, 5147 (2000).
- [87] K. S. D. Beach, R.J. Gooding, and F. Marsiglio, *Physica C* **341-348**, 897 (2000).
- [88] G. Baym and D. Mermin, *J. Math. Phys.* **2**, 232 (1961).
- [89] H. J. Vidberg and J. Serene, *J. Low Temp. Phys.* **29**, 179 (1977).
- [90] A. Klein, *Nuovo Cimento* **25**, 788 (1962).
- [91] J.R. Schrieffer, *Theory of Superconductivity* (Benjamin/Cummings, Don Mills, 1964).
- [92] F. Marsiglio, unpublished.
- [93] B. Mitrović, H. G. Zarate and J. P. Carbotte, *Phys. Rev. B* **29**, 184 (1984).

# Appendix A

## Results in the noninteracting limit

### A.1 The noninteracting Hamiltonian

When the on-site interaction in the AHM is set to zero, the surviving part, the kinetic term, describes a collection of free electrons on a lattice:

$$\hat{H}_0 = -t \sum_{\langle ij \rangle, \sigma} (\hat{c}_{i\sigma}^\dagger \hat{c}_{j\sigma} + h.c.). \quad (\text{A.1})$$

Assuming periodic boundary conditions, the AHM given by Eq. (1.1) is symmetric under translation by a Bravais lattice vector. This translational symmetry allows the use of the Bloch momentum as a good quantum number to label eigenstates of the AHM Hamiltonian. Introducing the Bloch operator  $c_{\vec{k},\alpha}^-$  we have:

$$c_{j,\alpha} = \frac{1}{\sqrt{N}} \sum_{\vec{k}} e^{i\vec{k} \cdot \vec{R}_j} c_{\vec{k},\alpha}^-, \quad (\text{A.2})$$

$$c_{\vec{k},\alpha}^- = \frac{1}{\sqrt{N}} \sum_j e^{-i\vec{k} \cdot \vec{R}_j} c_{j,\alpha}, \quad (\text{A.3})$$

where  $\vec{R}_j$  is the Bravais lattice vector corresponding to site  $j$  and  $\vec{k}$  labels the Bloch vectors in the First Brillouin Zone (FBZ):



$$\vec{k} = (k_1, k_2, \dots, k_D) = \left( \frac{\pi n_1}{La}, \frac{\pi n_2}{La}, \dots, \frac{\pi n_D}{La} \right),$$

$$n_{1,2,\dots,D} = -L + 1, -L + 2, \dots, -1, 0, 1, \dots, L - 1, L \quad (\text{A.4})$$

for a  $D$ -dimensional hypercubic lattice with  $M = 2L$  sites on each axis ( $N = M^D$ ) and lattice constant  $a$ . The noninteracting Hamiltonian is diagonal in momentum representation:

$$\hat{H}_0 = \sum_{\vec{k}, \alpha} (\epsilon_{\vec{k}} - \mu) c_{\vec{k}, \alpha}^\dagger c_{\vec{k}, \alpha}, \quad (\text{A.5})$$

where  $\epsilon_{\vec{k}}$  is the single particle dispersion and  $\mu$  is the chemical potential.

## A.2 The noninteracting one-particle Green function

In this section, for illustrative purposes, we will take the EOM formalism described in §2.3.2 to Fourier space, in order to derive an expression for the noninteracting one-particle Green function.

According to Eq. (2.2), the noninteracting one-particle Green function is defined as the ensemble average of the following time ordered product of Heisenberg annihilation and creation operators:

$$G_\alpha^0(1; 1') = -\langle T_\tau [c_\alpha^0(1) c_\alpha^{\dagger 0}(1')] \rangle_0 \equiv -\frac{1}{Z_G} \text{Tr} \left\{ e^{-\beta \hat{K}_0} T_\tau [c_\alpha^0(1) c_\alpha^{\dagger 0}(1')] \right\}, \quad (\text{A.6})$$

where  $Z_G \equiv e^{-\beta \Omega_0} \equiv \text{Tr} \left\{ e^{-\beta \hat{K}_0} \right\}$  is the partition function in the grand canonical ensemble. The operators  $c_\alpha^0(m)$ ,  $c_\alpha^{\dagger 0}(m)$  are the noninteracting equivalent of those given by Eq. (2.1):

$$\begin{aligned} c_\alpha^0(m) &= e^{-\hat{K}_0 \tau_m} c_{j_m \alpha} e^{\hat{K}_0 \tau_m} \\ c_\alpha^{\dagger 0}(m) &= e^{-\hat{K}_0 \tau_m} c_{j_m \alpha}^\dagger e^{\hat{K}_0 \tau_m}, \end{aligned} \quad (\text{A.7})$$

The difference comes from the use of the noninteracting grand canonical Hamiltonian  $\hat{K}_0 = \hat{H}_0 - \mu \hat{N}$ , where  $\hat{H}_0$  is given by Eq. (A.1). Substituting Eq. (A.2) into Eq. (A.6) for the one-particle propagator (making note of the spin symmetry of the AHM, we will drop the spin indices to simplify the notation):

$$\begin{aligned}
G^0(1; 1') &= -\langle T_\tau [c_{j_1}^0(\tau_1) c_{j_1'}^{\dagger 0}(\tau_1')] \rangle_0 \\
&= -\left\langle T_\tau \left[ \left( \frac{1}{\sqrt{N}} \sum_{\vec{k}} e^{i\vec{k} \cdot \vec{R}_{j_1}} c_{\vec{k}}^0(\tau_1) \right) \left( \frac{1}{\sqrt{N}} \sum_{\vec{k}'} e^{-i\vec{k}' \cdot \vec{R}_{j_1'}} c_{\vec{k}'}^{\dagger 0}(\tau_1') \right) \right] \right\rangle_0 \\
&= -\frac{1}{N} \sum_{\vec{k}, \vec{k}'} e^{i(\vec{k} \cdot \vec{R}_{j_1} - \vec{k}' \cdot \vec{R}_{j_1'})} \underbrace{\langle T_\tau [c_{\vec{k}}^0(\tau_1) c_{\vec{k}'}^{\dagger 0}(\tau_1')] \rangle_0}_{\propto \delta_{\vec{k}\vec{k}'}} \\
&= -\frac{1}{N} \sum_{\vec{k}} e^{i\vec{k} \cdot (\vec{R}_{j_1} - \vec{R}_{j_1'})} \langle T_\tau [c_{\vec{k}}^0(\tau_1) c_{\vec{k}}^{\dagger 0}(\tau_1')] \rangle_0 \\
&= -\frac{1}{N} \sum_{\vec{k}} e^{i\vec{k} \cdot (\vec{R}_{j_1} - \vec{R}_{j_1'})} G^0(\vec{k}; \tau_1, \tau_1') \tag{A.8}
\end{aligned}$$

As a result of the imaginary time invariance of the AHM one can show, using the cyclic property of the trace, that the one-particle Green function  $G(\vec{k}; \tau, \tau')$  depends on its imaginary time coordinates only through their difference  $\tau - \tau'$ :

$$\begin{aligned}
G^0(\vec{k}; \tau, \tau') &= -\langle T_\tau [c_{\vec{k}}^0(\tau) c_{\vec{k}}^{\dagger 0}(\tau')] \rangle_0 \\
&= -\frac{1}{Z_G} \text{Tr} \left\{ e^{-\beta \hat{K}_0} T_\tau [e^{-\hat{K}_0 \tau} c_{\vec{k}} e^{\hat{K}_0(\tau - \tau')} c_{\vec{k}}^\dagger e^{\hat{K}_0 \tau'}] \right\} \\
&= -\frac{1}{Z_G} \text{Tr} \left\{ e^{-\beta \hat{K}_0} T_\tau [e^{-\hat{K}_0(\tau - \tau')} c_{\vec{k}} e^{\hat{K}_0(\tau - \tau')} c_{\vec{k}}^\dagger] \right\} \\
&= -\frac{1}{Z_G} \text{Tr} \left\{ e^{-\beta \hat{K}_0} T_\tau [c_{\vec{k}}^0(\tau - \tau') c_{\vec{k}}^{\dagger 0}(0)] \right\} \\
&= G^0(\vec{k}; \tau - \tau'). \tag{A.9}
\end{aligned}$$

The property in (A.9), together with the fact that the fermionic Matsubara Green functions are antiperiodic under shifts  $\tau \rightarrow \tau + \beta$  (again, this can be seen easily for  $G^0(\vec{k}; \tau)$  using the cyclic property of the trace) allows one to express the noninteracting Green function in terms of its Fourier component:

$$G^0(\vec{k}; \tau) = \frac{1}{\beta} \sum_n e^{-i\omega_n \tau} G^0(\vec{k}, i\omega_n). \tag{A.10}$$

$$G^0(\vec{k}; i\omega_m) = \int_0^\beta e^{i\omega_m \tau} G^0(\vec{k}, \tau). \tag{A.11}$$

With Eq. (A.10), Eq. (A.8) becomes:

$$G^0(1; 1') \equiv G^0(1-1') = \frac{1}{\beta N} \sum_{\vec{k}} \sum_n e^{i\vec{k} \cdot (\vec{R}_{j_1} - \vec{R}_{j_1'})} e^{-i\omega_n(\tau_{j_1} - \tau_{j_1'})} G^0(\vec{k}, i\omega_n). \quad (\text{A.12})$$

Substituting the above expression into the equation of motion of the free propagator given by Eq. (2.9) leads to

$$\sum_{j''} \left[ t + \left( -\frac{\partial}{\partial \tau_1} + \mu \right) \delta_{j_1 j''} \right] \frac{1}{\beta N} \sum_{\vec{k}} \sum_n e^{i\vec{k} \cdot (\vec{R}_{j''} - \vec{R}_{j_1'})} e^{-i\omega_n(\tau_{j_1} - \tau_{j_1'})} G^0(\vec{k}, i\omega_n) = \delta_{j_1 j_1'} \delta(\tau_1 - \tau_{1'}). \quad (\text{A.13})$$

As noted before, the prime symbol indicates that the sum is restricted to nearest neighbors of  $j_1$  only. The right hand side can be written as:

$$\delta_{j_1 j_1'} \delta(\tau_1 - \tau_{1'}) = \frac{1}{N} \sum_{\vec{k}} e^{i\vec{k} \cdot (\vec{R}_{j_1} - \vec{R}_{j_1'})} \frac{1}{\beta} \sum_n e^{-i\omega_n(\tau_{j_1} - \tau_{j_1'})}. \quad (\text{A.14})$$

After a few algebraic manipulations, the left hand side of Eq. (A.13) gives

$$\begin{aligned} & \frac{1}{\beta N} \sum_{\vec{k}} \sum_n \left[ -\frac{\partial}{\partial \tau_1} + t \left( \sum_{j''} e^{i\vec{k} \cdot (\vec{R}_{j''} - \vec{R}_{j_1})} \right) + \mu \right] e^{i\vec{k} \cdot (\vec{R}_{j_1} - \vec{R}_{j_1'})} e^{-i\omega_n(\tau_{j_1} - \tau_{j_1'})} G^0(\vec{k}, i\omega_n) \\ & = \frac{1}{\beta N} \sum_{\vec{k}} \sum_n (i\omega_n - \epsilon_{\vec{k}} + \mu) e^{i\vec{k} \cdot (\vec{R}_{j_1} - \vec{R}_{j_1'})} e^{-i\omega_n(\tau_{j_1} - \tau_{j_1'})} G^0(\vec{k}, i\omega_n). \end{aligned} \quad (\text{A.15})$$

The free one-particle dispersion, which also appears in Eq. (A.5), is given by

$$\epsilon_{\vec{k}} = t \sum_{j''} e^{i\vec{k} \cdot (\vec{R}_{j''} - \vec{R}_{j_1})} = -2t \sum_{i=1}^D \cos(k_i a) \quad (\text{A.16})$$

for a  $D$ -dimensional hyper-cubic lattice of lattice constant  $a$ .

Finally, putting the left hand side (A.15) and the right hand side (A.14) together we get

$$\begin{aligned} & (i\omega_n - \epsilon_{\vec{k}} + \mu) G^0(\vec{k}, i\omega_n) = 1 \quad \text{or} \\ & G^0(\vec{k}, i\omega_n) \equiv G_1^0(\vec{k}, i\omega_n) = G_1^0(\vec{k}, i\omega_n) = \frac{1}{i\omega_n - \epsilon_{\vec{k}} + \mu}. \end{aligned} \quad (\text{A.17})$$

Like in the more general case, we require the number equation to relate the chemical potential to a particular electron density. In the noninteracting limit, Eq. (2.38) becomes:

$$n_0 = \frac{2}{N\beta} \sum_{\vec{k}, m} G^0(\vec{k}, i\omega_m) e^{i\omega_m 0^+} = \frac{2}{N\beta} \sum_{\vec{k}, m} \frac{e^{i\omega_m 0^+}}{i\omega_m - \epsilon_{\vec{k}} + \mu}. \quad (\text{A.18})$$

The Matsubara sum can be performed analytically and we obtain the usual result,

$$n_0 = \frac{2}{N} \sum_{\mathbf{k}} f(\epsilon_{\mathbf{k}} - \mu) \quad (\text{A.19})$$

with  $f(x) \equiv 1/(e^{\beta x} + 1)$  the Fermi-Dirac distribution function.

### A.3 Pairing susceptibility in the noninteracting approximation

Here we will derive an expression for the noninteracting pair propagator. Later, from the perspective set by Eq. (2.34), we will illustrate how the Cooper instability arises in the presence of interactions.

The pair propagator is a special case of the more general two-particle Green function  $G_{2,\uparrow\downarrow}(12; 1'2')$ . In the noninteracting limit, the latter is obtained from Eq. (2.11) with the correlation function set to zero (this can be seen from Eq. (2.24) and (2.25) when  $|U| = 0$ ). Setting  $2 = 1$  and  $2' = 1'$  leads to the noninteracting pair propagator:

$$G_{2,\uparrow\downarrow}^0(11; 1'1') = G_{\uparrow}^0(1; 1') G_{\downarrow}^0(1; 1'). \quad (\text{A.20})$$

Expressing the two noninteracting one-particle Green functions in the above expression in term of their Fourier components, one has:

$$\begin{aligned} G_{2,\uparrow\downarrow}^0(11; 1'1') &= \sum_{k, k'} e^{i(k+k') \cdot (1-1')} G_{\uparrow}^0(k) G_{\downarrow}^0(k') \\ &= \sum_{k, Q} e^{iQ \cdot (1-1')} G_{\uparrow}^0(k) G_{\downarrow}^0(Q - k) \\ &\equiv \sum_Q e^{iQ \cdot (1-1')} G_{2,\uparrow\downarrow}(Q). \end{aligned} \quad (\text{A.21})$$

In the above relations we have used the compact notations:

$$k \equiv (\vec{k}, i\omega_m), \quad Q \equiv (\vec{q}, i\nu_n),$$

$$\sum_k \equiv \frac{1}{\beta N} \sum_{\vec{k}} \sum_{m=-\infty}^{\infty}, \quad (\text{A.22})$$

$$Q \cdot (1 - 1') \equiv \vec{q} \cdot (\vec{R}_{j_1} - \vec{R}_{j_1'}) - i\nu_n(\tau_1 - \tau_1'),$$

where, like elsewhere in this thesis,  $i\omega_m \equiv i\pi T(2m - 1)$  and  $i\nu_n \equiv i\pi T2n$ ,  $m, n \in \mathbb{Z}$ , are the fermionic and bosonic Matsubara frequencies, respectively. The last two lines in Eq. (A.21) lead to the following expression for the pair propagator in Fourier space:

$$G_{2,\uparrow\downarrow}^0(Q) \equiv \chi_{00}(\vec{q}, i\nu_n) = \frac{1}{N\beta} \sum_{\vec{k}, m} G_{\uparrow}^0(\vec{k}, i\omega_m) G_{\downarrow}^0(-\vec{k} + \vec{q}, -i\omega_m + i\nu_n) \quad (\text{A.23})$$

The Matsubara sum can be readily evaluated, and we get

$$\chi_{00}(\vec{q}, z) = -\frac{1}{N} \sum_{\vec{k}} \frac{1 - f(\epsilon_{\vec{k}} - \mu) - f(\epsilon_{-\vec{k} + \vec{q}} - \mu)}{z - (\epsilon_{\vec{k}} - \mu) - (\epsilon_{-\vec{k} + \vec{q}} - \mu)}, \quad (\text{A.24})$$

Thinking ahead, in Eq. (A.24) we have analytically continued the result to the upper half-plane ( $i\nu_n \rightarrow z$ ). To go further, one needs to perform the  $\vec{k}$ -sum according to the dimensionality and the size of any particular system.

When one deals with a finite size system, the sum over  $\vec{k}$  is discrete, and poles occur at the two particle scattering energies,  $\epsilon_{\vec{k}} + \epsilon_{-\vec{k} + \vec{q}} - 2\mu$ . These plots are often displayed in texts [91, 68]; one example, showing the real part of the susceptibility, is reproduced in Fig. A.1(a) for a 1D system with  $N = 32$  sites. Note that as the temperature decreases, the zero frequency minimum increases in value; we have indicated with a horizontal line a typical value of  $1/|U|$  (with  $|U| = 2t$ ), anticipating the discussion about the Cooper instability problem. The other diverging parts of the curve are principal value parts, the true analytical properties of which will be more properly displayed in the thermodynamic limit (see below). In Fig.A.1(b) we show the imaginary part of the susceptibility as well (obtained by using a finite smearing parameter in place of the infinitesimal  $\delta$ ).

In the thermodynamic limit [92], the picture is quite different. We show in Figs. A.2(a) and A.2(b) the corresponding results for an infinite system

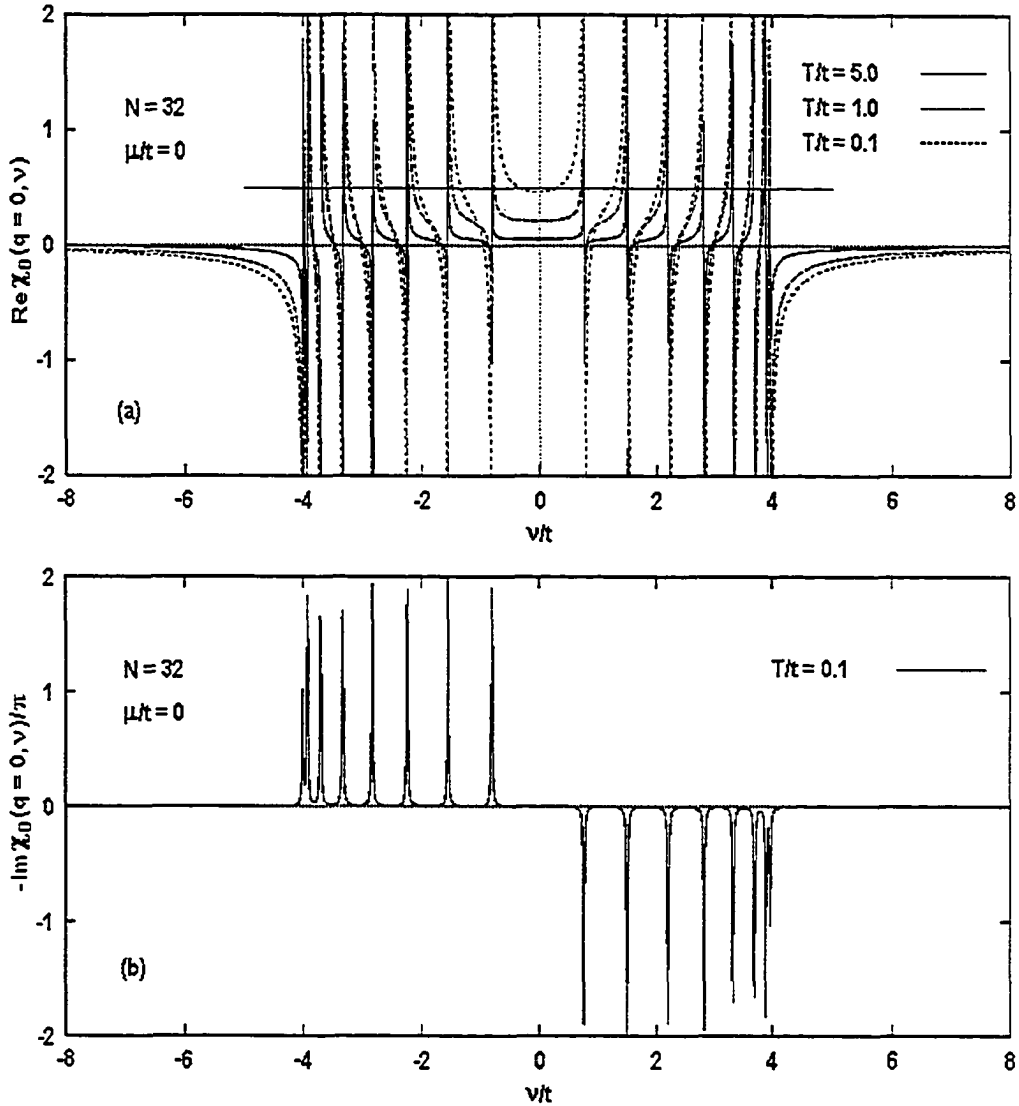


Figure A.1: Real (a) and imaginary (b) parts of the noninteracting susceptibility (Eq. (A.24)) at zero wavevector vs. frequency, for three different temperatures. Note that poles occur at the energies corresponding to two single electron energies. In addition, the minimum at zero frequency diverges as the temperature goes to zero (not evident in (a) because the divergence is logarithmic). The figures were produced in one dimension with a finite lattice of length 32 sites. The horizontal line at 0.5 denotes the value of  $1/|U|$  for  $|U| = 2t$ , for future reference.

(in 1D) at temperatures  $T = 1, 0.1,$  and  $0.01$  (in units of  $t$ ). The real part of  $\chi_0(\vec{q} = 0, \nu)$  clearly shows a *maximum* at zero frequency; elsewhere there are no positive divergences as they have been integrated to a smooth curve in the principal value sense. The negative divergences occur at the band edges and are due to the divergent single electron density of states at the band edges in one dimension. As is apparent from Fig. A.2(a) these divergences are present at all temperatures. In fact, for the lowest two temperatures shown, the curves are essentially the same *except for the region near zero frequency*, where the maximum diverges as  $T \rightarrow 0$ . This divergence in the noninteracting two-particle propagator is an indication that the electron gas is susceptible to pair formation (for superconductivity or charge and spin density waves).

Fig. A.2(b) shows the spectral function,  $B_0(\vec{q}, \nu) \equiv -\text{Im}\chi_0(\vec{q}, \nu + i\delta)/\pi$  vs. frequency. Aside from the asymmetrization, this quantity provides an image of the single electron density of states. This remains true in any dimension, as can be seen from taking the imaginary part of Eq. (A.24):

$$B_0(\vec{q} = 0, \nu) = -\frac{1}{2} \tanh\left(\frac{\beta\nu}{4}\right) g\left(\frac{\nu}{2} + \mu\right) \quad (\text{A.25})$$

where  $g(\epsilon)$  is the single electron density of states and  $B_0$  denotes the noninteracting result. As the temperature approaches zero, the hyperbolic tangent function simply changes sign at the origin. In Fig. A.1(b) the delta-function structure was merely providing an image of the discretized density of states for a finite system.

The well-defined symmetry of both figures is due to the particle-hole symmetry at half-filling (we have set the chemical potential equal to zero). In the more general case, the chemical potential is adjusted such that, for a fixed electron number density, the number equation Eq. (A.18) is satisfied.

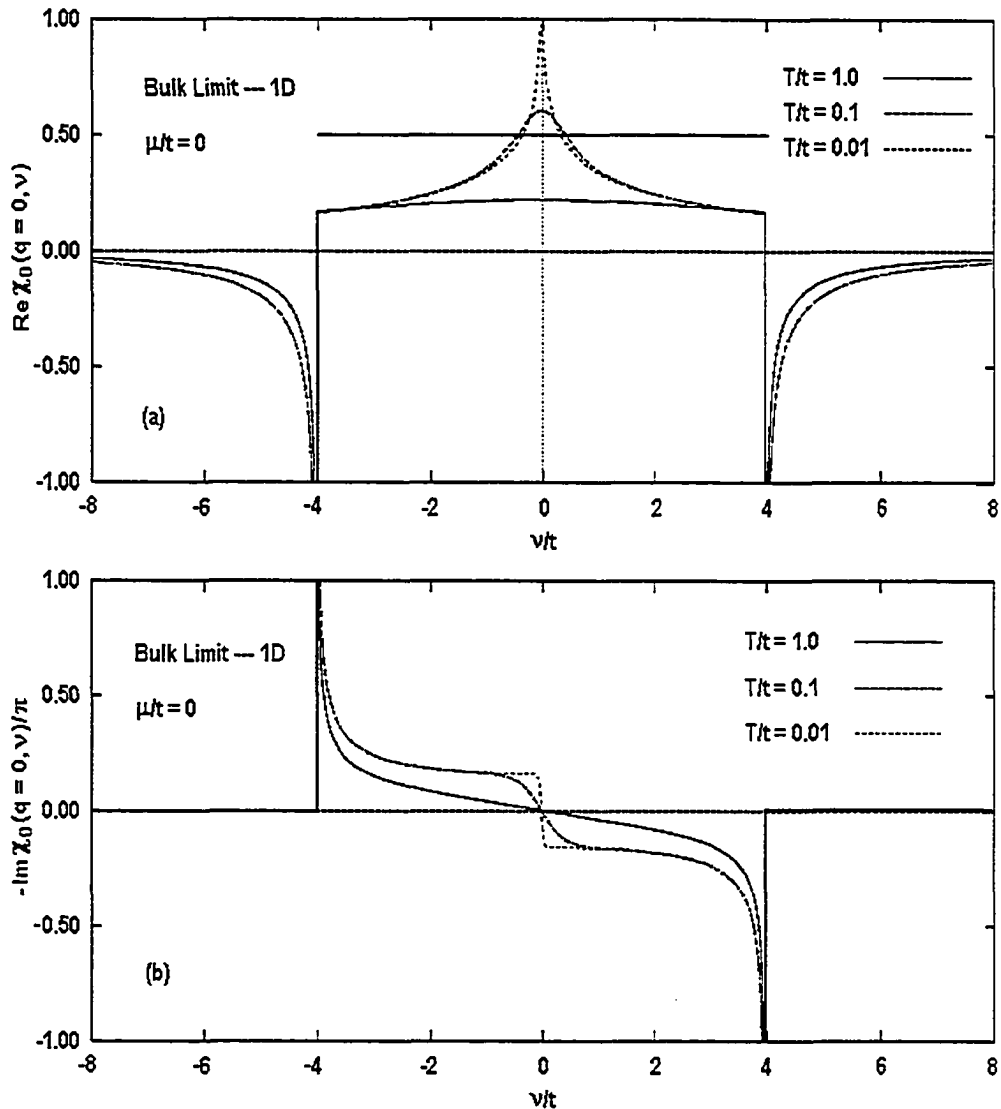


Figure A.2: Real (a) and imaginary (b) parts of the noninteracting susceptibility (Eq. (A.24)) at zero wavevector vs. frequency, for three different temperatures, for the bulk limit in one dimension. Note that part (a) in particular looks very different from the finite size counterpart in Fig. A.1(a). In particular, the poles corresponding to sums of single electron energies are evident only in (b). The developing singularity at zero frequency remains, as is evident in (a).



## A.4 The Cooper instability

The plot shown in Fig. A.1(a) is used to illustrate how the Cooper instability arises in the presence of interactions. For quick reference, we rewrite below Eq. (2.33) for the pair propagator when interactions are included in a minimal way:

$$G_{2,11}(Q) \equiv \chi(\vec{q}, i\nu_n) = \frac{\chi_{00}(\vec{q}, i\nu_n)}{1 - |U|\chi_{00}(\vec{q}, i\nu_n)}. \quad (\text{A.26})$$

With our eye on Fig. A.1(a), the idea is that once the minimum crosses a horizontal line representing the value  $1/|U|$  (shown in Fig. A.1(a) at 0.5), an instability occurs. This results in two real roots joining together and becoming pure imaginary. This transition is viewed as a signal that the pair particle propagator becomes unstable in time [65, 91, 68]. We will clarify this point shortly.

In the thermodynamic limit [92], as one can see in Fig. A.2(a), an instability would be signalled by the maximum crossing some line (representing  $1/|U|$ ), at which point a pole appears in the two electron propagator in the upper half plane. As in the finite lattice calculation the pole has a real part which is zero; unlike that case, however, the pole passes from the lower half plane to the upper half one. The interpretation that this signals a two particle propagator that increases exponentially in time remains in the thermodynamic limit, although the reasoning is somewhat different. Now we require *both* the imaginary and real parts of the denominator in Eq. (A.26) (with argument  $\vec{q} = 0$  and  $i\nu_n$  analytically continued to complex  $z$ ) to be zero. One can show, by adopting the approximate form,  $\chi_{00}(\vec{q} = 0, z) \approx 1/(a - ibz)$  near the instability temperature, that the solution is given at a complex frequency with a real part of zero, and with an imaginary part which is negative above the instability and positive below it. The emergence of a pole for the two electron propagator in the upper half plane signals an instability, just as in the finite system.

To illustrate the onset of the instability, we will go from imaginary to real time (see the discussion in Appendix B, §B.1). Assuming an analytic continuation has been performed (easily in the case of Eq. (A.26), given Eq. (A.24)), one can convert the frequency integral in Eq. (B.2) (where the one-particle propagator is replaced by the pair propagator) into a complex contour integral. The contour extends from just above the real axis to infinity

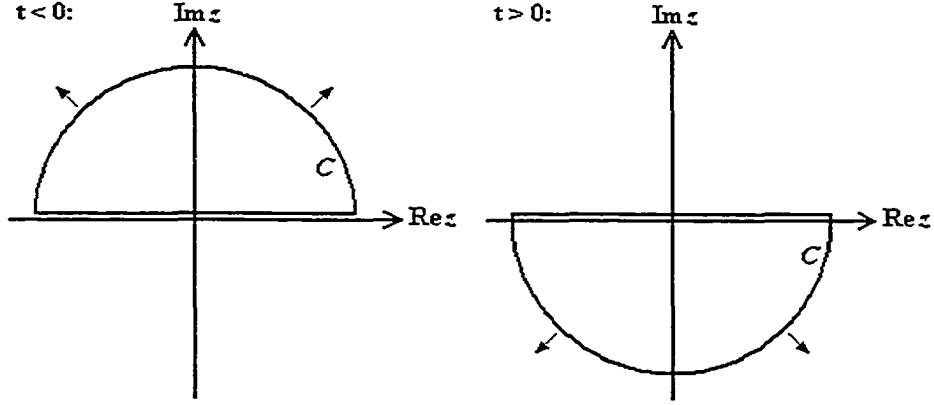


Figure A.3: The upper and the lower integration contours, as discussed in text. The straight line portion of each contour lies infinitesimally above the real axis. The semi-circular arc extends to infinity.

in the upper half plane  $\mathbb{U}$  (if  $t < 0$ ) or in the lower half plane  $\mathbb{L}$  (if  $t > 0$ ):

$$\chi^R(\vec{q}, t) = \frac{1}{2\pi} \int_C dz e^{-izt} \chi(\vec{q}, z). \quad (\text{A.27})$$

According to the residue theorem, the integral in Eq. (A.27) is obtained by summing all the residues of the poles of  $e^{-izt} \chi(\vec{q}, z)$  in  $\mathbb{U}$  for  $t < 0$  (which is zero when all the poles of  $\chi(\vec{q}, z)$  lie on the real axis  $\mathbb{R}$ ), and by summing all the residues of its poles in  $\mathbb{R} \cup \mathbb{L}$  for  $t > 0$  (which recovers the correspondent of Eq. (B.2) for  $\chi(\vec{q}, z)$ ). Now consider the contribution to the retarded pair propagator due to a single complex pole  $z_0$ ,

$$\int_C dz \frac{e^{-izt}}{z - z_0}. \quad (\text{A.28})$$

If this pole is not in the upper half plane (*i.e.*, it is either real or in the lower half plane:  $z_0 \in \mathbb{R} \cup \mathbb{L}$ ), then its contribution is proportional to  $\theta(t) e^{-i(\text{Re } z_0)t} e^{(\text{Im } z_0)t}$ . This result is entirely consistent with the Heaviside factor in the definition of the retarded propagator (see Eq. (B.3)). Moreover, since  $\text{Im } z_0 \leq 0$ , the contribution to the pair propagator either remains constant in magnitude or decays exponentially in time.

Now consider what happens if the pole moves into the upper half plane (*i.e.*,  $z_0 \in \mathbb{U}$ ). First of all, there will be a contribution proportional to

$e^{-i(\text{Re } z_0)t} e^{(\text{Im } z_0)t}$  even when  $t < 0$ , in violation of the causality principle, since it gives a response *before* the initial injection of the pair at time zero. Furthermore, for  $t > 0$  this contribution grows without bound as  $t \rightarrow \infty$  (now,  $\text{Im } z_0 > 0$ ). The appearance of a mode that increases exponentially in time indicates that the system has become unstable.

# Appendix B

## Analytic continuation and Padé approximants

### B.1 Analytic continuation

In many-body problems, analytic continuation arises from the need to recover real-time dynamics from a response function calculated at non-zero temperatures in the Matsubara formalism. For example, one is often interested in the spectral function:

$$A(\omega) = -\frac{1}{\pi} \text{Im} G^R(\omega), \quad (\text{B.1})$$

where  $G^R(\omega)$  is the Fourier transform of the retarded Green function:

$$G^R(t) = \frac{1}{2\pi} \int_{-\infty}^{\infty} d\omega e^{-i\omega t} G^R(\omega). \quad (\text{B.2})$$

In real time, the retarded Green function

$$G^R(t) = -i \langle \{c(t), c^\dagger(0)\} \rangle \theta(t) \quad (\text{B.3})$$

describes the response of the system to when a particle is added at time zero and removed at time  $t$ .

Most of the time, however, the result of calculations provides the function of interest at a discrete set of Matsubara points on the imaginary axis; thus, one will have obtained the values of the Fourier components of the thermal Green function

$$G(\tau) = \frac{1}{\beta} \sum_m e^{-i\omega_m \tau} G(i\omega_m). \quad (\text{B.4})$$

In the Matsubara formalism, time is a complex quantity, related to temperature. Its definition involves a imaginary-time ordering operator, as seen in §2.3.1 and reiterated below (showing only the time, frequency dependence, respectively, for clarity, like in the rest of this Appendix):

$$G(\tau) = -\langle T_\tau [c(\tau)c^\dagger(0)] \rangle, \quad (\text{B.5})$$

The fermionic (bosonic) thermal Green functions are antiperiodic (periodic) to shifts  $\tau \rightarrow \tau + \beta$ ; thus, both species are periodic with period  $2\beta$  (property used in deriving Eq. (B.4)). The physical significance of the thermal (imaginary-time) Green function is not as clear as that of its real-time counterpart; nonetheless, it has the advantage of a clear and elegant mathematical formalism, and that of computational ease. Moreover, as we alluded to in opening this Appendix, all the information needed from real-time propagators can potentially be extracted from the Matsubara formalism, by means of analytic continuation.

The foundation for this method was laid by Baym and Mermin [88]. They have shown that there exists a unique function, defined on the complex domain, which takes on the values of the Fourier components of the thermal Green function at Matsubara points on the imaginary axis, and gives the Fourier transform of the retarded Green function just above the real axis:

$$\bar{G}(i\omega_m) = G(i\omega_m); \quad (\text{B.6})$$

$$\bar{G}(\omega + i\delta) = G^R(\omega), \quad \delta \rightarrow 0^+. \quad (\text{B.7})$$

This function is analytic everywhere in the complex plane, with the exception of the real axis; this is a causality requirement. The values of  $\bar{G}$  in the upper and lower half planes are related by

$$\bar{G}(z^*) = [\bar{G}(z)]^*, \quad (\text{B.8})$$

which is a statement of the time reversal symmetry between the retarded and advanced Green functions. A consequence of this property is that the imaginary part of  $\bar{G}$  may be discontinuous across the real axis. The measure of this discontinuity is given by the spectral function, as can be seen by using Eqs. (B.7) and (B.8) in Eq. (B.1):

$$A(\omega) = -\frac{1}{\pi} \text{Im} \bar{G}(\omega + i\delta) = -\frac{1}{2\pi i} [\bar{G}(\omega + i\delta) - \bar{G}(\omega - i\delta)], \quad (\text{B.9})$$

Finally, in regard to the properties of  $\bar{G}$ , one can write a spectral (Lehmann) representation for this function:

$$\bar{G}(z) = \int_{-\infty}^{\infty} d\omega \frac{A(\omega)}{z - \omega}. \quad (\text{B.10})$$

Clearly, the function  $\bar{G}$  can be very useful, assuming one can construct it. Baym and Mermin [88] have shown that this is possible, in principle, provided we know  $G(i\omega_n)$  for an infinite set of points. In practice, however, we can only calculate the values of the thermal Green function at a finite number of Matsubara frequencies. Moreover, the theorem in Ref. [88] only shows the existence of the function  $\bar{G}$ ; there is no general method to perform the analytic continuation. This leads us to the need for approximate procedures such as the Padé approximant method.

## B.2 Padé approximants - Thiele's reciprocal difference algorithm

Typically, within the Matsubara formalism we calculate  $G(i\omega_m)$  from its self-energy  $\Sigma(i\omega_m)$ , via Dyson's equation, Eq. (2.36). In turn, the self-energy is calculated from some approximate theory, *e.g.*, some version of the T-matrix theory. The Padé method is based on the assumption that  $\bar{G}$  (or  $\bar{\Sigma}$ ) can be written as a rational polynomial or terminating continued fraction. The latter is usually more useful for investigating the analytic structure. Terminating a continued fraction decomposition is equivalent to expressing the function of interest by ratios of polynomials.

In what follows, we present a recursive algorithm called Thiele's Reciprocal Difference Method, used by Vidberg and Serene [89] in the context of the Eliashberg equations. In outlining the methodology of this procedure we follow Mitrović *et al.* [93]. Suppose we know the values  $F_i$  of a complex function  $F(z)$  at  $N$  points  $z_i$  ( $i = 1, \dots, N$ ) in the complex plane. The  $N$ -point Padé approximant to  $F(z)$  is defined as a continued fraction

$$F_N(z) = \frac{a_1}{1 + \frac{a_2(z-z_1)}{1 + \dots + \frac{a_N(z-z_{N-1})}{1}}}. \quad (\text{B.11})$$

This can be written more conveniently as

$$F_N(z) = \frac{a_1}{1+} \frac{a_2(z-z_1)}{1+} \frac{a_3(z-z_2)}{1+} \dots \frac{a_N(z-z_{N-1})}{1}. \quad (\text{B.12})$$

such that  $F_N(z_i) = F_i$ ,  $i = 1, \dots, N$ . In our case, the  $z_i$  are the fermionic Matsubara frequencies  $i\omega_m$ ,  $m = 1, \dots, N$  and the  $F_i$  are the corresponding values of the self-energy at those frequencies. The coefficients  $a_i$  are given by recursion:

$$a_i = g_i(z_i), \quad g_1(z_i) = F_i, \quad i = 1, \dots, N$$

$$g_p(z) = \frac{g_{p-1}(z_{p-1}) - g_{p-1}(z)}{(z_{p-1} - z)g_{p-1}(z)}, \quad p \geq 2. \quad (\text{B.13})$$

It can be shown that

$$F_N(z) = \frac{P_N(z)}{Q_N(z)}, \quad (\text{B.14})$$

where  $P_N(z)$  and  $Q_N(z)$  are polynomials given by the recursive formulae:

$$P_{n+1} = P_n(z) + (z - z_n)a_{n+1}P_{n-1} \quad \text{and}$$

$$Q_{n+1} = Q_n(z) + (z - z_n)a_{n+1}Q_{n-1}, \quad (\text{B.15})$$

where  $P_0 = 0$ ,  $P_1 = a_1$ ,  $Q_0 = Q_1 = 1$  and  $n = 1, \dots, N - 1$ .

This algorithm is quite efficient numerically. However, the accuracy requirements for the solution on the imaginary axis can be very high. A discussion about the level of numerical precision needed for a reliable Padé result can be found in Ref. [86], together with an alternate algorithm implemented using the symbolic computation package MAPLE. The symbolic implementation allows one to transcend the limits imposed by hardware floating-point numerics and enables calculations to any desired level of precision. The downside is the high cost in computational resources that comes with enforcing such high accuracy.